Studies on Nonlinear Beam Dynamics in Uniaxial Nematic Liquid Crystals Under the Influence of Temperature, Diffractive Radiation, and Potentials

Thesis submitted to the University of Calicut
in partial fulfillment of the requirements
for the award of the degree of

DOCTOR OF PHILOSOPHY IN PHYSICS

by

SAJITHA N M

Under the guidance of

Dr. Suneera T P

Professor of Physics

Research and Post Graduate Department of Physics
Government College Madappally, Vadakara,
Kozhikode, Kerala - 673102, India

April 2025

GOVERNMENT COLLEGE, MADAPPALLY
VATAKARA-673 102, KOZHIKODE DISTRICT, KERALA
Phone: 9188900231
Email- gcmadappally@gmail.com
Website - www.madappallycollege.org
ACCREDITED AT "A" LEVEL BY NAAC

CERTIFICATE

Ref: 1) No. 96445/RESEARCH-C-ASST-1/2025/Admn, Dated: 22.09.2025

2) U.O.No. 7974/2022/Admn Dated 31.03.2022

This is to certify that no corrections or suggestions have been recommended by either adjudicator for the thesis of Ms. SAJITHA N M, research scholar under the guidance of Dr. Suneera T P, Professor, Research and Post Graduate Department of Physics, Government College Madappally, Vadakara. Therefore, the original thesis titled "Studies on Nonlinear Beam Dynamics in Uniaxial Nematic Liquid Crystals Under the Influence of Temperature, Diffractive Radiation, and Potentials", is resubmitted as such, and the contents of the soft copy and hard copy of the thesis are the same.

Research Supervisor
Prof. (Dr.) Suneera T P
Professor of Physics
Department of Physics,
Government College Madappally,
Vadakara-673102

Principal

Principal
GOVERNMENT COLLEGE, MADAPPALLY
MADAPPALLY COLLEGE (P.O)
PIN: 673 102

(College Seal)

Date: 07/10/2025

DECLARATION

I hereby declare that the work presented in the thesis entitled **'Studies on Nonlinear Beam Dynamics in Uniaxial Nematic Liquid Crystals Under the Influence of Temperature, Diffractive Radiation, and Potentials'** is based on the original work done by me under the guidance of **Dr. Suneera T P**, Professor, Department of Physics, Govt. College Madappally, Vadakara, Kerala, and has not been included in any other thesis submitted previously for the award of any degree. The contents of the thesis are undergone plagiarism check using 'IThenticate' software at C.H.M.K. Library, University of Calicut, and the similarity index found within the permissible limit. I also declare that the thesis is free from AI generated contents.

NM Sajitha
Sajitha N M
Research Scholar (Part-time)

Madappally
April 2025

Dr. Suneera T P
(Research Supervisor)

Dr. SUNEERA T.P
PEN: 602076
Professor of Physics
Govt. College, Madappally
PIN: 673102.

CERTIFICATE

Certified that the work presented in this thesis titled **'Studies on Nonlinear Beam Dynamics in Uniaxial Nematic Liquid Crystals Under the Influence of Temperature, Diffractive Radiation, and Potentials'** is a bonafide work done by **Ms. SAJITHA N M** under my guidance in the Department of Physics, Govt. College Madappally, Vadakara, Calicut, Kerala and that this work has not been included in any other thesis submitted previously for the award of any degree.

Madappally
April 2025

Dr. Suneera T P
(Research Supervisor)

Dr. SUNEERA T.P
PEN: 602076
Professor of Physics
Govt. College, Madappally
PIN: 673102.

UNIVERSITY OF CALICUT

CERTIFICATE ON PLAGIARISM CHECK

1.	Name of the Research Scholar	SAJITHA N M	
2.	Title of thesis / dissertation	Studies on Nonlinear Beam Dynamics in Uniaxial Nematic Liquid Crystals Under the Influence of Temperature, Diffractive Radiation, and Potentials	
3.	Name of the Supervisor	Dr. Suneera T P	
4.	Department/Institution	PG & Research Department of Physics, Govt. College Madappally, Vadakara, 673102 (PIN)	
5.		Non Core	Core
		Introduction/ Theoretical overview/Review of literature/ Materials & Methods/ Methodology	**Analysis/Result/Discussion / Summary/Conclusion/ Recommendations**
	Similar content (%) identified	**4**	**6**
	Acceptable maximum limit (%)	10	10
6.	Software used	iThenticate	
7.	Date of verification	16.04.25	

**Report on plagiarism check, specifying included/excluded items with % of similarity to be attached.*

Checked by (with name, designation & signature)

Dr. Nasirudheen. T
Assistant Librarian
University of Calicut, Kerala.

Name and signature of the Researcher SAJITHA. N.M , NM Sajitha

Name and signature of the Supervisor. Prof (Dr) Suneera.T.P

Dr. SUNEERA T.P
PEN: 602076
~~Associate~~ Professor
Department of Physics
Govt. College, Madappally.

The Doctoral Committee* has verified the report on plagiarism check with the contents of the thesis, as summarized above and appropriate measures have been taken to ensure originality of the Research accomplished herein.

Name & Signature of the HoD/HoI (Chairperson of the Doctoral Committee) Shimu Pattithara Malammal

**In case of languages like Malayalam, Tamil etc..on which no software is available for plagiarism check, a manual check shall be made by the Doctoral Committee, for which an additional certificate has to be attached.*

Principal
GOVERNMENT COLLEGE, MADA
MADAPPALLY COLLEGE P.
PIN: 673 102

GOVERNMENT COLLEGE, MADAPPALLY
KOZHIKODE DISTRICT
PIN: 673 102
MADAPPALLY COLLEGE P.O.

Acknowledgements

My desire has become a reality thanks to God's grace and the blessings of my family.

I am grateful to everyone who supported me during these years. Firstly I wish to express my gratitude to my Ph.D. supervisor Dr. Suneera T P, Professor and Head of the Department, Department of Physics, Govt. College Madappally, Vadakara, for her guidance and continued support over the last three years. She has shed light on novel and fascinating areas of nonlinear Physics, patiently explaining numerous techniques and methods that will help me along the way. Her desire to share her vast knowledge, as well as her boundless enthusiasm for the subject, has been an inspiration.

I am deeply indebted to Dr. Shinu P M, Principal, Govt. College, Madappally, and Dr. Preetha B, former Principal, Govt. College, Madappally for the facilities provided in continuing the research work. I express my sincere gratitude and thanks to Dr. Nithyaja B, Associate Professor, Department of Physics; Dr. G Harikrishnan, Associate Professor, Department of Physics; and Mr. M Hameed, Associate Professor, Department of Physics, Govt. College Madappally for the advice, valuable suggestions, and help were provided during the initial stage of this work. I wish to express my thanks to all my colleagues in the Department of Physics, Government College, Madappally for their support.

Many thanks to the great scientists I've met at conferences and meetings for showing me the broad and never-ending research in solitons in liquid crystals. I also want to thank all of the teachers who taught me at various stages of my education.

I would like to express my sincere thanks to Sandeep K V, Assistant Professor, Department of Physics, Mahatma Gandhi Govt. Arts College for providing technical support during necessary situations. I express my heartfelt gratitude to Dr. Anuradha, Associate Professor of Mathematics, Govt. Engineering College, Kozhikode for her inspiration, invaluable suggestions, support, and encouragement to complete this work. This thesis would also be sorely incomplete without thanking some of the many friends Dr. Nitu Ashok, Mr. Sanid C, Dr. Aysha Muhsina, Dr. Thasneem A R and Ms. Bhagyasree G S.

Without the help of my family, who were willing to give me the time and space to work on it, I would not have been able to complete this thesis. To my dear parents Chandrika N P and Chandran N M, thank you for the love and care you have provided, in difficult times and when things were going well. My brother Sajeesh A K, your unwavering support has been overwhelming and much appreciated. You are a constant inspiration for me and someone I will always seek. Progress has, at times, been challenging as I have balanced professional responsibilities and family commitments alongside my part-time research work. I am deeply grateful to my husband Sanal M K, for his unwavering support, patience, and encouragement throughout this journey. He gave me the courage to believe in myself and the confidence to persevere and succeed during my PhD journey. My heartfelt thanks go to my daughter Sanviya S S, whose love, understanding, and cheerful presence have been a constant source of strength. I also thank my little boy Shriyansh S S, for the joy and warmth he brings into my life. Even without understanding the path I am on, his innocent smile has often brightened my most difficult days.

Sajitha N M

Abstract

Studies on Nonlinear Beam Dynamics in Uniaxial Nematic Liquid Crystals Under the Influence of Temperature, Diffractive Radiation, and Potentials

This thesis investigated the nonlinear beam dynamics in uniaxial nematic liquid crystals under the influence of temperature, diffractive radiation, and potentials. The study emphasizes the role of diffractive radiation in ensuring undisturbed nematicon propagation by utilizing both variational and numerical methods. A key aspect of the research is the competition between focusing reorientational and defocusing thermal nonlinearities, which results in the formation of multi-peak nematicons. It also investigates how parabolic potential influences the generation of higher harmonics of nematicons. The stability of steady-state solutions against small perturbations is studied by applying the Bogoliubov-De-Gennes equations. The study has been extended to the thermal response of nematicons in a parabolic potential. Single-peak nematicons exist only in the absence of thermal response coefficients. The presence of both focusing reorientational and defocusing thermal nonlinearities creates multiple maxima in the energy landscape, allowing for the stabilization of double-peak nematicons as equilibrium states. Periodic oscillations are observed in nematicons within a parabolic potential, with their wavelength being influenced by thermal response coefficients. The linear stability analysis reveals that single-peak and periodically oscillating double-peak nematicons are stable, whereas non-oscillating double-peak nematicons are unstable. The research also extends to study the formation and stability of gap nematicons. Finally, the study explores the effects of thermal response and diffractive radiation on multi-peak gap nematicons.

Keywords: focusing reorientational nonlinearity; defocusing thermal nonlinearity; higher harmonic generation; band gap spectrum; gap nematicons

Sajitha N M
(Research Scholar)

Dr. Suneera T P
(Research Supervisor)

Dr. SUNEERA T.P
PEN: 602076
Professor of Physics
Govt. College, Madappally
PIN: 673102.

സാരാംശം

Studies on Nonlinear Beam Dynamics in Uniaxial Nematic Liquid Crystals Under the Influence of Temperature, Diffractive Radiation, and Potentials

ഈ പ്രബന്ധത്തിൽ, താപനില, ഡിഫ്രാക്റ്റീവ് വികിരണം, പൊട്ടൻഷ്യലുകൾ എന്നിവയുടെ സ്വാധീനത്തിൽ യൂണി-ആക്സിയൽ നിമാറ്റിക് ലിക്വിഡ് ക്രിസ്റ്റലിലുള്ള നോൺലീനിയർ ബീം ഡൈനാമിക്സ് വിശകലനം ചെയ്തു. ഒരു തടസ്സരഹിതമായ നിമാറ്റികോൺ പ്രചരണത്തിനായുള്ള ഡിഫ്രാക്റ്റീവ് വികിരണത്തിന്റെ പ്രാധാന്യം വേരിയേഷണൽ, ന്യൂമറിക്കൽ അനാലിസിസ് മുതലായ രീതികൾ ഉപയോഗിച്ച് വിശദീകരിക്കുന്നു. ഈ ഗവേഷണത്തിന്റെ ഒരു പ്രധാന ഭാഗം ഫോക്കസിംഗ് റീയോറിയന്റേഷണൽ, ഡിഫോകസിംഗ് താപ നോൺലിനിയാരിറ്റികളുടെ മത്സരമാണ്. ഇത് മൾട്ടിപീക്ക് നിമാറ്റിക്കോണുകളുടെ രൂപീകരണത്തിലേക്ക് നയിക്കുന്നു. നിമാറ്റിക്കോണുകളുടെ ഉയർന്ന ഹാർമോണിക് ഉൽപാദനത്തിൽ പാരബോളിക് പൊട്ടൻഷ്യലിന്റെ സ്വാധീനത്തെക്കുറിച്ച് പഠനം പരിശോധിക്കുന്നു. ബോഗോളിബോവ്-ഡി-ജെനസ് സമവാക്യങ്ങൾ ഉപയോഗിച്ച് ചെറിയ വ്യതിയാനങ്ങൾക്കു കീഴിലുള്ള സ്റ്റേഷനറി സൊല്യൂഷന്റെ സ്ഥിരത പരിശോധിച്ചിട്ടുണ്ട്. പാരബോളിക് പൊട്ടൻഷ്യലിൽ നിമാറ്റികോണുകളുടെ താപ പ്രതികരണം വിശകലനം ചെയ്യുന്നതിനായി പഠനം വിപുലീകരിക്കപ്പെട്ടിരിക്കുന്നു. താപപ്രതികരണ സഹഗുണങ്ങൾ ഇല്ലാത്തപ്പോൾ മാത്രമാണ് സിംഗിൾ പീക്ക് നിമാറ്റിക്കോണുകൾ നിലനിൽക്കുന്നത്. ഫോക്കസിംഗ് റീയോറിയന്റേഷണൽ, ഡിഫോകസിംഗ് താപ നോൺലിനിയാരിറ്റീസ് എന്നിവയുടെ സാന്നിധ്യം ഊർജ്ജലാൻഡ്സ്കേപ്പിൽ നിരവധി മാക്സിമകൾ ഉണ്ടാക്കുകയും, ഡബിൾ പീക്ക് നിമാറ്റിക്കോണുകൾക്ക് സമതുലിതാവസ്ഥയിൽ സ്ഥിരത നൽകുകയും ചെയ്യുന്നു. ഒരു പാരബോളിക് പൊട്ടൻഷ്യലിന്റെ സാന്നിധ്യമുണ്ടെങ്കിൽ, നിമാറ്റിക്കോണിൽ ആവർത്തിത ദോളനങ്ങൾ കാണപ്പെടുന്നു. ഇതിന്റെ ദോളനങ്ങളുടെ തരംഗദൈർഘ്യത്തിൽ താപപ്രതികരണ സഹഗുണങ്ങൾക്കുള്ള നിർണായക സ്വാധീനവും കണ്ടെത്തി. ലീനിയർ സ്ഥിരതാവിശകലനം സിംഗിൾ പീക്ക്, ആവർത്തിത ദോളനങ്ങളുള്ള ഡബിൾ പീക്ക് നിമാറ്റിക്കോണുകൾ സ്ഥിരമാണെന്നും, എന്നാൽ ഡബിൾ പീക്ക് നിമാറ്റിക്കോണിന് ദോളനരഹിത സ്വഭാവമുള്ളപ്പോൾ അസ്ഥിരമാണെന്നും കാണിക്കുന്നു. ഇതിന് പുറമേ, ഗ്യാപ് നിമാറ്റിക്കോണുകളുടെ രൂപീകരണവും സ്ഥിരതയും പഠിക്കാൻ ഗവേഷണം വ്യാപിപ്പിച്ചിട്ടുണ്ട്. അവസാനമായി, ഈ പഠനം മൾട്ടിപീക്ക് ഗ്യാപ് നിമാറ്റിക്കോണുകളിൽ താപ പ്രതികരണത്തിന്റെയും ഡിഫ്രാക്റ്റീവ് വികിരണത്തിന്റെയും സ്വാധീനങ്ങൾ പരിശോധിക്കുന്നു.

കീവേഡുകൾ: ഫോക്കസിംഗ് റീയോറിയന്റേഷണൽ നോൺലിനിയാരിറ്റി; ഡിഫോകസിംഗ് താപ നോൺലിനിയാരിറ്റി; ഹൈയർ ഹാർമോണിക് ജനറേഷൻ; ബാൻഡ് ഗ്യാപ് സ്പെക്ട്രം; ഗ്യാപ് നിമാറ്റികോൺ

Sajitha N M
(Research Scholar)

Dr. Suneera T P
(Research Supervisor)

Dr. SUNEERA T.P
PEN: 602076
Professor of Physics
Govt. College, Madappally
PIN: 673102.

List of Published Papers

1. **N. M. Sajitha**, T. P. Suneera, ‘Interplay between diffractive radiation shed and damping coefficient on nematicon propagation’. Journal of Modern Optics. 2022 nov; 69(20): 1134–1141.

2. **N. M. Sajitha**, T. P. Suneera, ‘The effect of parabolic potential on the generation of higher harmonics of nematicons’. Physica Scripta. 2023 Apr; 98(5): 055502.

3. **N. M. Sajitha**, T. P. Suneera, ‘Thermal response of single-peak and double-peak nematicons’. The European Physical Journal Plus. 2023 Dec; 138(12): Article ID 1073.

4. **N. M. Sajitha**, T. P. Suneera, ‘Thermal response of nematicons in a parabolic potential’. Physica Scripta. 2024 May; 99(6): 065567.

5. **N. M. Sajitha**, T. P. Suneera, ‘The formation and stability of single-peak and multi-peak gap nematicons in a periodic potential’. Liquid Crystals. 2024 Sep; 1–13.

6. **N. M. Sajitha**, T. P. Suneera, ‘Unveiling the dynamics of multi-peak gap nematicons: Effects of thermal response and diffractive radiation’. Chaos. 2025 Mar; 35(3): 033149.

List of Conference Presentations

1. **N. M. Sajitha**, T. P. Suneera, The influence of diffractive radiation shed on the damping of a dipole mode nematicon, Conference on Nonlinear Systems and Dynamics (CNSD 2022), IISER Pune, December 2022.
2. **N. M. Sajitha**, T. P. Suneera, Thermal Response of Nematicons in a Parabolic Potential, International Conference on Optics, Photonics & Quantum Information (OPTIQ - 2023), Cochin University of Science And Technology (CUSAT), December 2023.
3. **N. M. Sajitha**, T. P. Suneera, Thermal Response of Double peak Nematicons in a Periodic Potential, International Conference on Advanced Materials for Sustainability (ICAMS - 2023), University of Calicut, December 2023.

Contents

Preface **xx**

1 Introduction **1**

1.1 Solitons 1
1.2 Liquid Crystals 3
1.2.1 Nematic Liquid Crystals 6
1.2.2 E7 NLC 8
1.3 Nematicons 12
1.4 Literature Review 14
1.5 Governing Equations 18
1.6 Methodology 22
1.6.1 Semi-Analytical Methods 23
1.6.2 Numerical Methods 25
1.7 Objectives of this Thesis 30
1.8 Relevance of this Study 30
1.9 Motivation of this Study 31
1.10 Outline of Thesis 33

2 Impact of Diffractive Radiation Shed on Nematicon Propagation **46**

2.1 Introduction 47
2.2 Theoretical model 48
2.3 Results and discussions 55
2.4 Conclusion 58

3 Competition of Nonlinearities in Nematicon Dynamics 61
3.1 Introduction 62
3.2 Theoretical model 63
3.3 Results and discussions 67
3.4 Linear stability analysis 71
3.5 Conclusion 74

4 Higher Harmonic Generation in NLC 78
4.1 Introduction 79
4.2 Theoretical model 80
4.3 Results and discussions 86
4.4 Linear stability analysis 90
4.5 Conclusion 92

5 Thermal Effects on Nematicons in Parabolic Potential 96
5.1 Introduction 97
5.2 Theoretical model 98
5.3 Results and discussions 105
5.4 Linear stability analysis 107
5.5 Conclusion 110

6 Dynamics of Gap Nematicons 115
6.1 Introduction 116
6.2 Theoretical model 117
6.3 Band gap spectrum and stationary solutions 119
    6.3.1 Band gap spectrum 119
    6.3.2 Stationary solutions 122
6.4 Propagation dynamics of gap nematicons 123
6.5 Results and discussions 125
    6.5.1 Single-peak gap nematicons 127
    6.5.2 Multi-peak gap nematicons 127

6.6 Linear stability analysis 130
6.7 Conclusion 134

7 Multi-Peak Gap Nematicons: Effects of Thermal Response and Diffractive Radiation 139

7.1 Introduction 140
7.2 Theoretical model 141
7.3 Band gap spectrum and stationary solutions 145
    7.3.1 Band gap spectrum 145
    7.3.2 Stationary solutions 149
7.4 Propagation dynamics of gap nematicons 151
7.5 Results and discussions 155
    7.5.1 Thermal response only 155
    7.5.2 Thermal response and diffractive radiation 157
7.6 Linear stability analysis 159
7.7 Conclusion 163

8 Results and Recommendations 167

8.1 Results 168
8.2 Recommendations 171

List of Figures

1.1 Soliton profile 3

1.2 The arrangements of molecules in (a) solids, (b) liquid crystals, and (c) liquid are shown. The molecules are represented by yellow-colored ellipses. 4

1.3 The mesogen alignment of a nematic liquid crystal is shown. The mesogens prefer to order in the direction of the director n. 7

1.4 (a) Pure linear diffraction, (b) self-focusing of an optical beam. . 13

2.1 The figure of the considered sample and interaction geometry. A nematic liquid crystal with the ellipses represents the elongated NLC molecules. The green arrow represents the input light beam impinges on the sample. 49

2.2 Beam propagation with constant damping plotted for damping coefficient $\epsilon_s = 3$ for an initial excitation with a_{x0}=1.3, a_{y0}=1.8, w_{x0}=12, w_{y0}=12, σ_{x0}=0, σ_{y0}=0. In the first row (Results of variational analysis): (a) evolution of amplitude along the x-direction, (b) evolution of amplitude along the y-direction. The second and third-row corresponds to numerical results. In the second row: (c) the evolution of amplitude along the x-direction, (d) evolution of amplitude along the y-direction for g_x=g_y=0; In the third row: (e) the evolution of amplitude along the x-direction, (f) evolution of amplitude along the y-direction for g_x=g_y=0.08. . 51

2.3 Beam propagation with periodic damping plotted for damping coefficient $\epsilon_s = 3$ for an initial excitation with a_{x0}=1.3, a_{y0}=1.8, w_{x0}=12, w_{y0}=12, σ_{x0}=0, σ_{y0}=0. In the first row (Results of variational analysis): (a) evolution of amplitude along the x-direction, (b) evolution of amplitude along the y-direction. The second and third-row corresponds to numerical results. In the second row: (c) the evolution of amplitude along the x-direction, (d) evolution of amplitude along the y-direction for g_x=g_y=0; In the third row: (e) the evolution of amplitude along the x-direction, (f) evolution of amplitude along the y-direction for g_x=g_y=0.08. . 54

2.4 Beam propagation with hyperbolic damping plotted for damping coefficient $\epsilon_s = 3$ for an initial excitation with a_{x0}=1.3, a_{y0}=1.8, w_{x0}=12, w_{y0}=12, σ_{x0}=0, σ_{y0}=0. In the first row (Results of variational analysis): (a) evolution of amplitude along the x-direction, (b) evolution of amplitude along the y-direction. The second and third-row corresponds to numerical results. In the second row: (c) the evolution of amplitude along the x-direction, (d) evolution of amplitude along the y-direction for g_x=g_y=0; In the third row: (e) the evolution of amplitude along the x-direction, (f) evolution of amplitude along the y-direction for g_x=g_y=0.08. . 57

3.1 The interaction geometry. A nematic liquid crystal with ellipses which have long axes parallel to y is used to represent the elongated NLC. The input light beam is shown with a green arrow impinging normally to the molecular director on the sample. The angle ξ describes the reorientation of the optic axis, n in the (x, y) plane. 65

3.2 Evolution of the amplitude in two transverse directions for $\tau_0 = \tau_1 = 0$: (a) Along the x-direction, and (b) along the y-direction. 69

3.3 Evolution of the amplitude in two transverse directions for $\tau_0 = \tau_1 =$ 0.5: (a) Along the x-direction, and (b) along the y-direction. 69

3.4 Evolution of the amplitude in two transverse directions for $\tau_0 = \tau_1 =$ 0.6: (a) Along the x-direction, and (b) along the y-direction. 69

3.5 Evolution of the amplitude in two transverse directions for $\tau_0 = \tau_1 =$ 1.0: (a) Along the x-direction, and (b) along the y-direction. 70

3.6 Evolution of the amplitude in two transverse directions for $\tau_0 = \tau_1 =$ 1.6: (a) Along the x-direction, and (b) along the y-direction. 70

3.7 The results of linear stability analysis of the system for thermal response coefficients (a) $\tau_0 = \tau_1 = 0$, and (b) $\tau_0 = \tau_1 = 0.2$. The real and imaginary parts of the perturbation eigenvalues (λ) versus the propagation constant μ are shown. 73

3.8 The results of linear stability analysis of the system for thermal response coefficients (a) $\tau_0 = \tau_1 = 0.5$, (b) $\tau_0 = \tau_1 = 0.6$, (c) $\tau_0 = \tau_1 = 1.0$, and (d) $\tau_0 = \tau_1 = 1.6$. The real and imaginary parts of the perturbation eigenvalues (λ) versus the propagation constant μ are shown. 74

4.1 The interaction geometry. The elongated NLC is represented by a nematic liquid crystal with ellipses, having long axes parallel to y. The green arrow depicts the input light beam impinging normally to the molecular director on the sample. The angle ξ describes the reorientation of the optic axis, n in the (x, y) plane. 81

4.2 Evolution of beam in two transverse directions in a parabolic potential with a strength of $Vo = 0.5$ V/μm for an initial excitation with a_{x0}=1.0, a_{y0}=1.4, w_{x0}=12, w_{y0}=12, σ_{x0}=0, σ_{y0}=0, g_{x0}=0, g_{y0}=0. Upper row represents the amplitude variation along x and y directions from variational analysis and lower row represents the amplitude variation from numerical analysis. 87

4.3 Evolution of beam in two transverse directions in a parabolic potential with a strength of $Vo = 1.0$ V/μm for an initial excitation with a_{x0}=1.0, a_{y0}=1.4, w_{x0}=12, w_{y0}=12, σ_{x0}=0, σ_{y0}=0, g_{x0}=0, g_{y0}=0. Upper row represents the amplitude variation along x and y directions from variational analysis and lower row represents the amplitude variation from numerical analysis. 88

4.4 Wavelength (μm) of periodic oscillations versus parabolic potential (V/μm). Variational results: Red (solid) line, Numerical results: Green (dotted) line. 89

4.5 Evolutions of width and phase in two transverse directions in a parabolic potential with a strength of $Vo = 0.5$ V/μm for an initial excitation with a_{x0}=1.0, a_{y0}=1.4, w_{x0}=12, w_{y0}=12, σ_{x0}=0, σ_{y0}=0, g_{x0}=0, g_{y0}=0. 89

4.6 The results of linear stability analysis of the system in a parabolic potential with the strength of (a) V_0 = 0.5 V/μm and (b) V_0 = 1.0 V/μm. The real and imaginary parts of the perturbation eigenvalues (λ) versus the propagation constant μ are shown. . . . 91

5.1 The interaction geometry. The elongated NLC is represented as a nematic liquid crystal with ellipses with long axes parallel to y. The input light beam is depicted with a green arrow impinging normally on the molecular director. The angle ξ indicates the reorientation of the optic axis, n in the (x, y) plane. 100

5.2 Evolution of the amplitude in two transverse directions for $\tau_0 = \tau_1 = 0$: (a) Along the x-direction, and (b) along the y-direction. 103

5.3 Evolution of the amplitude in two transverse directions for $\tau_0 = \tau_1 = 0.8$: (a) Along the x-direction, and (b) along the y-direction. 103

5.4 Evolution of the amplitude in two transverse directions for $\tau_0 = \tau_1 = 1.4$: (a) Along the x-direction, and (b) along the y-direction. 103

5.5 Evolution of the amplitude in two transverse directions for $\tau_0 = \tau_1 = 2.0$: (a) Along the x-direction, and (b) along the y-direction. 104

5.6 Evolution of the amplitude in two transverse directions for $\tau_0 = \tau_1 = 2.4$: (a) Along the x-direction, and (b) along the y-direction. 104

5.7 The thermal response coefficients versus wavelength (μm) of periodic oscillations. 106

5.8 The results of linear stability analysis of the system for thermal response coefficients (a) $\tau_0 = \tau_1 = 0$, (b) $\tau_0 = \tau_1 = 0.8$, (c) $\tau_0 = \tau_1 = 2.0$, and (d) $\tau_0 = \tau_1 = 2.4$. The real and imaginary parts of the perturbation eigenvalues (λ) versus the propagation constant μ are shown. 109

6.1 The interaction geometry. A nematic liquid crystal with ellipses with long axes parallel to y is used to represent the elongated NLC. The green arrow indicates the input light beam impinging normally to the molecular director on the sample. The reorientation of the optic axis, n in the (x, y) plane is described by the angle ξ. 118

6.2 Band gap spectrum and the stationary states. First row: (a) Band gap spectrum - The eigenvalue μ versus Bloch momentum k, with the first band in red (dashed) line, the second band in blue (dotted) line, and the third band in green (solid) line; (b) single-peak gap nematicons for a_{x0}=1.7, a_{y0}=2.0; (c) two peak gap nematicons for a_{x0}=4.1, a_{y0}=4.8. Second row for three peak gap nematicons: (d) a_{x0}=4.1, a_{y0}=4.9; (e) a_{x0}=4.5, a_{y0}=5.3; (f) a_{x0}=4.8, a_{y0}=5.6. Third row for four peak gap nematicons: (g) a_{x0}=8.3, a_{y0}=9.0; (h) a_{x0}=8.8, a_{y0}=9.5; (i) a_{x0}=9.6, a_{y0}=10.3. In all three rows, the strength of periodic potential is $V_0 = 1.7$. P blue (dashed) and Q red (solid) in Figures 6.2(b)-(i). 121

6.3 Evolution of beam for an initial excitation with a_{x0}=1.7, a_{y0}=2.0, w_{x0}=12, w_{y0}=12, σ_{x0}=0, σ_{y0}=0 with propagation constant μ=1.25 for a periodic potential strength of $V_0 = 1.7$. (a) Evolution of R; (b) Evolution of S. 124

6.4 Evolution of beam for an initial excitation with a_{x0}=4.1, a_{y0}=4.8, w_{x0}=12, w_{y0}=12, σ_{x0}=0, σ_{y0}=0 with propagation constant μ=1.9 for a periodic potential strength of $V_0 = 1.7$. (a) Evolution of R; (b) Evolution of S. 124

6.5 Evolution of beam for an initial excitation with w_{x0}=12, w_{y0}=12, σ_{x0}=0, σ_{y0}=0 with propagation constant μ=2.2. First column: evolution of R; second column: evolution of S. First row for a_{x0}=4.1, a_{y0}=4.9; second row for a_{x0}=4.5, a_{y0}=5.3; third row for a_{x0}=4.8, a_{y0}=5.6. In all three rows, the strength of periodic potential is $V_0 = 1.7$. 126

6.6 Evolution of beam for an initial excitation with w_{x0}=12, w_{y0}=12, σ_{x0}=0, σ_{y0}=0 with propagation constant μ=2.45. First column: evolution of R; second column: evolution of S. First row for a_{x0}=8.3, a_{y0}=9.0; second row for a_{x0}=8.8, a_{y0}=9.5; third row for a_{x0}=9.6, a_{y0}=10.3. In all three rows, the strength of periodic potential is $V_0 = 1.7$. 128

6.7 The results of linear stability analysis of the system in a periodic potential with the strength of $V_0 = 1.7$. (a) Stability analysis of single-peak gap nematicons for a_{x0}=1.7, a_{y0}=2.0. (b) Stability analysis of two peak gap nematicons for a_{x0}=4.1, a_{y0}=4.8. The real and imaginary parts of the perturbation eigenvalues (λ) versus the propagation constant μ are shown. 131

6.8 The results of linear stability analysis of the system in a periodic potential with the strength of $V_0 = 1.7$. (a) Stability analysis of three peak gap nematicons for a_{x0}=4.5, a_{y0}=5.3. (b) Stability analysis of four peak gap nematicons for a_{x0}=8.8, a_{y0}=9.5. The real and imaginary parts of the perturbation eigenvalues (λ) versus the propagation constant μ are shown. 131

6.9 The results of linear stability analysis of the system in a periodic potential with the strength of $V_0 = 1.7$. Stability analysis of three peak gap nematicons for (a) a_{x0}=4.1, a_{y0}=4.9; (b) a_{x0}=4.8, a_{y0}=5.6. Stability analysis of four peak gap nematicons for (c) a_{x0}=8.3, a_{y0}=9.0; (d) a_{x0}=9.6, a_{y0}=10.3. The real and imaginary parts of the perturbation eigenvalues (λ) versus the propagation constant μ are shown. 133

7.1 The considered geometry. The NLC molecules are depicted with ellipses and their long axes along y. The input beam is displayed in a green arrow, hitting normally on the molecular director. The angle ξ represents the director angle [5]. 142

7.2 Band gap spectrum - The eigenvalue μ versus Bloch momentum k, with the first band in red dashed line, the second band in blue dotted line, and the third band in green solid line. First row for $V_0 = 1.0$: (a) $\tau_0 = \tau_1 = 0$; (b) $\tau_0 = \tau_1 = 0.8$; (c) $\tau_0 = \tau_1 = 1.6$. Second row for $V_0 = 1.7$: (d) $\tau_0 = \tau_1 = 0$; (e) $\tau_0 = \tau_1 = 0.8$; (f) $\tau_0 = \tau_1 = 1.6$. Third row for $V_0 = 2.4$: (g) $\tau_0 = \tau_1 = 0$; (h) $\tau_0 = \tau_1 = 0.8$; (i) $\tau_0 = \tau_1 = 1.6$. 146

7.3 Stationary states in a periodic potential with strength $V_0 = 1.7$. P blue (solid) line and Q red (dashed) line. First row: Two-peak gap nematicon for a_{x0}=4.8, a_{y0}=4.1 with g_x=g_y=0. (a) $\tau_0 = \tau_1 = 0$; (b) $\tau_0 = \tau_1 = 0.8$; (c) $\tau_0 = \tau_1 = 1.6$. Second row: Three-peak gap nematicon for a_{x0}=5.6, a_{y0}=4.8 with $\tau_0 = \tau_1 = 0.8$. (d) g_x=g_y=0.5; (e) g_x=g_y=1.5; (f) g_x=g_y=3.8. Third row: Four-peak gap nematicon for a_{x0}=9.8, a_{y0}=9.1 with $\tau_0 = \tau_1 = 1.6$. (g) g_x=g_y=2.0; (h) g_x=g_y=5; (i) g_x=g_y=8.6. 149

7.4 Evolution of a two-peak gap nematicon for an initial excitation with a_{x0}=4.8, a_{y0}=4.1, w_{x0}=12, w_{y0}=12, σ_{x0}=0, σ_{y0}=0, g_x=0, and g_y=0 in a periodic potential with strength $V_0 = 1.7$. First column [(a), (c), (e)]: Evolution of R. Second column [(b), (d), (f)]: Evolution of S. First raw: $\tau_0 = \tau_1 = 0$ and $\mu = 1.9$. Second raw: $\tau_0 = \tau_1 = 0.8$ and $\mu = 2.4$. Third raw: $\tau_0 = \tau_1 = 1.6$ and $\mu = 3.3$. 152

7.5 The thermal response coefficients versus separation between peaks of two-peak gap nematicon. 153

7.6 Evolution of a three-peak gap nematicon for an initial excitation with a_{x0}=5.6, a_{y0}=4.8, w_{x0}=12, w_{y0}=12, σ_{x0}=0, and σ_{y0}=0 in a periodic potential with strength $V_0 = 1.7$. First column [(a), (c), (e)]: Evolution of R. Second column [(b), (d), (f)]: Evolution of S. First row: g_x=g_y=0.5. Second row: g_x=g_y=1.5. Third row: g_x=g_y=3.8. In all three rows, $\tau_0 = \tau_1 = 0.8$ and $\mu = 3.6$. 154

7.7 Evolution of a four-peak gap nematicon for an initial excitation with a_{x0}=9.8, a_{y0}=9.1, w_{x0}=12, w_{y0}=12, σ_{x0}=0, and σ_{y0}=0, in a periodic potential with strength $V_0 = 1.7$. First column [(a), (c), (e)]: Evolution of R. Second column [(b), (d), (f)]: Evolution of S. First row: g_x=g_y=2. Second row: g_x=g_y=5. Third row: g_x=g_y=8.6. In all three rows, $\tau_0 = \tau_1 = 1.6$ and $\mu = 6.4$. 158

7.8 The results of linear stability analysis of the system in a periodic potential with the strength of $V_0 = 1.7$. Stability analysis of two-peak gap nematicons for (a) $\tau_0 = \tau_1 = 0$; (b) $\tau_0 = \tau_1 = 0.8$; (c) $\tau_0 = \tau_1 = 1.6$. The real and imaginary parts of the perturbation eigenvalues (λ) versus the propagation constant μ are displayed. 161

7.9 The results of linear stability analysis of the system in a periodic potential with the strength of $V_0 = 1.7$. Stability analysis of three-peak gap nematicons for $\tau_0 = \tau_1 = 0.8$: (a) g_x=g_y=0.5; (b) g_x=g_y=1.5; (c) g_x=g_y=3.8. The real and imaginary parts of the perturbation eigenvalues (λ) versus the propagation constant μ are displayed. 161

7.10 The results of linear stability analysis of the system in a periodic potential with the strength of $V_0 = 1.7$. Stability analysis of four-peak gap nematicons for $\tau_0 = \tau_1 = 1.6$: (a) g_x=g_y=2; (b) g_x=g_y=5; (c) g_x=g_y=8.6. The real and imaginary parts of the perturbation eigenvalues (λ) versus the propagation constant μ are displayed. 161

List of Tables

4.1 The strength of parabolic potential and the corresponding wavelength of periodic oscillations of higher harmonics of nematicons. 89

5.1 Thermal response coefficients and the corresponding wavelength (μm) of periodic oscillations of double-peak nematicon. 106

7.1 Thermal response coefficients and the corresponding seperation between peaks of two-peak gap nematicon. 153

Preface

Nonlinear systems do not obey the superposition principle. Nonlinear phenomena abound in the nonlinear world, and optics is one of the most accessible fields for studying them. When light and matter interact, the former can alter the medium properties, particularly the refractive index, affecting its own propagation. We look at a nonlinear process termed self-confinement. It is the ability of a light beam to compensate for its natural tendency to spread. Solitons are formed when a nonlinear process balances the linear dispersive or diffractive effects of a medium. Solitons retain their shape during propagation, making them excellent choices for carrying and processing other signals, like waveguides. A balance between nonlinear self-focusing and linear diffractive spreading produces spatial solitons. We deal with nematicons which are the spatial optical solitary waves in nematic liquid crystals (NLCs). These are diffractionless self-confined light beams in which diffraction is balanced by self-focusing via nonlinearity. Nonlinearity in NLC can take place via dipolar interactions between molecules and electric fields. NLCs have been selected because they are an excellent medium for investigating nonlinear processes, particularly because of their high and nonlocal response to electric fields. The nematicons are widely used in all-optical interconnects, readdressable configurations, all-optical steering, and routing devices.

This thesis investigates the nonlinear beam dynamics in uniaxial nematic liquid crystals under the influence of temperature, diffractive radiation, and potentials. The equations governing the nonlinear optical beam propagation in NLCs are a coupled system consisting of (2+1)D nonlinear Schrodinger-type equation for the optical beam and an elliptic Poisson equation for the molecular director. Semi-analytical and numerical methods are employed for the analysis. The variational method based on Lagrangian density is used as the semi-analytic method for studying the system. The finite-difference method, Runge-Kutta method, and pseudo-spectral methods are applied.

Chapter 1 provides an overview of liquid crystals and nematicons. This chapter also covers the governing equations of nematicons. The methodology for analyzing beam propagation through uniaxial NLC is also described in this chapter. Both the semi-analytical and numerical methods are discussed.

Chapter 2 examines the interplay between diffractive radiation shed and damping coefficient in a nematic liquid crystal with nonlocal nonlinearity. The system is analyzed using semi-analytical and numerical methods. The beam propagation under three types of damping such as constant, periodic, and hyperbolic profiles is studied. The influence of diffractive radiation shed on nematicon propagation has also been analyzed.

The thermal responses of single-peak and double-peak solitons in a nematic liquid crystal have been studied numerically in Chapter 3. The study also examines how the competition between focusing reorientational and defocusing thermal nonlinearities results in the formation of single-peak and double-peak nematicons. The stability of the stationary solutions against small perturbations has been studied employing Bogoliubov-de Gennes equations.

The behavior of nonlocal spatial optical solitons in a uniaxial nematic liquid crystal with a parabolic potential is investigated in Chapter 4. The equations governing the system are solved using semi-analytic and numerical methods. This chapter also discusses the effect of the parabolic potential on the formation of higher harmonics of nematicons. The stability of the stationary states is also analyzed.

Chapter 5 deals with the thermal response of nematicons in a parabolic potential. The study investigates how the energy landscape experienced by the light beam within the medium is modified by the competing nonlinearities. The formation of single-peak and double-peak nematicons as well as the effect of parabolic potential on the periodic oscillations of nematicons are analyzed. This chapter also looks at the impact of thermal response coefficients on the wavelength of the oscillation of double-peak nematicon. The stability of the stationary solutions against small perturbations has been studied employing linear stability analysis.

Chapter 6 investigates the formation and stability of single-peak and multi-peak gap nematicons using numerical methods. Both the stationary solutions and the dynamic solutions have been studied in the first band gap. The range of propagation constants at which the single-peak gap nematicons and the multi-peak gap nematicons can exist are discussed. The study also investigated how the intensity distribution among various peaks in a multi-peak gap nematicon depends on input beam intensity. The stability of the stationary solution against small perturbations has been studied using Bogoliubov-de Gennes equations.

Chapter 7 deals with the effects of thermal response and diffractive radiation on multi-peak gap nematicons. The chapter explores both stationary and dynamic solutions, focusing on the formation and evolution of multi-peak structures under varying thermal response coefficients and diffractive radiation shelf heights. The study analyzes the interplay among thermal effects, refractive index changes, and diffractive radiation which influences the configuration and dynamics of the gap nematicons. The stability of stationary solutions against small perturbations has also been investigated.

The results and conclusions of the thesis are summarised in Chapter 8. This chapter briefly discusses future research avenues in NLC and other optical media.

List of Abbreviations

NLC	Nematic Liquid Crystal
KdV	Korteweg de Vries
LCD	Liquid Crystal Display
TN	Twisted Nematic
IPS	In-Plane Switching
PDLC	Polymer-Dispersed Liquid Crystal
CW	Continuous-Wave
NLSE	Nonlinear Schrodinger Equation
ODE	Ordinary Differential Equation
BDG	Bogoliubov-de Gennes
CNTs	Carbon Nanotubes
SLMs	Spatial Light Modulators

Chapter 1

Introduction

Waves are fundamental aspects of nature and can be observed all around such as water waves, sound waves, and light waves. In most cases, these systems are analyzed and solved under linear conditions where the principle of superposition is applicable. However, many intriguing effects and phenomena occur in the nonlinear regime. Nonlinear media are characterized by a polarization density that responds nonlinearly to the electric field of light, and the field of nonlinear optics studies how light behaves in such media. Nonlinear effects typically become noticeable only under high-intensity light such as that generated by lasers. Nonlinear optics explains how properties like frequency, polarization, phase, and the propagation path of light are altered in response to this nonlinear interaction [1].

1.1 Solitons

Solitary waves are localized waves that maintain their shape during propagation due to a precise balance between linear and nonlinear effects in the medium [2]. The phenomenon of solitary waves was first observed by John Scott Russell in 1834 when he noticed a wave moving through Edinburgh Union Canal that retained its form as it traveled. This observation marked the first recorded instance of what we now call a soliton [3]. Later Boussinesq and Rayleigh demonstrated that such “solitary waves” could emerge from water wave equations. In 1895, Korteweg and de Vries formulated what is now known as the Korteweg-de Vries (KdV) equation, which approximately describes long waves in shallow water. The term “soliton” was introduced by Zabusky and Kruskal to refer to the solitary wave solutions of the KdV equation recognizing that these solutions exhibited particle-like properties [4]. A soliton is a solitary wave that preserves its shape while traveling at a constant velocity. Figure (1.1) illustrates the soliton profile, demonstrating how the shape of the wave remains unchanged during propagation.

In fiber optics, solitons have been employed as information carriers or “bits” in various experiments. Their inherent stability makes them ideal for transmitting information over long distances [5, 6]. The robust and stable nature of solitons has led to their widespread use across several fields including physics, hydrodynamics, photonics, biology, and chemistry [7].

A soliton forms when there is a balance between nonlinear and dispersive or diffractive effects within a medium. There are mainly two categories of solitons. They are temporal and spatial solitons. When the nonlinear phase modulation is balanced with the linear dispersion, temporal solitons are formed. If the nonlinear self-focusing counteracts with the linear diffractive spreading, then spatial solitons are formed.

Solitons are particularly useful in systems with strong nonlinearity. Their importance stems from their unique properties as nonlinear waves as well as their function as nonlinear excitations in condensed matter systems. Liquid crystals are one of the systems in which the nonlinear interactions lead to the formation of solitons. The velocity of the fluid and the molecular orientation play crucial roles in liquid crystals. This thesis focuses on the formation, propagation, and remarkable features of optical spatial solitons in nematic liquid crystals.

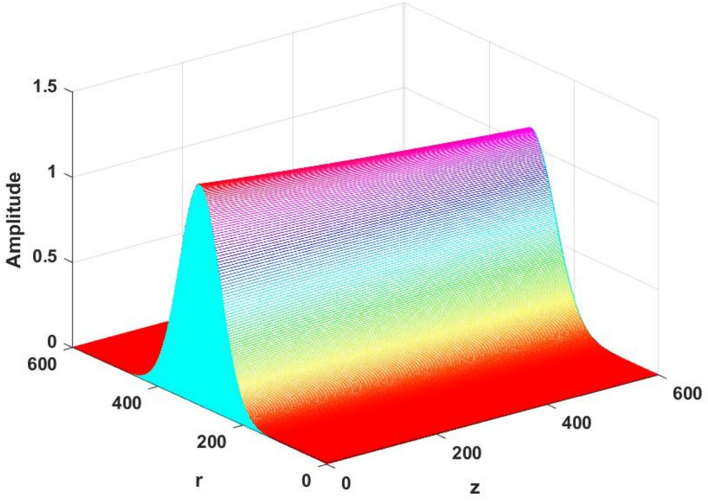

Figure 1.1: Soliton profile

1.2 Liquid Crystals

Matter is typically categorized into four distinct states such as solid, liquid, gas, and plasma. Solids can exist in either a crystalline or amorphous form. The key characteristic that differentiates solids from liquids is their ability to flow. While liquids can flow and adapt to the shape of their container, solids maintain their form and do not flow. Additionally, the optical properties of some solids and liquids vary significantly. For instance, certain solids can alter the polarization of light whereas liquids generally do not exhibit this property. Due to these early concepts, researchers initially did not recognize the existence of other phases even though they encountered substances that did not fit neatly into the established categories. Continued investigations revealed that the observed intermediate phases represent a distinct thermodynamic state of matter, separate from the isotropic liquid. These phases exhibit mechanical and symmetry properties that are between those of a crystalline solid and an isotropic liquid. Lehmann first described them as flowing crystals, later coining the term “liquid crystals” [8]. Figure (1.2) illustrates the molecular arrangements in solids, liquid crystals, and liquids, with yellow ellipses representing the molecules.

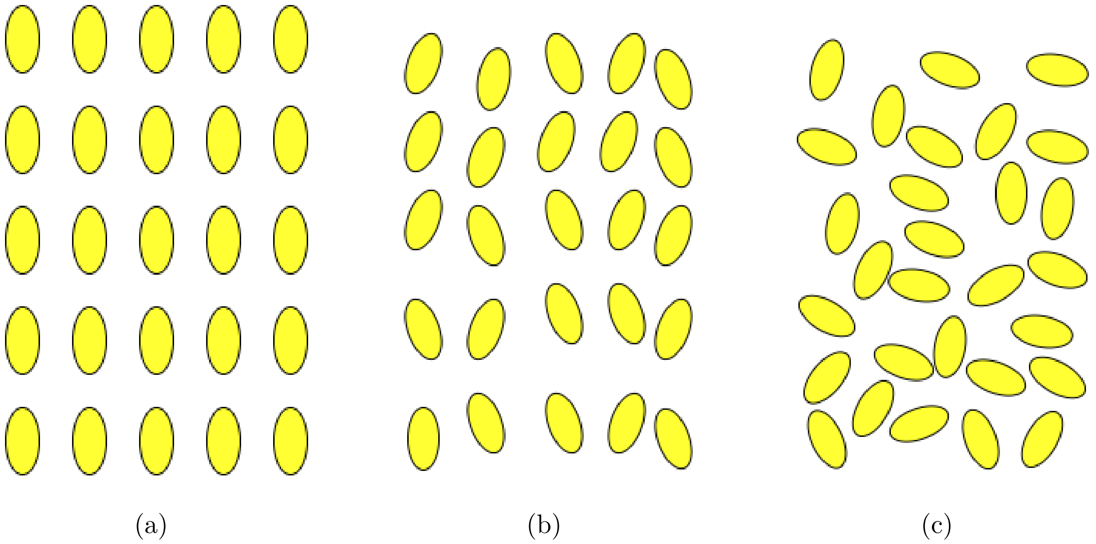

(a) (b) (c)

Figure 1.2: The arrangements of molecules in (a) solids, (b) liquid crystals, and (c) liquid are shown. The molecules are represented by yellow-colored ellipses.

A crystal is defined as a structure where objects are arranged in a three-dimensional lattice, resulting in periodic density in all three spatial directions. The intermediate state between a liquid and a crystal is referred to as a liquid crystal, also known as mesophases [8]. The nature of these mesophases varies because they can lose periodicity in one, two, or all three spatial directions based on factors such as temperature, pressure, and chemical composition. Columnar phases, often called discotic phases, lose their crystalline structure in one direction when partially melted. If the crystalline order is disrupted in two dimensions, they form stacks of two-dimensional liquids. These arrangements are classified as smectics[9]. Even if the system melts in all three directions, it doesn't necessarily become an isotropic fluid. Anisotropic correlations like nematic correlations may still exist. The key point is that even though the translational order is absent, the long axes of the molecules align in a common direction [10]. Depending on the level of molecular organization, various liquid crystal (LC) phases exist with the least ordered phase typically known as 'nematics' [11]. This phase is composed of nematic liquid crystals (NLCs) where the rod-shaped molecules lack positional order but are aligned in parallel due to intermolecular forces [12]. Consequently, NLC molecules can flow and arrange themselves randomly like a liquid while preserving long-range directional alignment. Liquid crystals can be categorized as thermotropic or lyotropic depending on whether temperature or concentration predominantly influences the phase transitions [13].

Liquid crystals are experiencing a resurgence in both fundamental research and technological advancements, becoming an integral part of modern life. They possess unique properties due to the partially ordered phases and anisotropy which are essential for various applications in micro-electronics and opto-electronics [14–16]. The liquid crystal displays (LCD) which are widely used in electronic devices, rely on liquid crystals to generate visual effects on screens [17]. LCDs are integral to devices such as televisions, computer monitors, smartphones, and digital watches. Their core functionality is based on the ability of liquid crystals to control light transmission when exposed to an electric field, enabling the creation of high-resolution images. Techniques like twisted nematic (TN) and in-plane switching (IPS) are commonly employed to achieve enhanced image quality and broader viewing angles [18]. LCD technology continues to advance with the production of thinner, lighter, and more energy efficient displays.

Liquid crystals are widely employed in optical modulators because they can modify the polarization and phase of light when exposed to external electric fields. These modulators play crucial roles in applications such as telecommunications, laser technology, and optical signal processing. Additionally, LCs can serve as optical switches, directing or altering the properties of light, which is vital for reconfigurable photonic circuits and all optical signal routing [19]. Furthermore, LCs are utilized in thermography and medical imaging where their temperature sensitive nature allows them to change color in response to temperature fluctuations. This property makes them ideal for thermal mapping which is used to identify abnormal heat patterns in the body, often linked to diseases such as cancer or vascular disorders [20]. Liquid crystal thermography is a noninvasive technique that provides real-time imaging of temperature distribution [21, 22]. Optical attenuators and wavelength-selective switches, which are made of liquid crystals, are used to control light signals through optical fiber networks in telecommunication systems. Their tunability under electric fields allows for precise control over light transmission optimizing the performance and efficiency of fiber optic systems [23]. In nonlinear optics, LCs are gaining attention for their ability to support solitons which are localized waves that maintain their form while propagating, thanks to the balance between nonlinearity and dispersion. Nematicons are spatial solitons found in NLCs and they are explored due to their applications in optical switching, waveguiding, and signal processing. The self focusing and beam guiding properties of LCs make them highly beneficial for use in nonlinear photonic devices [12].

1.2.1 Nematic Liquid Crystals

The molecules in a nematic liquid crystal phase tend to point in a common direction despite having no positional order [19]. A mesogen is an elongated or rod-like molecule with anisotropic properties that forms the structural basis of LCs. Most NLCs have an optic axis that corresponds to the molecular director or the average orientation of the long axes. As a result, the majority of NLCs are uniaxial. Figure (1.3) depicts the mesogen alignment of a nematic liquid crystal. This diagram shows that mesogens prefer to order in the direction of the director n. The molecular director n is a unit vector that represents the average direction of the molecules.

The angular distribution of the molecules around the direction of the director is described in the nematic phase by the orientational order parameter S. A Legendre polynomial of second order is commonly used to define it [24],

$$S = \frac{1}{2}\left\langle 3cos^2\alpha - 1\right\rangle, \tag{1.1}$$

where the average is calculated over the total solid angle. The angle between the director and the long molecular axis is denoted by α. If all the molecules are parallel to n, then α=0 or $\alpha=\pi$. It yields order parameter S=1. When the molecules are randomly aligned, S=0 and the LC becomes an isotropic liquid.

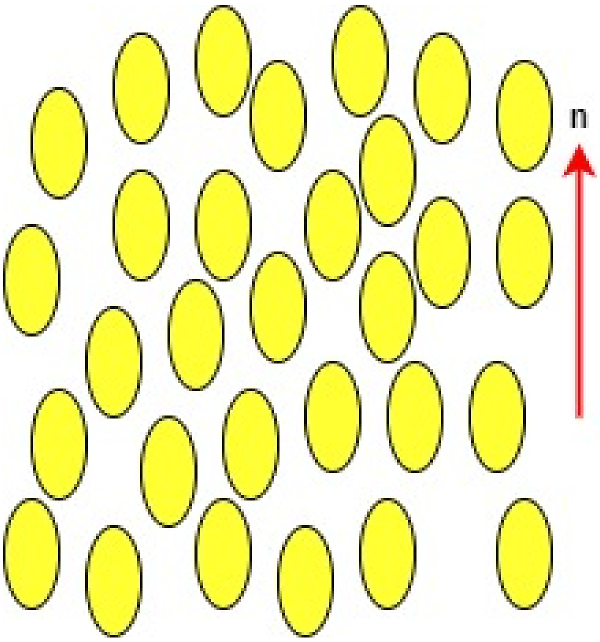

Figure 1.3: The mesogen alignment of a nematic liquid crystal is shown. The mesogens prefer to order in the direction of the director n.

The order parameter of an LC is typically between 0.3 and 0.9.

The refractive indices for light polarised parallel to n and perpendicular to n are different because nematic molecules are rod-like. The dielectric tensor ϵ of the nematic can be used to define the refractive indices of the NLC parallel and perpendicular to n [25]. ie,

$$n_{\parallel} = \sqrt{\frac{\epsilon_{\parallel}}{\epsilon_0}}, \qquad n_{\perp} = \sqrt{\frac{\epsilon_{\perp}}{\epsilon_0}}, \tag{1.2}$$

where ϵ_0 stands for vacuum dielectric permittivity. The macroscopic behavior of NLC is equivalent to a positive uniaxial anisotropy [26],

$$\epsilon_a = \epsilon_{\parallel} - \epsilon_{\perp}. \tag{1.3}$$

Only LC with positive anisotropy is considered in this thesis. Ordinary polarised light propagates as it does in isotropic media with a refractive index $n_0 = n_{\perp} = \sqrt{\epsilon}_{\perp}$. Extraordinary polarised light has a refractive index that is related to the angle (θ)

between the director and the wave vector [27],

$$n_e = \sqrt{\frac{n_{\perp}^2 n_{\parallel}^2}{n_{\perp}^2 sin^2\theta + n_{\parallel}^2 cos^2\theta}}. \tag{1.4}$$

The order parameter influences the refractive indices. Although the molecules should be arranged in a common direction, interactions with confining boundaries and/or external magnetic or electric fields cause this organization to deform, changing the order parameter. Splay, twist, and bend are the three types of common deformations. Since these deformations take place on scales that are much larger than molecular size, elastic continuum theory is applicable and they can be regarded as constants everywhere. When the director alignment is homogeneous and the director is perpendicular to the applied field, the molecules reorient above an intensity threshold known as the Frederick threshold [28].

A nematic liquid crystal alters the polarisation of light waves as they pass through it. The magnitude of the polarisation change is determined by the strength of an applied electric field. Nematic is derived from the Greek prefix nemato, which means thread like, and is used here because the molecules in the liquid align into a threadlike shape. Twisted nematic displays are the most common type of liquid crystal display which are made up of nematic liquid crystals [29]. NLCs offer numerous applications in light modulators, random lasers, liquid crystal displays, and optical communication systems [30, 31]. E7 is a widely used NLC mixture. It is an ideal platform for studying various nonlinear optical phenomena because of its favorable electro-optic properties.

1.2.2 E7 NLC

E7 is a common mixture of nematic liquid crystal which is used in display technologies and other electro-optical applications. E7 holds certain peculiarities that distinguish it from other liquid crystals and make it particularly suited for soliton studies. It is a eutectic mixture of several different liquid crystal compounds, typically a combination of cyanobiphenyls and cyanoterphenyls. It consists of 51% 5CB (4-cyano-4'-pentylbiphenyl), 25% 7CB (4-cyano-4'-heptylbiphenyl), 16% 8OCB (4-cyano-4'-octyloxybiphenyl), and 8% 5CT (4-cyano-4'-pentylterphenyl) [32]. This specific blend optimizes its optical and thermal properties, making it widely used in liquid crystal displays, photonics, and nonlinear optics.

Temperature Dependence

The temperature dependence of the refractive indices for E7 liquid crystal shows distinct behavior across a temperature range of 20°C to 55°C [33]. From 20°C to 40°C, the refractive indices exhibit a relatively weak, linear variation: the refractive index parallel to the director ($n_{\|}$) decreases by 0.6%, while the index perpendicular to the director ($n_{\perp}$) increases by 1.3%. This weak dependence reflects the modest influence of temperature on the molecular ordering in the nematic phase. However, from 40°C to 55°C, the temperature dependence becomes more pronounced with additional quadratic and cubic terms emerging in the refractive index variations. These changes are attributed to the increased thermal motion of the molecules and the approaching transition to the isotropic phase where molecular order is lost.

Dielectric Anisotropy

The dielectric constant of the E7 is greater if an electric field is applied parallel to the director than it is applied perpendicular to it. This property makes E7 suitable for use in devices like liquid crystal displays (LCDs), as it enables the liquid crystals to reorient in response to applied electric fields [34].

Optical Anisotropy

E7 possesses different refractive indices depending on the direction of light propagation relative to the molecular alignment. This optical anisotropy is known as birefringence [35]. This anisotropy is critical for the optical modulation in

LCDs. E7 shows this property in the visible range. Hence E7 is suitable for LCD applications where the controlled manipulation of light is essential.

Viscosity

E7 has relatively low viscosity which allows for fast switching times in liquid crystal devices. Viscosity is temperature dependent and influences the response time of the liquid crystal when external fields are applied [36].

Chemical Stability

E7 is chemically stable and does not easily degrade under light exposure, making it suitable for long-term use in display technologies [37]. Experimental studies indicate that E7 can endure light intensities commonly used in display technologies such as up to 95 mW/cm^2 during UV curing processes as seen in advanced liquid crystal applications like polymer-dispersed liquid crystal devices [38].

Elastic Constants

Molecular alignment in LCs can undergo three primary types of deformations: splay, twist, and bend. These deformations describe how the molecular director is distorted under external forces such as electric or magnetic fields [39].

Splay Deformation: Splay occurs when the molecular director spreads radially outward or inward leading to a divergence in the alignment. This type of deformation is often observed in the presence of curved boundaries or non-uniform electric fields. The resistance to splay is quantified by the elastic constant K_1, and it is essential in understanding how liquid crystals respond to surface anchoring effects [40].

Twist Deformation: Twist deformation takes place when the director rotates around an axis perpendicular to its initial orientation forming a helical structure. This deformation is common in twisted nematic (TN) displays where alignment layers impose opposite molecular orientations at the boundaries. The elastic constant K_2 measures the energy required to resist twisting [40, 41].

Bend Deformation: Bend deformation happens when the molecular director curves into an arc-like shape. This type of distortion often arises when the alignment transitions smoothly over a distance but is curved rather than straight. The resistance to bending is represented by K_3, which is typically the largest of the three elastic constants [40].

These elastic deformations and their associated constants determine how nematic liquid crystals behave under external influences, making them crucial for designing optical and electro-optic devices such as liquid crystal displays and tunable lenses.

Tunable Refractive Index

The refractive index of E7 can be controlled using an external electric field allowing researchers to precisely adjust the propagation conditions for light [42]. This tunability provides a versatile platform for manipulating and guiding solitons.

Low Power Requirement

The nonlinear effects in E7 NLCs can be achieved with relatively low light power compared to other nonlinear media like optical fibers[37]. This is advantageous because it makes experiments more accessible and reduces the need for high-intensity lasers.

Soliton Interactions

The properties of E7 allow for the study of various types of solitons including spatial, temporal, and light bullets (spatio-temporal solitons). The controllability of the refractive index and molecular alignment enables detailed investigations into soliton interactions, collisions, and stability in different configurations [35].

Applications of E7 NLC

E7 NLC is known for its high birefringence and positive dielectric anisotropy which enable its use in a variety of applications, including display technologies, privacy windows, and optical shutters [34, 35, 38]. As a eutectic mixture, it is commonly integrated into polymer-dispersed liquid crystal (PDLC) materials, particularly for systems operating under normal mode conditions [43, 44]. The material's stable nematic phase along with its optical and dielectric properties, make it ideal for twisted-nematic and in-plane switching display technologies [32]. Furthermore, E7's versatility extends to electro-optic applications such as optical modulators and tunable lenses [45]. These properties combined with its low power requirements, make E7 indispensable for modern display and optical systems [39]. Its ability to respond to temperature variations and external influences also makes it an excellent platform for studying solitons with the current focus on investigating nematicons in this material.

1.3 Nematicons

Spatial optical solitons in nematic liquid crystal are known as nematicons. G. Assanto coined the name in 2003 [29]. When a light source enters an optically dense medium, the optical beam linearly diffracts. On the other hand, the optical beam can cause a local change in the refractive index of the NLC resulting in the optical beam self-focusing. Figure (1.4) depicts linear diffraction and self-focusing. The balance of these two optical effects results in the formation of a nematicon.

Reorientational nonlinearity is a nonlinear optical response of birefringent molecular crystals in the fluid state that can be seen in uniaxial nematic liquid crystals such as E7 NLC. NLCs are made up of molecules that are angularly aligned, nonpolar, and anisotropic. Elastic forces hold these molecules together. They will rotate in space in the presence of strong electric fields due to an increase in refractive index resulting in beam self-focusing. When a polarised light beam of sufficient intensity passes through the NLC, a torque is produced as a result of the reaction of optically induced dipoles of the electric field vector [29]. The torque-induced change in molecular angular orientation reduces the energy and phase speed of extraordinary polarized waves. The nonlinear refractive

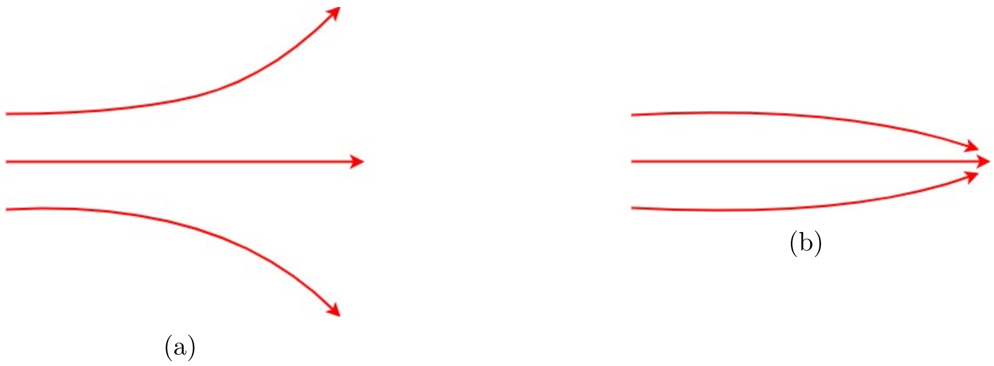

Figure 1.4: (a) Pure linear diffraction, (b) self-focusing of an optical beam.

index redistribution is more pronounced where the beam intensity is greater. Additionally, it is nonlocal due to the possibility of a graded potential with light guiding properties emerging from the intermolecular links in the fluid. NLC behaves as a waveguide that prevents beam diffraction and allows for stable spatial solitons. The optical properties of the nematic have been influenced by a refractive index which is determined by a tensor response. This tensor yields two eigen directions for a uniaxial NLC, known as ordinary and extraordinary waves. Because ordinary waves are non-dispersive, they do not form solitary waves. The extraordinary waves, on the other hand, are dispersive and can form solitary waves. The extraordinary response of the NLC then results in the formation of a nematicon [25]. Nematicons are such linearly polarised solitary waves in NLCs. Nematicons are simple to produce with mW optical power or less because the NLC dielectric medium has the following properties [19]:

(i) Very large nonlinear response: Only a small amount of optical power is required to achieve refractive index variation or self-focussing to compensate for diffraction.

(ii) Nonlocal response: The profile of nonlinear response is wider than that of light beam. As a result of the high nonlocality, stable solitons can propagate even in the case of two transverse dimensions.

(iii) All optical saturable response: When the electric field of a light beam enters the NLC, director of the liquid crystal has a tendency to align with the direction of the incident field. For powerful beams, the molecular director aligns with the field and further reorientation is not possible. Two dimensional solitons are stabilised as a result of this response saturation.

1.4 Literature Review

Nematicons or self-localized beams in nematic liquid crystals have been extensively studied due to their fascinating nonlinear properties and potential applications in photonics.

The concept of nematicons emerged when researchers observed that light beams could form self-focused channels in nematic liquid crystals due to the material's optical nonlinearity. The fundamental work by Assanto et al. in 2003 demonstrated that light-induced molecular reorientations in nematic liquid crystals led to the formation of spatial solitons [19]. This marked the foundation of nematicon research showing that nematicons could propagate over long distances without diffraction due to the balance between diffraction and nonlinear effects in the medium. In 2003, G. Assanto introduced the term "nematicon" to describe the distinctive waveforms that result from the reorientation of the molecular director under the influence of optical fields. Continuous-wave (CW) beams operating at milliwatt levels can create nematicons which are characterized by their extraordinary polarized wave packets in uniaxial NLCs maintaining electric field oscillations in the plane defined by the optic axis and wave vector [12].

The propagation of nematicons relies on the nonlinear optical response of NLCs. Subsequent studies explored how different parameters such as beam power, polarization, and the physical properties of the material affect nematicon behavior. Experiments showed that nematicons are highly sensitive to these parameters and through careful control, it is possible to manipulate the trajectory and interaction of these self-focused beams. These studies expanded on the initial findings, offering insights into beam propagation dynamics in complex liquid crystal environments [46].

The unique properties of nematicons have made them a promising candidate for use in photonic devices particularly in optical switching and signal routing. Studies have shown that nematicons can be steered by external electric fields allowing dynamic control over their path. This has opened the door to potential applications in reconfigurable photonic circuits where nematicons could be used for signal processing and data transmission [47].

Research into nematicon interactions revealed that they exhibit soliton-like behavior allowing them to collide, fuse, or repel depending on their initial conditions. The study of these interactions has provided deeper insights into soliton dynamics in soft matter systems. Numerical and experimental investigations have highlighted the role of nonlinearities and boundary conditions in determining the outcomes of nematicon interactions [48].

More recent research has focused on improving the control and stability of nematicons by utilizing advanced material compositions and external manipulation techniques. These studies aim to enhance the robustness of nematicons for practical applications in optical communications and sensing technologies. Additionally, researchers are investigating the use of nematicons in new types of optical materials such as chiral liquid crystals which exhibit unique nonlinear behaviors [1, 49].

Thermo-reorientational nematicons are self-focused light beams that form in NLC under the combined influence of optical and thermal effects. These beams leverage the nonlinear optical response of the material driven by the reorientation of liquid crystal molecules and temperature gradients due to the absorption of light. Initial studies on thermo-reorientational nematicons were built upon the foundational understanding of nematicons in liquid crystals. The inclusion of thermal effects was explored to account for the broader nonlinear responses in liquid crystal systems. Researchers discovered that the absorption of light in NLC could lead to local temperature increases which in turn enhanced the reorientational response of the molecules affecting the formation and dynamics of nematicons [50]. The thermo-optic effect where the refractive index changes due to temperature variations became a key area of investigation in the study of thermo-reorientational nematicons. This effect was shown to further enhance the nonlinearity in NLC, leading to more robust self-trapped beams. Studies demonstrated that as light propagates through the material, the absorption induced heating causes molecular reorientation, altering the local optical properties. This interplay between thermal and optical reorientation was crucial in understanding the enhanced nonlinearity in these systems [51].

Experimental investigations provided deeper insight into how thermal effects could be harnessed to control nematicon formation and propagation. For instance, researchers showed that increasing the power of the laser beam not only enhanced the optical reorientation but also significantly increased the local temperature, strengthening the beam confinement through the thermo-optic effect. Alberucci et al. experimentally demonstrated that thermal contributions could lead to more pronounced beam self-localization, particularly in the case of continuous-wave (CW) laser sources where thermal diffusion becomes dominant over optical reorientation alone [52].

Theoretical models were developed to describe the complex interactions between optical and thermal effects in nematic liquid crystals. These models integrated the thermal conductivity of the material, light absorption, and molecular reorientation dynamics. Assanto and Smyth provided a comprehensive theoretical framework to predict the behavior of thermo-reorientational nematicons which accounted for the temperature-dependent nonlinearities and their impact on soliton formation. This modeling helped to explain the experimental results and guided further research into optimizing the control of thermo-reorientational effects [53].

Recent studies have also examined the impact of linear absorption on the stability of nonlinear vortex beams in dye-doped nematic liquid crystals [54]. Dye-induced light absorption leads to a complex nonlinear optical response characterized by spatially nonlocal focusing and defocusing contributions. The anomalous interaction of spatial solitons influenced by the competition between these nonlinearities has been explored in recent works [55]. The breathing solitons exhibit significant deformation in the presence of a self-focusing saturable nonlinearity, while the introduction of a defocusing nonlinearity results in the formation of couples of solitons [56].

The increased control over nematicons through thermal reorientation opened up new possibilities for their application in photonics. Thermo-reorientational effects enabled more dynamic control over beam propagation, making these systems suitable for use in tunable photonic devices such as optical switches, modulators, and sensors. These studies highlighted the potential of using thermal gradients to manipulate light in liquid crystal based devices, paving the way for innovative designs in optical communication and signal processing [53].

Solitons in periodic media are an important topic in science and engineering [57]. The gap soliton is a type of localized wave that forms in nonlinear optical media when the refractive index changes periodically [58]. These solitons exist in the forbidden frequency band where linear waves cannot travel. They are stable due to the balance between the medium's nonlinearity and its periodic structure. In materials like liquid crystals and photonic crystals, gap solitons often appear near the edges of spectral bands and show unique stability properties [59]. They are useful for technologies such as optical switches, soliton lasers, pulse compressors, and optical buffers [60–62]. An optical switching mechanism proposed by researchers [58] relies on the transmission of coupled gap solitons in nonlinear periodic dielectric media which could lead to a compact all-optical switch with high performance including fast switching speeds, optimal pulse widths, and strong on-off intensity ratio. Previous studies have also examined the stability of two-dimensional gap solitons near the edges of Bloch bands in a sinusoidal lattice potential considering both focusing and defocusing cubic Kerr nonlinearities [61]. Furthermore, research has explored gap solitons and nonlinear Bloch waves within a nonlinear fractional-order quantum coupler influenced by periodic potential [62]. More recent studies have expanded on the potential practical applications of gap solitons in integrated photonic devices. These include their use in tunable optical circuits and all-optical signal processing. The use of gap solitons in nonlinear photonic crystals and metamaterials has opened new avenues for research with ongoing studies focusing on enhancing their performance and broadening their application in photonic technologies [62].

In parallel with experimental efforts significant progress has been made in the theoretical and numerical modeling of nematicons. Various models have been developed to describe the nonlinear propagation of light in nematic liquid crystals considering the anisotropy of the material and nonlocal effects. These models have been instrumental in predicting the behavior of nematicons under different conditions and guiding experimental research. Nonlocal models have proven crucial in understanding the long-range interactions between nematicons and their surroundings, providing a deeper understanding of their stability and robustness in real-world applications [63].

The body of literature on nematicons highlights their importance in the field of nonlinear optics and photonics. Nematicons have been the subject of extensive research from their initial discovery to modern applications in photonic circuits. Their ability to self-localize, interact, and be controlled by external fields makes them highly promising for future technologies in optical communications and signal processing. Ongoing research continues to refine our understanding of nematicon dynamics and expand their potential applications in advanced photonic systems.

1.5 Governing Equations

The Maxwell's equations are a group of coupled partial differential equations which characterize the general evolution of electromagnetic waves. McLaughlin et al showed that Maxwell's equations could be reduced to a Helmholtz equation coupled with a Poisson equation for a light beam propagating in NLC [64]. Further investigation revealed that the Helmholtz equation could be converted into a nonlinear Schrodinger equation for beam propagation and a Poisson equation for medium response [24, 25]. Figure (1.5) depicts the interaction geometry of

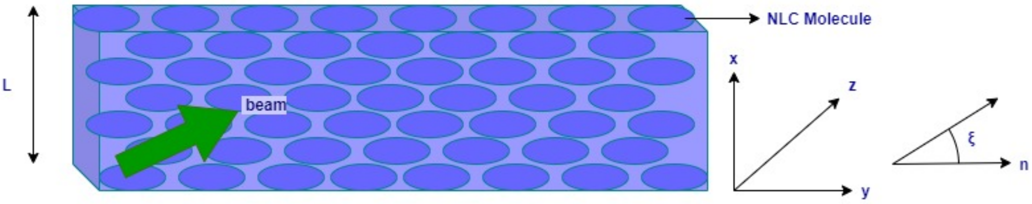

Figure 1.5: The figure of the considered sample and interaction geometry. L represents the thickness of the NLC cell and the angle ξ denotes the reorientation of the optic axis n in the (x, y) plane.

the NLC cell. The elongated NLC molecules are represented by ellipses with their long axes aligned parallel to the y axis. The green arrow represents the input light beam impinging normally on the molecular director on the sample. The governing equations used in this work can be derived from a more general, Helmholtz-type system [65, 66]. The full Helmholtz-type model, which governs the field components E_x and E_y as well as the director angle ξ are [67, 68],

$$\begin{aligned}&\epsilon_a cos^2\xi \frac{\partial^2 E_y}{\partial x \partial y} + \frac{1}{2}\epsilon_a sin2\xi \frac{\partial^2 E_y}{\partial x^2} + (n_\perp^2 + \epsilon_a sin^2\xi)\frac{\partial^2 E_x}{\partial x^2} + n_\perp^2 \frac{\partial^2 E_x}{\partial y^2} + n_\perp^2 \frac{\partial^2 E_x}{\partial z^2} \\ &+ \frac{1}{2}\epsilon_a sin2\xi \frac{\partial^2 E_x}{\partial x \partial y} = -k_o^2 n_\perp^2 \left[(n_\perp^2 + \epsilon_a sin^2\xi)E_x\right] - k_o^2 n_\perp^2 \left[\frac{1}{2}\epsilon_a sin2\xi E_y\right], \qquad (1.5)\end{aligned}$$

$$\begin{aligned}&\epsilon_a sin^2\xi \frac{\partial^2 E_x}{\partial x \partial y} + \frac{1}{2}\epsilon_a sin2\xi \frac{\partial^2 E_x}{\partial y^2} + (n_\parallel^2 - \epsilon_a sin^2\xi)\frac{\partial^2 E_y}{\partial y^2} + n_\perp^2 \frac{\partial^2 E_y}{\partial x^2} + n_\perp^2 \frac{\partial^2 E_y}{\partial z^2} \\ &+ \frac{1}{2}\epsilon_a sin2\xi \frac{\partial^2 E_y}{\partial x \partial y} = -k_o^2 n_\perp^2 \left[(n_\parallel^2 - \epsilon_a sin^2\xi)E_y\right] - k_o^2 n_\perp^2 \left[\frac{1}{2}\epsilon_a sin2\xi E_x\right], \qquad (1.6)\end{aligned}$$

$$K\nabla^2\xi + \frac{1}{4}\epsilon_0\epsilon_a \left[(\mid E_x \mid^2 - \mid E_y \mid^2) sin2\xi + (E_x E_y^* + E_x^* E_y) cos2\xi\right] = 0. \quad (1.7)$$

E_x and E_y are the x and y components of the electric fields and ξ is the director angle. The subscripts x and y represent the partial derivatives concerning x and y respectively. z is the propagation distance. k_0 be the ordinary wave vector and ϵ_a be the birefringence of the nematic. $n_{||}$ and $n_\perp$ are the refractive indices parallel and perpendicular to the director alignment respectively. ∇^2 is the two-dimensional Laplacian. The scalar magnitude of the elastic interaction between NLC molecules is represented by K. In this study, the elastic constants corresponding to bend, splay, and twist deformations are assumed to be equal [67]. While E7 nematic liquid crystals naturally exhibit anisotropic elastic properties with distinct splay, twist, and bend elastic constants, research suggests that under certain conditions, these constants can become nearly equal.

Temperature Influence:

The elastic constants of nematic liquid crystals are temperature-dependent. Studies have shown that as temperature varies, the relative differences between the splay, twist, and bend elastic constants can decrease, leading to more comparable values. For instance, research on discotic nematic liquid crystals has demonstrated unusual temperature dependencies in elastic constants, suggesting that temperature variations can influence the relative magnitudes of these constants [69].

Engineered Mixtures:

By designing liquid crystal mixtures with specific molecular compositions, it is possible to tailor the elastic properties. Mixtures that combine different mesogenic compounds can result in elastic constants that are closer in magnitude. For example, studies on binary mixtures of nematic liquid crystals have explored how combining molecules with different dipole orientations affects elastic properties, potentially leading to more uniform elastic constants [70].

In the above mentioned configuration, using the paraxial approximation for wave packet propagation in a nonlocal uniaxial environment, the dimensional model for the evolution of the beam in the presence of nonlinear reorientation can be written as,

$$\begin{aligned} 2ik_0n_\perp\frac{\partial E_x}{\partial z}+\frac{\partial^2 E_x}{\partial x^2}+\frac{\partial^2 E_x}{\partial y^2}+k_o^2\epsilon_a E_x sin^2\xi \\ +\frac{1}{2}k_0^2\epsilon_a E_y e^{ik_0(n_\parallel-n_\perp)z}sin2\xi=0, \end{aligned} \tag{1.8}$$

$$\begin{aligned}&2ik_0n_\parallel\frac{\partial E_y}{\partial z}+\frac{\partial^2 E_y}{\partial x^2}+\frac{n_\parallel^2}{n_\perp^2}\frac{\partial^2 E_y}{\partial y^2}-k_o^2\epsilon_aE_ysin^2\xi\\&\qquad+\frac{1}{2}k_0^2\epsilon_aE_xe^{-ik_0(n_\parallel-n_\perp)z}sin2\xi=0,\end{aligned}\tag{1.9}$$

$$K\nabla^2\xi+\frac{1}{4}\epsilon_0\epsilon_a\left[2(\mid E_x\mid^2-\mid E_y\mid^2)sin2\xi+2ReE_xE_y^*e^{-ik_0(n_\parallel-n_\perp)z}cos2\xi\right]=0.\tag{1.10}$$

The various constants in the model are chosen as the material parameters of the standard E7 mixture at room temperature which is a positive uniaxial NLC with $n_\parallel$= 1.73 and $n_\perp$ = 1.53, and elastic constant K= 12pN. The equations of x and y components of the electric field of the beam are [67],

$$E_x=Xe^{ik_0n_\perp z},\qquad E_y=Ye^{ik_0n_\parallel z}.\tag{1.11}$$

Here, X and Y are the amplitudes of electric fields in two transverse directions. By substituting Equation (1.11) in Equations (1.8)-(1.10), we get

$$\begin{aligned}&2ik_0n_\perp\frac{\partial X}{\partial z}+\frac{\partial^2 X}{\partial x^2}+\frac{\partial^2 X}{\partial y^2}+k_o^2\epsilon_aXsin^2\xi\\&\qquad+\frac{1}{2}k_0^2\epsilon_aYe^{ik_0(n_\parallel-n_\perp)z}sin2\xi=0,\end{aligned}\tag{1.12}$$

$$\begin{aligned}&2ik_0n_\parallel\frac{\partial Y}{\partial z}+\frac{\partial^2 Y}{\partial x^2}+\frac{n_\parallel^2}{n_\perp^2}\frac{\partial^2 Y}{\partial y^2}-k_o^2\epsilon_aYsin^2\xi\\&\qquad+\frac{1}{2}k_0^2\epsilon_aXe^{-ik_0(n_\parallel-n_\perp)z}sin2\xi=0,\end{aligned}\tag{1.13}$$

$$K\nabla^2\xi+\frac{1}{4}\epsilon_0\epsilon_a\left[2(\mid X\mid^2-\mid Y\mid^2)sin2\xi+2ReXY^*e^{-ik_0(n_\parallel-n_\perp)z}cos2\xi\right]=0.\tag{1.14}$$

It is possible to nondimensionalize the electric fields so that $E_x = A_bX$ and $E_y = A_bY$ on an input wave packet with power P_b, amplitude A_b, and width W_b.

For a Gaussian beam [67],

$$P_b = \frac{\pi}{2} C A_b^2 W_b^2, \qquad C = \frac{1}{2}\epsilon_0 c n_e. \tag{1.15}$$

The non-dimensional equations are

$$2i\frac{\partial X}{\partial z} + \frac{\partial^2 X}{\partial x^2} + \frac{\partial^2 X}{\partial y^2} + X sin^2\xi + \frac{1}{2} Y e^{\frac{iz}{1+\gamma}} sin 2\xi = 0, \tag{1.16}$$

$$2i\gamma\frac{\partial Y}{\partial z} + \frac{\partial^2 Y}{\partial x^2} + \gamma^2\frac{\partial^2 Y}{\partial y^2} - Y sin^2\xi + \frac{1}{2} X e^{\frac{-iz}{1+\gamma}} sin 2\xi = 0, \tag{1.17}$$

$$\nu\nabla^2\xi + (\mid X \mid^2 - \mid Y \mid^2) sin 2\xi + 2Re(XY^* e^{\frac{-iz}{1+\gamma}}) cos 2\xi = 0, \tag{1.18}$$

where,

$$\gamma = \frac{n_{\parallel}}{n_{\perp}}, \qquad \nu = \frac{4Kk_0^2}{\epsilon_0 A_b^2}. \tag{1.19}$$

Here, γ and ν are the anisotropy and the nonlocality respectively. A_b is the amplitude of the input optical beam. In Equation (1.19), the parameter ν determines the intermolecular elastic link between nematic molecules. A small value of ν represents the local limit, while a large value of ν represents the nonlocal limit. In this thesis, the parameters are chosen as the nonlocality $\nu = 600$ and anisotropy $\gamma = 1.13$ [67].

1.6 Methodology

The beams which travel through a nonlocal NLC are affected by the response of the medium. The governing equations for an optical beam propagating in NLC are a coupled system with a Nonlinear Schrodinger Equation(NLSE) for the beam and a Poisson equation for the director. There is no exact solitary wave solution or any other exact solution to this system of equations. As a result, semi-analytical and numerical methods are used to solve these equations.

1.6.1 Semi-Analytical Methods

Anderson used this method for the first time in 1983 to approximate nonlinear pulse propagation in optical fibers as described by the NLSE [71]. Variational or semi-analytic approximations have been found to be useful in the absence of exact solutions with good agreement with numerical and experimental results.

The semi-analytical method is based on the trial function of the light beam and the director. The trial function has several variational parameters such as amplitude, width, phase, and shelf height. These parameters change with the propagation distance. The variational method is a very useful tool, but it has some drawbacks due to some simplifications imposed on the beam profiles. As a result, governing equations remove some important aspects of the evolution of the beam. A careful selection of trial functions is required to avoid the drawbacks of this method. Typically, a basic beam profile serves as the trial function [72]

$$E = f\left(q_1(z), q_2(z), q_3(z), ..., q_N(z)\right), \tag{1.20}$$

where the parameters are $q_i(z)$, where i = 1,...,N and N is the total number of parameters.

The variational method which yields modulation equations, will be used in this work to investigate the beam dynamics in NLCs. The calculus of variation is concerned with problems in which we seek a function or a curve, rather than the value of some variables, that makes a given quantity stationary. In most problems involving the calculus of variations, the quantity to be minimised (or maximised) can be expressed as a functional, which means that its arguments are functions rather than just variables. Let J be a functional of y, defined as

$$J(y) = \int_{x_1}^{x_2} f\left(y(x), \frac{dy(x)}{dx}, x\right) dx, \tag{1.21}$$

then the Euler equation is [73]

$$\frac{\partial f}{\partial y} - \frac{d}{dx}\left(\frac{\partial f}{\partial y_x}\right) = 0. \tag{1.22}$$

It is necessary to reformat the governing equations into their equivalent Lagrangian formulation in order to use this calculus of variations. Let L be the Lagrangian of the system. Then, the averaged Lagrangian $\mathcal{L}$ is given by

$$\mathcal{L} = \int L dx. \tag{1.23}$$

The variational method is based on the principle of stationary action. The action is a functional that takes the trajectory of the system as its argument, and its integrand is the averaged Lagrangian, which can be written as

$$S = \int_{z_0}^{z_f} \mathcal{L} dz, \tag{1.24}$$

where S denotes the action and z_0 and z_f denote the initial and final z points. According to the principle of stationary action, the action must be stationary,

$$\delta S = \delta \int_{z_0}^{z_f} \mathcal{L} dz = 0. \tag{1.25}$$

The next step is introducing an appropriate trial function into the averaged Lagrangian if it follows the principle of stationary action. After that, the Lagrangian is averaged by integrating the spatial variables x and y. As a result, the averaged Lagrangian is only dependent on the propagation distance z. The averaged Lagrangian gives a set of variational equations for each of the parameters $q_i(z)$. These variational equations which take the form of Euler-Lagrange's equation are known as modulation equations [74],

$$\frac{\partial \mathcal{L}}{\partial q_i} - \frac{d}{dz}\left(\frac{\partial \mathcal{L}}{\partial \, q_i'}\right) = 0. \tag{1.26}$$

Equation (1.26) yields a system of first-order coupled ordinary differential equations (ODEs). Simple numerical methods such as the standard fourth-order Rune-Kutta method can be used to solve these system of ODEs.

1.6.2 Numerical Methods

Various numerical methods are employed to study the system in different contexts. The numerical methods include the Runge-Kutta method, finite difference method, and pseudo-spectral methods.

Runge-Kutta Method

This method is for numerically solving differential equations and is reasonably simple and robust [75]. Consider an initial value problem,

$$\frac{dy}{dx} = f(x, y), \quad y(x_0) = y_0. \tag{1.27}$$

Here, y is an unknown function of x that we want to approximate. Runge-Kutta method helps in determining an approximate value of y for a given x by calculating four different slopes and using them as weighted averages. Now we choose a step-size h greater than zero and define,

$$y_{n+1} = y_n + \tfrac{1}{6}\left(k_1 + 2k_2 + 2k_3 + k_4\right), \qquad x_{n+1} = x_n + h, \tag{1.28}$$

where,

$$k_1 = hf\left(x_n, y_n\right), \tag{1.29}$$

$$k_2 = hf\left(x_n + \frac{1}{2}h, y_n + \frac{1}{2}k_1\right), \tag{1.30}$$

$$k_3 = hf\left(x_n + \frac{1}{2}h, y_n + \frac{1}{2}k_2\right), \tag{1.31}$$

$$k_4 = hf\left(x_n + h, y_n + k_3\right), \tag{1.32}$$

where, y_{n+1} is the fourth-order Runge Kutta approximation of $y(x_n + 1)$. y_{n+1} is determined by the present value y plus the weighted average of four increments.

Each increment is the product of the interval size h and an estimated slope specified by the function f on the right-hand side of the differential equation.

In Equation (1.28) the sum $(k_1 + 2k_2 + 2k_3 + k_4)/6$ can be considered as an average slope. This method solves the modulation ODE system with fourth-order accuracy in h.

Finite Difference Method

Another numerical method applied in this thesis is the finite-difference method. Several authors have studied and compared the finite difference method to other numerical techniques, concluding that it is efficient and produces accurate solutions at a low computational cost [76–78].

The finite difference techniques are based on approximations that allow differential equations to be replaced by finite difference equations. Finite difference approximation refers to any approximation of a derivative to values at a discrete set of points. The approximations obtained from Taylor expansion nearest to the point of interest are used to replace the partial differential equations in this method. By imposing a rectangular grid on the problem, the dynamical equation is discretized. Consider a function f and its derivative, both of which are finite, single-valued, and continuous functions of x. According to the Taylor series expansion,

$$f(x+h) = f(x) + hf'(x) + \frac{1}{2!}h^2 f''(x) + \frac{1}{3!}h^3 f'''(x) + ..., \tag{1.33}$$

and

$$f(x-h) = f(x) - hf'(x) + \frac{1}{2!}h^2 f''(x) - \frac{1}{3!}h^3 f'''(x) + ..., \tag{1.34}$$

where the superscript $'$ represents the derivative with respect to x. Adding Equations (1.33) and (1.34) yields

$$f(x+h) + f(x-h) = 2f(x) + h^2 f''(x) + O(h^4), \tag{1.35}$$

where $O(h^4)$ denotes the error introduced by truncating the series. Assuming that these terms are insignificant, we can obtain

$$f''(x) = \frac{f(x+h) - 2f(x) + f(x-h)}{h^2}. \tag{1.36}$$

Subtraction of Equation (1.34) from Equation (1.33) while ignoring terms of the order h^3 yields

$$f'(x) = \frac{f(x+h) - f(x-h)}{2h}. \tag{1.37}$$

By including more terms in the Taylor series expansion, higher-order finite difference approximations can be obtained. If f is a function of x and z, then a rectangular grid is imposed on the (x, z) plane so that $x = jh$ and $z = nk$ where j and n are integers. Derivatives can be written as follows:

$$(\frac{\partial^2 f}{\partial x^2})_{j,n} = \frac{1}{h^2}(f^n_{j+1} - 2f^n_j + f^n_{j-1}), \qquad \frac{\partial f}{\partial z} = \frac{1}{k}(f^{n+1}_j - f^n_j), \tag{1.38}$$

where the forward difference approximation is used for $\frac{\partial f}{\partial z}$.

Crank-Nicolson Implicit Method

In this method, the forward difference approximation is used for $\frac{\partial f}{\partial z}$ and the central difference approximation for $\frac{\partial^2 f}{\partial x^2}$.

$$\left(\frac{\partial^2 f}{\partial x^2}\right)_{j,n} = \frac{1}{2}\left(\frac{f^{n+1}_{j+1} - 2f^{n+1}_j + f^{n+1}_{j-1}}{h^2} + \frac{f^n_{j+1} - 2f^n_j + f^n_{j-1}}{h^2}\right). \tag{1.39}$$

Consider the NLSE in the following form that outlines the method,

$$i\frac{\partial f}{\partial z} = \frac{\partial^2 f}{\partial x^2} + |f|^2 f. \tag{1.40}$$

A one-dimensional beam travels through the nonlinear medium. The output field at $z = L$ is calculated from its initial value at $z = 0$. The medium is divided into evenly spaced intervals by k along the propagation direction. The finite difference form of the NLSE is written as:

$$\frac{i}{k}(f_j^{n+1} - f_j^n) = \frac{1}{2}\left(\frac{f_{j+1}^{n+1} - 2f_j^{n+1} + f_{j-1}^{n+1}}{h^2} + \frac{f_{j+1}^n - 2f_j^n + f_{j-1}^n}{h^2}\right) + \\ \frac{1}{2}(|f_j^{n+1}|^2 f_j^{n+1} + |f_j^n|^2 f_j^n). \tag{1.41}$$

Rearranging the equation

$$C_j f_{j+1}^{n+1} + B_j f_j^{n+1} + A_j f_{j-1}^{n+1} = -C_j f_{j+1}^n + B_j f_j^n - A_j f_{j-1}^n, \tag{1.42}$$

where $A_j = -\frac{k}{2h^2} = C_j$, $B_j = i + \frac{k}{2h^2} - \frac{k}{2}|f_j|^{n+1}$, and $D_j = i - \frac{k}{2h^2} + \frac{k}{2}|f_j|^n$. The equation is of the form $AF = D$, where A is a tridiagonal matrix expressed as:

$$\begin{pmatrix} B_1 & C_1 & 0 & 0 & 0 & . & . & . \\ A_1 & B_2 & C_2 & 0 & 0 & . & . & . \\ 0 & A_2 & B_3 & C_3 & 0 & . & . & . \\ 0 & 0 & A_3 & B_4 & C_4 & . & . & . \\ . & . & . & & & & & \\ & & & & & A_{n-2} & B_{n-1} & C_{n-1} \\ . & . & . & & & & A_{n-1} & B_n \end{pmatrix} \begin{pmatrix} f_1^{n+1} \\ f_2^{n+1} \\ f_3^{n+1} \\ . \\ . \\ . \\ f_n^{n+1} \end{pmatrix} = \begin{pmatrix} d_1^n \\ d_2^n \\ d_3^n \\ . \\ . \\ . \\ d_n^n \end{pmatrix}, \tag{1.43}$$

where d_i^j are known variables. This matrix is in the form AF = D and hence the output field F will be obtained as follows:

$$F = A^{-1}D. \tag{1.44}$$

Spectral Methods

Spectral methods are numerical techniques for solving differential equations by representing the solution as a series expansion in orthogonal basis functions such as Fourier series or Chebyshev polynomials. These methods are highly effective for problems with smooth solutions because they offer high accuracy while using fewer grid points. Spectral methods can be applied in physical space, such as using Chebyshev polynomials for one-dimensional problems, or in Fourier space for periodic problems. They rely on the rapid convergence of the series expansion to produce precise results [79, 80].

Pseudo-Spectral Methods

In the pseudo-spectral method, partial differential equations are solved pointwise in the physical space (x, t) similar to finite difference methods. However, the spatial derivatives are computed using orthogonal functions. To explain the approach, consider a differential equation of the form:

$$Lf = g, \tag{1.45}$$

where $f(x, t)$ is the solution, $g(x, t)$ is a source term, and L represents a differential operator. The boundary conditions at $x = \pm 1$ depend on L. The solution is approximated using a finite series expansion:

$$f(x, t) \approx f_n(x, t) = \sum_{k=1}^{n} w_k(t)\phi_k(x), \tag{1.46}$$

where $\phi_k(x)$ are basis functions, and $w_k(t)$ are the expansion coefficients. Basis functions are typically chosen from orthogonal function sets, such as Fourier series or Chebyshev polynomials. The coefficients are determined using a residual function, defined as:

$$R[f_n(x, t)] := [Lf_n - g](x, t). \tag{1.47}$$

The residual function R is calculated using the approximate solution $f_n(x, t)$. The residual norm, $\|R\|$, measures the accuracy of the approximation, and the goal is to minimize R over the domain. The expansion coefficients w_k are chosen to satisfy boundary conditions, while the remaining coefficients are adjusted to make R as small as possible at several spatial points.

The pseudo-spectral method provides exact solutions at collocation points, with interpolation used to determine the solution between these points. Chebyshev polynomials are commonly employed for interpolation, and the collocation points are defined as $x_j = \cos\left(\frac{j\pi}{N}\right)$, where $j = 0, 1, 2, \ldots, N$. This method is highly effective for smooth functions and exhibits geometric convergence.

1.7 Objectives of this Thesis

- Investigate the propagation of nematicons under the influence of damping and diffractive radiation.
- Study the impact of thermal effects on nematicon propagation.
- Explore the behavior of nematicons within a parabolic potential.
- Study the thermal response of nematicons within a parabolic potential.
- Analyze the propagation dynamics of nematicons in a periodic potential.
- Investigate the effect of thermal response and diffractive radiation on nematicon dynamics in a periodic potential.

1.8 Relevance of this Study

The thesis titled “Studies on Nonlinear Beam Dynamics in Uniaxial Nematic Liquid Crystals Under the Influence of Temperature, Diffractive Radiation, and Potentials” holds significant relevance in both scientific research and technological applications.

Advancement in Optical Communications: Understanding the nonlinear beam dynamics in uniaxial nematic liquid crystals under the influence of parabolic and periodic potentials, thermal responses, and diffractive radiation is crucial for improving the design and performance of optical devices such as switches, modulators, and waveguides.

Nonlinear Optics: Nonlinear optical phenomena are critical in developing advanced materials for photonics. This research contributes to the broader understanding of how nematic liquid crystals as a nonlinear medium interact with light which can lead to innovations in light manipulation and laser technologies.

Tunable Photonic Devices: Nematic liquid crystals due to their sensitivity to temperature and light intensity offer tunability for photonic devices. By exploring the thermal influences on nematicon propagation, this research can contribute to the development of adaptive optical components such as reconfigurable waveguides, optical switches, and modulators.

Energy-efficient Technologies: Understanding the thermal effects on nematic liquid crystals could contribute to the development of energy-efficient technologies as these materials are widely used in low power consuming displays and other optoelectronic devices.

In summary, this research has practical implications for improving photonic devices, advancing optical communication systems, and contributing to the broader field of nonlinear optics.

1.9 Motivation of this Study

The motivation behind the thesis titled “Studies on Nonlinear Beam Dynamics in Uniaxial Nematic Liquid Crystals Under the Influence of Temperature, Diffractive Radiation, and Potentials” is rooted in the need to deepen our understanding of the complex interactions between light and nematic liquid crystals. Nematic liquid crystals like E7 are widely known for their significant electro-optic properties which make them essential in a variety of photonic applications such as displays, waveguides, and optical communication systems. However, the nonlinear optical behavior of beams propagating through such media is governed by complex interactions between the material’s refractive index profile, molecular alignment, and nonlinear response necessitating further investigation to fully understand and optimize these effects.

One of the major challenges in utilizing NLC for practical applications is understanding how thermal effects such as temperature variations alter the molecular alignment and consequently, the optical properties of the material. This is particularly important because temperature changes can induce fluctuations in the refractive index leading to beam distortion, diffraction, or self-focusing effects. In real-world optical systems, thermal effects often coexist with other nonthermal factors such as external electric fields or light-induced molecular reorientation. These effects can significantly impact the behavior of optical beams propagating through NLCs making it crucial to model and predict how such variables interact.

A theoretical study offers the advantage of providing a controlled environment where these complex phenomena can be modeled and simulated. By focusing on the propagation of nonlinear optical beams in E7, a widely used uniaxial nematic liquid crystal, this thesis aims to explore how various factors affect the optical response. The study will help clarify how these factors contribute to phenomena like optical self-trapping, beam deflection, and soliton formation which are key to optimizing the performance of NLC based photonic devices.

Additionally, there is a growing interest in applying NLC in more advanced photonic systems such as reconfigurable optical circuits and all-optical switching devices. These systems often operate in environments where thermal management is critical making it even more important to understand how temperature and other parameters affect optical beam propagation in NLCs. This research is expected to provide insights that will aid in the development of more efficient and robust liquid crystal based optical technologies.

In summary, the motivation for this thesis is driven by the need to enhance the theoretical understanding of nonlinear beam dynamics in uniaxial nematic liquid crystals particularly under the influence of potential, thermal response, and diffractive radiation effects with a focus on the E7 NLC. Such insights will contribute to the development of more precise and reliable optical systems utilizing

NLC in various technological applications.

1.10 Outline of Thesis

The thesis presents studies on nonlinear beam dynamics in uniaxial nematic liquid crystals under the influence of temperature, diffractive radiation, and potentials. A coupled system consisting of (2+1)D nonlinear Schrodinger-type equations for the optical beam and elliptic Poisson equations for the molecular director governs the propagation of nonlinear optical beams in NLCs. The variational and numerical methods are employed for the analysis. The standard fourth-order Runge Kutta method is employed to solve the modulation equations numerically. The finite difference beam propagation method has been used to solve the full governing equation of beam evolution in uniaxial NLC. For linear stability analysis, the pseudo-spectral method is employed. The remaining chapters of the thesis are structured as follows.

Chapter 2 discusses the interplay between diffractive radiation shed and damping coefficient in a NLC with nonlocal nonlinearity. Semi-analytical and numerical techniques are used to analyze the system. The introduction of defects into the NLC causes some kind of damping of nematicons. These defects can be induced at the time of construction of the NLC. We investigate the propagation of a beam through a medium in three situations in which defects in NLC are made in such a way that three different types of damping are produced. Even when the medium exhibits some kind of damping, we found that the diffractive radiation aids the beam to evolve as a nematicon. In the case of constant and periodic damping, the damping effect is canceled by high diffractive radiation. However, only a very small value of diffractive radiation shelf height can overcome the hyperbolic damping, allowing the nematicon to travel through the medium.

The thermal responses of single-peak and double-peak solitons in a nematic liquid crystal have been numerically studied in Chapter 3. Single-peak nematicons are observed for low thermal response coefficients where the behavior is primarily influenced by focusing reorientational nonlinearity. As the thermal response coefficients increase, the defocusing thermal nonlinearity becomes dominant, causing the beam to broaden and eventually split into double-peak nematicons. This competition between focusing reorientational and defocusing thermal nonlinearities leads to the formation of single-peak and double-peak nematicons. The stability of the stationary solutions to small perturbations is analyzed using the Bogoliubov-de Gennes equations. Single-peak nematicons are stable regardless of thermal response coefficient values while double-peak nematicons remain stable only for large values of thermal response coefficients. Moreover, higher thermal response coefficients reduce the total nonlinear response of the medium making the beam more resistant to perturbations.

Chapter 4 studies the behavior of nonlocal spatial optical solitons in a uniaxial nematic liquid crystal with a parabolic potential. By doping NLC with an appropriate dopant such as dye, carbon nanotubes (CNTs), or nanoparticles, the parabolic potential can be generated experimentally [81–83]. Numerical and semi-analytic methods are used to solve the equations governing the system. We found that nematicons exist in the parabolic potential. These nematicons show periodic oscillations in the presence of a parabolic potential. It has been found that when potential strength increases, the wavelength of periodic oscillations decreases linearly. Higher harmonics of nematicons can be produced by varying the strength of the parabolic potential. The nematicons are found to be stable in a parabolic potential according to the linear stability analysis.

Chapter 5 focuses on the impact of thermal response on nematicons in a parabolic potential. Single-peak nematicons can be observed only when thermal response coefficients are absent, as focusing reorientational nonlinearity dominates under such conditions. However, when the thermal response is introduced, the interplay between the focusing reorientational and defocusing thermal nonlinearities can lead to the transformation of single-peak nematicons into double-peak structures. In this scenario, the defocusing thermal nonlinearity exceeds the focusing reorientational nonlinearity resulting in the formation of double-peak nematicons. The combined effect of these nonlinearities reshapes the energy landscape encountered by the light beam within the medium. This altered energy distribution characterized by multiple maxima, allows for the stabilization of double-peak nematicons as equilibrium configurations. In the presence of a parabolic potential, nematicons can exhibit periodic oscillations. For small thermal response coefficients, double-peak nematicons with periodic oscillations can be obtained. The thermal response coefficients significantly influence the oscillation wavelength of these nematicons with the wavelength increasing as the coefficients grow. At high thermal response coefficients, the double-peak nematicons lose their oscillatory nature. Linear stability analysis indicates that single-peak nematicons and double-peak nematicons with periodic oscillations can be stable whereas double-peak nematicons without oscillations tend to be unstable.

Chapter 6 explores the formation and stability of single-peak and multi-peak gap nematicons by employing numerical analysis. The study includes both stationary and dynamic solutions within the first band gap. Both single-peak and multi-peak gap nematicons can be observed within this gap. Single-peak gap nematicons are found across a broad range of propagation constants whereas multi-peak gap nematicons emerge only when the propagation constant exceeds a certain threshold. The intensity distribution across the peaks in a multi-peak gap nematicon is strongly influenced by the intensity of the input beam. The stability of stationary solutions against small perturbations is analyzed using the Bogoliubov–de Gennes equations. Single-peak gap nematicons are stable. Multi-peak gap nematicons are stable when the peaks have equal amplitudes but become unstable when the peak amplitudes are unequal.

Chapter 7 deals with the effect of thermal response and diffractive radiation on the behavior of multi-peak gap nematicons employing numerical simulations for the analysis. Both stationary and dynamic solutions are studied revealing that the thermal response by itself results in the formation of two-peak gap nematicons within the first band gap. The separation between peaks increases in a nonlinear parabolic pattern as the thermal response coefficients rise driven by the interaction between thermal effects and refractive index variations in the NLC. The inclusion of diffractive radiation leads to the formation of three-peak and four-peak gap nematicons where energy dynamically redistributes among the peaks depending on the diffractive radiation shelf heights. The stability of these multi-peak configurations under small perturbations is evaluated using the Bogoliubov–de Gennes equations. Linear stability analysis shows that two-peak gap nematicons with thermal response can be stable. Three-peak gap nematicons exhibit stability for comparatively large diffractive radiation shelf heights with energy distributed almost uniformly among the peaks. However, at higher thermal response values even symmetrically distributed peaks in a four-peak gap nematicon become unstable. This instability is driven by stronger thermal gradients which amplify refractive index modulations disrupting the confinement of the peaks. These intensified modulations cause the peaks to shift out of phase ultimately leading to instability regardless of their peak symmetry.

Chapter 8 summarizes the results and conclusions of the thesis. This chapter also includes recommendations for future research in NLC and other optical media.

Bibliography

[1] Khoo IC. Nonlinear optics of liquid crystalline materials. Physics Reports. 2009 Feb;471(5–6):221-67.

[2] Lam L. Solitons in liquid crystals: Recent developments. Chaos, Solitons &amp Fractals. 1995 dec;5(12):2463-73.

[3] Lam L. Solitons in Liquid Crystals. Springer New York; 1992.

[4] Lei L, Changqing S, Juelian S, Lam PM, Yun H. Soliton Propagation in Liquid Crystals. Physical Review Letters. 1982 nov;49(18):1335-8.

[5] Kartashov YV, Malomed BA, Torner L. Solitons in nonlinear lattices. Reviews of Modern Physics. 2011 apr;83(1):247-305.

[6] Chen HH, Liu CS. Solitons in Nonuniform Media. Physical Review Letters. 1976 sep;37(11):693-7.

[7] Haus HA, Wong WS. Solitons in optical communications. Reviews of Modern Physics. 1996 apr;68(2):423-44.

[8] Andrienko D. Introduction to liquid crystals. Journal of Molecular Liquids. 2018 oct;267:520-41.

[9] Lagerwall JPF, Giesselmann F. Current Topics in Smectic Liquid Crystal Research. ChemPhysChem. 2006 jan;7(1):20-45.

[10] Lebwohl PA, Lasher G. Nematic-Liquid-Crystal Order—A Monte Carlo Calculation. Physical Review A. 1972 jul;6(1):426-9.

[11] Assanto G, Minzoni AA, Smyth NF, Worthy AL. Refraction of nonlinear beams by localized refractive index changes in nematic liquid crystals. Physical Review A. 2010 nov;82(5):053843.

[12] Assanto G, Smyth NF. Self-confined light waves in nematic liquid crystals. Physica D: Nonlinear Phenomena. 2020 jan;402:132182.

[13] Scalia G. Alignment of Carbon Nanotubes in Thermotropic and Lyotropic Liquid Crystals. ChemPhysChem. 2010 jan;11(2):333-40.

[14] Lagerwall JPF, Scalia G. A new era for liquid crystal research: Applications of liquid crystals in soft matter nano-, bio- and microtechnology. Current Applied Physics. 2012 nov;12(6):1387-412.

[15] Coates D. Development and applications of cholesteric liquid crystals. Liquid Crystals. 2015 jun:1-13.

[16] Kelly SM, O'Neill M. Liquid crystals for electro-optic applications. In: Handbook of Advanced Electronic and Photonic Materials and Devices. Elsevier; 2001. p. 1-66.

[17] GEELHAAR T. Liquid crystals for display applications. Liquid Crystals. 1998 jan;24(1):91-8.

[18] Zhou L, Liu S. Development and Prospect of Viewing Angle Switchable Liquid Crystal Devices. Crystals. 2022 Sep;12(10):1347.

[19] Assanto G, Peccianti M, Conti C. Nematicons: Optical Spatial Solitons in Nematic Liquid Crystals. Optics and Photonics News. 2003 feb;14(2):44.

[20] Garcìa CV, Garcilópez IP, Lallana PC, Vinouze B, Fracasso B. Liquid crystal optical switches. In: Optical Switches. Elsevier; 2010. p. 206-40.

[21] Ikeda T, Tsutsumi O, Sasaki T. Liquid crystal photonics: optical switching and image storage by means of nematic liquid crystals and ferroelectric liquid crystals. Synthetic Metals. 1996 aug;81(2-3):289-96.

[22] Wang Z, Xu T, Noel A, Chen YC, Liu T. Applications of liquid crystals in biosensing. Soft Matter. 2021;17(18):4675-702.

[23] Budaszewski D, Chychłowski M, Budaszewska A, Bartosewicz B, Jankiewicz B, Woliński TR. Enhanced efficiency of electric field tunability in photonic liquid crystal fibers doped with gold nanoparticles. Optics Express. 2019 May;27(10):14260.

[24] Assanto G. Nematicons: reorientational solitons from optics to photonics. Liquid Crystals Reviews. 2018 Jul;6(2):170-94.

[25] Assanto G, Karpierz MA. Nematicons: self-localised beams in nematic liquid crystals. Liquid Crystals. 2009 oct;36(10-11):1161-72.

[26] Piccardi A, Alberucci A, Assanto G. Nematicons and Their Electro-Optic Control: Light Localization and Signal Readdressing via Reorientation in Liquid Crystals. International Journal of Molecular Sciences. 2013 oct;14(10):19932-50.

[27] Duran S, Karabulut B. Nematicons in liquid crystals with Kerr Law by sub-equation method. Alexandria Engineering Journal. 2022 feb;61(2):1695-700.

[28] Ramaswamy R, Kader AHA, Elsonbaty A. New Exact Nematicon Solutions of Liquid Crystal Model With Different Types of Nonlinearities. IEEE Access. 2021;9:107909-16.

[29] Assanto G. Nematicons. John Wiley Sons Inc.; 2012.

[30] Meng Z, Yang Y, Wan Y. Controllable random lasers based on two-dimensional random gain systems with nematic liquid crystals. Indian Journal of Physics. 2021 apr;96(6):1805-12.

[31] Ye L, Zhao C, Feng Y, Gu B, Cui Y, Lu Y. Study on the Polarization of Random Lasers from Dye-Doped Nematic Liquid Crystals. Nanoscale Research Letters. 2017 Jan;12(1):Article ID 27.

[32] Bedjaoui L, Gogibus N, Ewen B, Pakula T, Coqueret X, Benmouna M, et al. Preferential solvation of the eutectic mixture of liquid crystals E7 in a polysiloxane. Polymer. 2004 sep;45(19):6555-60.

[33] Laudyn UA, Piccardi A, Kwasny M, Karpierz MA, Assanto G. Thermo-optic soliton routing in nematic liquid crystals. Optics Letters. 2018 may;43(10):2296.

[34] Rusen E, Diacon A, Mitran RA, Dinescu A, Nistor C, Șomoghi R, et al. E7 nematic liquid crystal encapsulated in a polymeric photonic crystal. European Polymer Journal. 2022 Jul;175:111374.

[35] Okutan M, Yeşilot G, Bolivar PH. Contribution of Multiwalled carbon nanotubes to dielectric and elastic properties in E7 nematic liquid crystal. Journal of Molecular Liquids. 2022 dec;368:120662.

[36] Duran H, Gazdecki B, Yamashita A, Kyu T. Effect of carbon nanotubes on phase transitions of nematic liquid crystals. Liquid Crystals. 2005 Jul;32(7):815-21.

[37] Yang CS, Lin CJ, Pan RP, Que CT, Yamamoto K, Tani M, et al. The complex refractive indices of the liquid crystal mixture E7 in the terahertz frequency range. Journal of the Optical Society of America B. 2010 Aug;27(9):1866.

[38] Singh BP, Sikarwar S, Pandey KK, Manohar R, Depriester M, Singh DP. Carbon Nanotubes Blended Nematic Liquid Crystal for Display and Electro-Optical Applications. Electronic Materials. 2021 Oct;2(4):466-81.

[39] Derouiche Y, Dubois F, Douali R, Legrand C, Maschke U. Some Properties of Nematic Liquid Crystal E7/Acrylic Polymer Networks. Molecular Crystals and Liquid Crystals. 2011 Jun;541(1):201/[439]-210/[448].

[40] Joshi AA, Whitmer JK, Guzmán O, Abbott NL, de Pablo JJ. Measuring liquid crystal elastic constants with free energy perturbations. Soft Matter. 2014;10(6):882-93.

[41] Salamon P, Éber N, Seltmann J, Lehmann M, Gleeson JT, Sprunt S, et al. Dielectric technique to measure the twist elastic constant of liquid crystals: The case of a bent-core material. Physical Review E. 2012 Jun;85(6):061704.

[42] Yakuphanoglu F, Okutan M, Koysal O, Ahn SM, Keum SR. Dielectric anisotropy, and diffraction efficiency properties of a doped nematic liquid crystal. Dyes and Pigments. 2008 Jan;76(3):721-5.

[43] Mhatre MM, Katariya-Jain A, Deshmukh RR. Enhancing morphological, electro-optical and dielectric properties of polymer-dispersed liquid crystal by doping of disperse Orange 25 dye in LC E7. Liquid Crystals. 2021 dec;49(6):790-803.

[44] Ganea CP, Manaila-Maximean D, Cîrcu V. Dielectric investigations on carbon nanotubes doped polymer dispersed liquid crystal films. The European Physical Journal Plus. 2020 oct;135(10).

[45] Eskalen H, Okumuş M, Özgan Electro-optical, thermal and dielectric properties of ternary mixture of E7/6CB/6BA liquid crystal mixture complex. Optik. 2019 Jun;187:223-9.

[46] Peccianti M, Conti C, Assanto G, De Luca A, Umeton C. Routing of anisotropic spatial solitons and modulational instability in liquid crystals. Nature. 2004 Dec;432(7018):733-7.

[47] Conti C, Peccianti M, Assanto G. Observation of Optical Spatial Solitons in a Highly Nonlocal Medium. Physical Review Letters. 2004 Mar;92(11):113902.

[48] Alberucci A, Piccardi A, Peccianti M, Kaczmarek M, Assanto G. Propagation of spatial optical solitons in a dielectric with adjustable nonlinearity. Physical Review A. 2010 Aug;82(2):023806.

[49] Alberucci A, Assanto G, MacNeil JML, Smyth NF. Nematic liquid crystals: An excellent playground for nonlocal nonlinear light localization

in soft matter. Journal of Nonlinear Optical Physics amp; Materials. 2014 Dec;23(04):1450046.

[50] Warenghem M, Blach JF, Henninot JF. Thermo-nematicon: an unnatural coexistence of solitons in liquid crystals? Journal of the Optical Society of America B. 2008 oct;25(11):1882.

[51] Buccoliero D, Desyatnikov AS, Krolikowski W, Kivshar YS. Boundary effects on the dynamics of higher-order optical spatial solitons in nonlocal thermal media. Journal of Optics A: Pure and Applied Optics. 2009 aug;11(9):094014.

[52] Alberucci A, Laudyn UA, Piccardi A, Kwasny M, Klus B, Karpierz MA, et al. Nonlinear continuous-wave optical propagation in nematic liquid crystals: Interplay between reorientational and thermal effects. Physical Review E. 2017 Jul;96(1):012703.

[53] Assanto G, Khan C, Smyth NF. Multihump thermo-reorientational solitary waves in nematic liquid crystals: Modulation theory solutions. Physical Review A. 2021 jul;104(1):013526.

[54] Ramaniuk A, Jung PS, Christodoulides DN, Krolikowski W, Trippenbach M. Absorption-mediated stabilization of nonlinear propagation of vortex beams in nematic liquid crystals. Optics Communications. 2019 nov;451:338-44.

[55] Cyprych K, Jung PS, Izdebskaya Y, Shvedov V, Christodoulides DN, Krolikowski W. Anomalous interaction of spatial solitons in nematic liquid crystals. Optics Letters. 2019 jan;44(2):267.

[56] Jisha CP, Beeckman J, Acker FV, Neyts K, Nolte S, Alberucci A. Generation of multiple solitons using competing nonlocal nonlinearities. Optics Letters. 2019 feb;44(5):1162.

[57] Nari Mangalath S, Tharammel Puthenpeedikakkal S. The formation and stability of single-peak and multi-peak gap nematicons in a periodic potential. Liquid Crystals. 2024 Sep:1-13.

[58] Lee S, Ho ST. Optical switching scheme based on the transmission of coupled gap solitons in nonlinear periodic dielectric media. Optics Letters. 1993 jun;18(12):962.

[59] Kartashov YV, Vysloukh VA, Torner L. Surface Gap Solitons. Physical Review Letters. 2006 feb;96(7):073901.

[60] Sipe JE. In: Gap Solitons. Springer Netherlands; 1992. p. 305-18.

[61] Shi Z, Wang J, Chen Z, Yang J. Linear instability of two-dimensional low-amplitude gap solitons near band edges in periodic media. Physical Review A. 2008 Dec;78(6):063812.

[62] Bao YY, Li SR, Liu YH, Xu TF. Gap solitons and nonlinear Bloch waves in fractional quantum coupler with periodic potential. Chaos, Solitons &amp Fractals. 2022 Mar;156:111853.

[63] Assanto G, Khan C, Piccardi A, Smyth NF. Temperature control of nematicon trajectories. Physical Review E. 2019 dec;100(6):062702.

[64] Assanto G, Peccianti M, Brzdakiewicz KA, de Luca A, Umeton C. Nonlinear Wave Propagation and Spatial Solitons in Nematic Liquid Crystals. Journal of Nonlinear Optical Physics &amp Materials. 2003 jun;12(02):123-34.

[65] Karpierz MA. Solitary waves in liquid crystalline waveguides. Physical Review E. 2002 sep;66(3):036603.

[66] Kwasny M, Laudyn UA, Sala FA, Alberucci A, Karpierz MA, Assanto G. Self-guided beams in low-birefringence nematic liquid crystals. Physical Review A. 2012 jul;86(1):013824.

[67] Assanto G, Smyth NF. Spin-optical solitons in liquid crystals. Physical Review A. 2020 sep;102(3):033501.

[68] Assanto G, Peccianti M. Spatial solitons in nematic liquid crystals. IEEE Journal of Quantum Electronics. 2003 jan;39(1):13-21.

[69] Venkata Sai D, Mirri G, Kouwer PHJ, Sahoo R, Musevic I, Dhara S. Unusual temperature dependence of elastic constants of an ambient-temperature discotic nematic liquid crystal. Soft Matter. 2016;12(11):2960-4.

[70] Sai DV, Yoon TH, Dhara S. Studies on binary mixtures of nematic liquid crystals made of strongly polar molecules with identical cores and antagonistic orientation of permanent dipoles. Journal of Molecular Liquids. 2020 Aug;312:113410.

[71] Anderson D. Variational approach to nonlinear pulse propagation in optical fibers. Physical Review A. 1983 jun;27(6):3135-45.

[72] Cooper F, Lucheroni C, Shepard H, Sodano P. Variational method for studying solitons in the Korteweg-de Vries equation. Physics Letters A. 1993 jan;173(1):33-6.

[73] Syafwan M, Susanto H, Cox SM, Malomed BA. Variational approximations for traveling solitons in a discrete nonlinear Schrödinger equation. Journal of Physics A: Mathematical and Theoretical. 2012 Feb;45(7):075207.

[74] Dhaouadi F, Favrie N, Gavrilyuk S. Extended Lagrangian approach for the defocusing nonlinear Schrödinger equation. Studies in Applied Mathematics. 2018 oct;142(3):336-58.

[75] Zingg DW, Chisholm TT. Runge–Kutta methods for linear ordinary differential equations. Applied Numerical Mathematics. 1999 oct;31(2):227-38.

[76] Joseph RM, Taflove A. FDTD Maxwell's equations models for nonlinear electrodynamics and optics. IEEE Transactions on Antennas and Propagation. 1997 mar;45(3):364-74.

[77] Wilson JP. Generalized Finite-Difference Time-Domain method with absorbing boundary conditions for solving the nonlinear Schrödinger equation on a GPU. Computer Physics Communications. 2019 feb;235:279-92.

[78] Moxley FI, Chuss DT, Dai W. A generalized finite-difference time-domain scheme for solving nonlinear Schrödinger equations. Computer Physics Communications. 2013 aug;184(8):1834-41.

[79] Fahroo F, Ross IM. Advances in Pseudospectral Methods for Optimal Control. In: AIAA Guidance, Navigation and Control Conference and Exhibit. American Institute of Aeronautics and Astronautics; 2008. .

[80] Fornberg B, Sloan DM. A review of pseudospectral methods for solving partial differential equations. Acta Numerica. 1994 Jan;3:203-67.

[81] Smyth NF, Assanto G, Skuse BD. Optical path control of solitary waves in dye-doped nematic liquid crystals. Photonics Letters of Poland. 2009 dec;1(4).

[82] Lin FC, Wu PC, Jian BR, Lee W. Dopant Effect and Cell-Configuration-Dependent Dielectric Properties of Nematic Liquid Crystals. Advances in Condensed Matter Physics. 2013;2013:1-5.

[83] Urbanski M. On the impact of nanoparticle doping on the electro-optic response of nematic hosts. Liquid Crystals Today. 2015 sep;24(4):102-15.

Chapter 2

Impact of Diffractive Radiation Shed on Nematicon Propagation

This chapter discusses the behavior of spatial solitons propagating through nematic liquid crystals under the influence of damping in a nonlocal regime. The role of diffractive radiation in enabling the undisturbed propagation of nematicons is analyzed using both variational analysis and numerical simulations. For a constant damping coefficient, higher levels of diffractive radiation are necessary to offset the damping effects. In the case of periodic damping profiles, even greater diffractive radiation is required to counteract the damping effects compared to constant damping profiles. However, low levels of diffractive radiation are sufficient to balance the effects of hyperbolic damping. The analysis is crucial for ensuring the stable propagation of nematicons under varying damping conditions. By analyzing the impact of diffractive radiation, the study offers valuable insights into optimizing conditions for undisturbed nematicon behavior in practical optical systems.

The results of this chapter are published as:

- N. M. Sajitha, T. P. Suneera, 'Interplay between diffractive radiation shed and damping coefficient on nematicon propagation'. Journal of Modern Optics. 2022 nov; 69(20): 1134–1141.

2.1 Introduction

The study of solitons in liquid crystals represents a significant area within nonlinear physics [1]. Specifically, nematicons are solitary waves observed in nematic liquid crystals (NLCs) that have garnered considerable interest in recent years [2, 3]. Throughout this thesis, we focus on NLCs with a single symmetry axis composed of anisotropic molecules in a fluid state. Typical NLCs exhibit positive uniaxial behavior where the molecular director, a unit vector aligned with the long axis of ellipsoid-shaped molecules, coincides with the optic axis [4]. According to G. Assanto, when a beam travels through a nonlocal NLC, it generates a diffractive radiation shelf beneath it, which can be visualized as circular patterns, enabling the beam to move through the medium without distortion [5].

The chapter focuses on understanding the behavior of nematicons when subjected to damping, a factor that affects their propagation. The research is motivated by the need to investigate how diffractive radiation plays a crucial role in maintaining stable soliton propagation in a nonlocal regime where interactions extend over a range of distances. In this chapter we aim to explore how different types of damping such as constant, periodic, or hyperbolic profiles influence the propagation of these solitons and how diffractive radiation can counterbalance these effects. The research highlights the significance of diffractive radiation in mitigating the effects of damping. The motivation is to enhance understanding of the relationship between damping and soliton behavior offering insights into optimizing conditions for undisturbed soliton travel in systems with complex damping profiles. Such findings are valuable for optical communications and photonic technologies where solitons are used as stable information carriers. Nematicons can be utilized in designing waveguides, optical circuits, or all-optical switching devices. These solitons can navigate in complex media without spreading out, making them ideal for precise signal transmission.

This chapter is arranged as follows. Section 2.2 explains the theoretical model of the beam propagation in a nematic liquid crystal having nonlocal nonlinearity and damping. Section 2.3 gives the results and discussions. First, the beam dynamics have been analyzed in the NLC with a constant damping coefficient. Then the study has been extended to the systems with periodic and hyperbolic damping profiles. Section 2.4 concludes the chapter.

2.2 Theoretical model

Consider an optical beam propagating along the z-direction through the positive uniaxial NLC. The geometry of the nematic liquid crystal cell is the same as that described in Ref. [5] and is shown in Figure (2.1). The optic axis of the nematic is aligned along the y-direction. The angle ξ describes the optic axis reorientation in the xy plane. The beam propagates through the medium and undergoes damping. The system is modeled by a nonlinear Schrodinger-type equation for the optical beam and an elliptic Poisson equation for the molecular director. The governing equations of the system are given by

$$2ik_0n_{\perp}\frac{\partial E_x}{\partial z}+\frac{\partial^2 E_x}{\partial x^2}+\frac{\partial^2 E_x}{\partial y^2}+k_o^2\epsilon_a E_x sin^2\xi+\frac{1}{2}k_0^2\epsilon_a E_y e^{ik_0(n_{\parallel}-n_{\perp})z}sin2\xi \\ +i\epsilon(z)E_x=0, \qquad (2.1)$$

$$2ik_0n_{\parallel}\frac{\partial E_y}{\partial z}+\frac{\partial^2 E_y}{\partial x^2}+\frac{n_{\parallel}^2}{n_{\perp}^2}\frac{\partial^2 E_y}{\partial y^2}-k_o^2\epsilon_a E_y sin^2\xi+\frac{1}{2}k_0^2\epsilon_a E_x e^{-ik_0(n_{\parallel}-n_{\perp})z}sin2\xi \\ +i\epsilon(z)E_y=0, \qquad (2.2)$$

with the equation of the molecular director

$$K\nabla^2\xi+\frac{1}{4}\epsilon_0\epsilon_a\left[2(|E_x|^2-|E_y|^2)sin2\xi+2ReE_xE_y^*e^{-ik_0(n_{\parallel}-n_{\perp})z}cos2\xi\right]=0. \qquad (2.3)$$

E_x and E_y are the x and y components of the electric fields, and ξ is the director angle. The subscripts x and y represent the partial derivatives concerning x and y respectively. z is the propagation distance. k_0 be the ordinary wave vector and ϵ_a be the birefringence of the nematic. K denotes the elastic constant of the

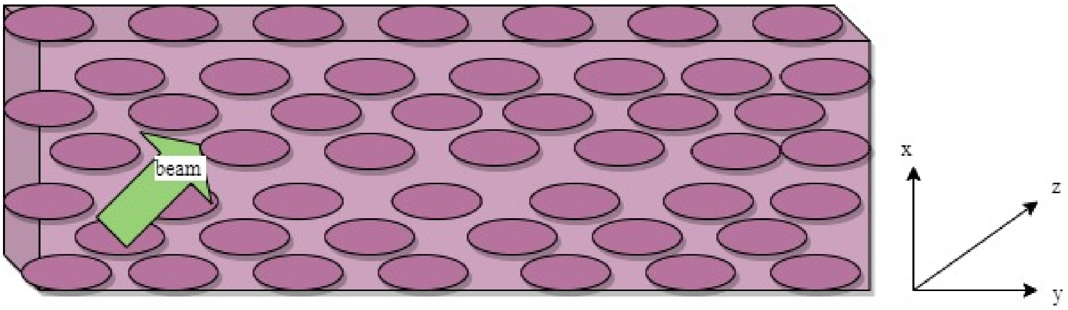

Figure 2.1: The figure of the considered sample and interaction geometry. A nematic liquid crystal with the ellipses represents the elongated NLC molecules. The green arrow represents the input light beam impinges on the sample.

medium. $n_\parallel$ and $n_\perp$ are the refractive indices parallel and perpendicular to the director alignment respectively. $\epsilon(z)$ is the damping coefficient which is a function of the propagation distance z. The various constants in the model are chosen as the material parameters of the standard E7 mixture at room temperature which is a positive uniaxial NLC with $n_\parallel$= 1.73 and $n_\perp$ = 1.53, and elastic constant K= 12pN [5]. $\nabla^2\xi$ is the two-dimensional Laplacian. The equations of x and y components of the electric field of the beam are

$$E_x = Xe^{ik_0 n_\perp z}, \qquad E_y = Ye^{ik_0 n_\parallel z}. \tag{2.4}$$

Here, X and Y are the amplitudes of electric fields in two transverse directions. By substituting Equation (2.4) in Equations (2.1) - (2.3) we get,

$$2i\frac{\partial X}{\partial z} + \frac{\partial^2 X}{\partial x^2} + \frac{\partial^2 X}{\partial y^2} + Xsin^2\xi + \frac{1}{2}Ye^{\frac{iz}{1+\gamma}}sin2\xi + i\epsilon(z)X = 0, \tag{2.5}$$

$$2i\gamma\frac{\partial Y}{\partial z} + \frac{\partial^2 Y}{\partial x^2} + \gamma^2\frac{\partial^2 Y}{\partial y^2} - Ysin^2\xi + \frac{1}{2}Xe^{\frac{-iz}{1+\gamma}}sin2\xi + i\epsilon(z)Y = 0, \tag{2.6}$$

$$\nu\nabla^2\xi + (|X|^2 - |Y|^2)sin2\xi + 2Re(XY^*e^{\frac{-iz}{1+\gamma}})cos2\xi = 0, \tag{2.7}$$

where,

$$\gamma = \frac{n_{\parallel}}{n_{\perp}}, \qquad \nu = \frac{4Kk_0^2}{\epsilon_0 A_b^2}. \tag{2.8}$$

Here, γ and ν are the anisotropy and the nonlocality respectively. A_b is the amplitude of the input optical beam.

The introduction of defects into the NLC causes some kind of damping of nematicons [6]. These defects can be induced at the time of construction of the NLC [7]. Here we analyze the propagation of the beam through the medium in three cases in which defects are created in NLC in such a way as to produce three different types of damping.

1. constant damping
2. periodic damping
3. hyperbolic damping

The Equations (2.5) - (2.7) have been analyzed by employing the variational method. The Lagrangian density of the system is given by

$$\begin{aligned} L = i(X^*X_z - XX_z^*) - |X_x|^2 - |X_y|^2 - i\gamma(Y^*Y_z - YY_z^*) - |Y_x|^2 - \gamma^2|Y_y|^2 \\ -\frac{1}{2}\nu|\nabla\xi|^2 + Re(XY^*e^{\frac{-iz}{1+\gamma}})sin2\xi + (|X|^2 - |Y|^2)sin^2\xi \\ +i\epsilon(z)(|X|^2 + |Y|^2), \end{aligned} \tag{2.9}$$

where the asterisk stands for complex conjugation. The trial solutions are chosen as [5]

$$X = \left(a_x e^{-\frac{r^2}{w_x^2}} + ig_x\right)e^{i\sigma_x}, \quad Y = \left(a_y e^{-\frac{r^2}{w_y^2}} + ig_y\right)e^{i\sigma_y}, \quad \xi = \alpha e^{-\frac{r^2}{\beta^2}}, \tag{2.10}$$

where $r^2 = x^2 + y^2$. a_x and a_y are the amplitudes, w_x and w_y are the widths, and σ_x and σ_y are the phases of the beam in two transverse directions. Also, g_x and g_y are the height of the diffractive radiation in the x and y directions respectively. α and β be the amplitude and width of the director respectively. The parameters a_x, a_y, w_x, w_y, σ_x, σ_y, g_x, g_y, and α are functions of z.

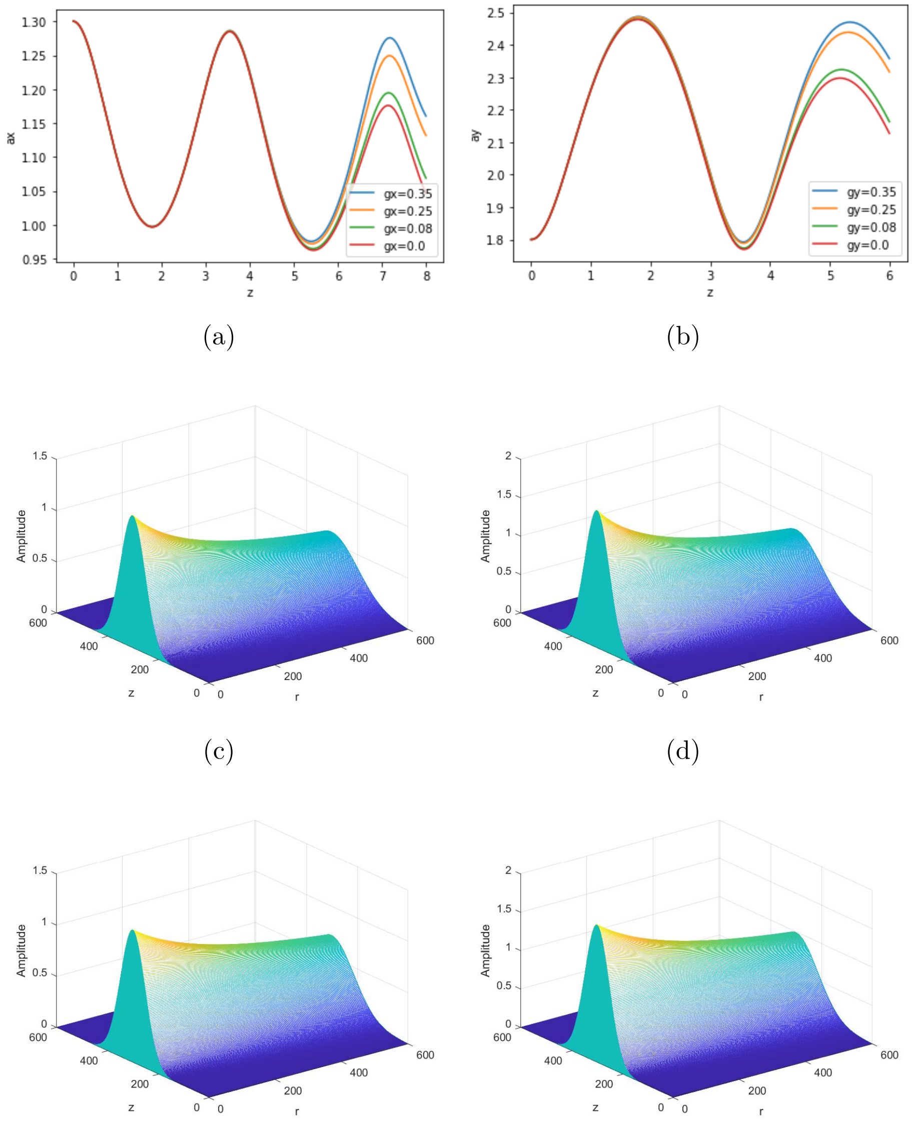

(a) (b)

(c) (d)

(e) (f)

Figure 2.2: Beam propagation with constant damping plotted for damping coefficient $\epsilon_s = 3$ for an initial excitation with a_{x0}=1.3, a_{y0}=1.8, w_{x0}=12, w_{y0}=12, σ_{x0}=0, σ_{y0}=0. In the first row (Results of variational analysis): (a) evolution of amplitude along the x-direction, (b) evolution of amplitude along the y-direction. The second and third-row corresponds to numerical results. In the second row: (c) the evolution of amplitude along the x-direction, (d) evolution of amplitude along the y-direction for g_x=g_y=0; In the third row: (e) the evolution of amplitude along the x-direction, (f) evolution of amplitude along the y-direction for g_x=g_y=0.08.

The trial functions (2.10) are substituted into the Lagrangian (2.9), which is then averaged by integrating x and y from $-\infty$ to $+\infty$. ie,

$$\mathcal{L} = \int_{-\infty}^{+\infty} L dx dy. \tag{2.11}$$

By using Equations (2.10) and (2.11) the averaged Lagrangian is given by

$$\begin{aligned} \frac{\mathcal{L}}{\pi} = & -(a_x^2 w_x^2 + 2l_x^2 g_x^2)\sigma_x' + 2w_x^2 g_x a_x' + 4a_x w_x g_x w_x' - 2a_x w_x^2 g_x' - a_x^2 \\ & - \gamma(a_y^2 w_y^2 + 2l_y^2 g_y^2)\sigma_y' + 2\gamma w_y^2 g_y a_y' + 4\gamma a_y w_y g_y w_y' - 2\gamma a_y w_y^2 g_y' \\ & - \frac{1}{2}(1+\gamma^2)a_y^2 + \frac{2}{D}\alpha a_x a_y w_x^2 w_y^2 \beta^2 \cos\theta - \frac{1}{2}\nu\alpha^2 \\ & + \frac{1}{2}\alpha^2 \left[\frac{a_x^2 w_x^2 \beta^2}{\beta^2 + w_x^2} - \frac{a_y^2 w_y^2 \beta^2}{\beta^2 + w_y^2}\right] + i\epsilon(z)\left[\frac{a_x^2 w_x^2}{2} + \frac{a_y^2 w_y^2}{2} + g_x^2 l_x^2 + g_y^2 l_y^2\right]. \end{aligned} \tag{2.12}$$

Where $'$ represents derivative with respect to z.
Here, D and θ are given by,

$$D = \beta^2 w_x^2 + \beta^2 w_y^2 + w_x^2 w_y^2, \qquad \theta = \frac{z}{1+\gamma} - \sigma_x + \sigma_y. \tag{2.13}$$

The standard variational approach for the system is given by,

$$\frac{\partial \mathcal{L}}{\partial p_i} - \frac{d}{dz}\left(\frac{\partial \mathcal{L}}{\partial\, p_i'}\right) = 0, \tag{2.14}$$

where p_i corresponds to all parameters free to vary in the ansatz. In the ansatz chosen in Equation (2.10), $p_i(z) = a_x,\ a_y,\ w_x,\ w_y,\ \sigma_x,\ \sigma_y,\ g_x,\ g_y$, and α. The variational equations for the beam parameters are obtained as follows:

$$\begin{aligned} \frac{dw_x}{dz} = & -\frac{l_x^2 g_x}{a_x w_x^3} + \frac{2\alpha a_y w_x w_y^2 \beta^2 l_x^2 g_x}{a_x^2 D^2}(\beta^2 + w_x^2) cos\theta + \frac{\alpha a_y w_x w_y^2 \beta^2 sin\theta}{a_x D} \\ & - \frac{4\alpha a_y w_y^2 \beta^2 l_x^2 g_x}{w_x a_x^2 D^2}(\beta^2 w_x^2 - \beta^2 w_y^2 + w_x^2 w_y^2) cos\theta - \frac{i\epsilon(z) l_x^2 g_x}{2a_x w_x}, \end{aligned} \tag{2.15}$$

$$\begin{aligned}\frac{dw_y}{dz} = &-\frac{l_y^2 g_y(1+\gamma^2)}{2\gamma a_y w_y^3} + \frac{2\alpha a_x w_x^2 w_y \beta^2 l_y^2 g_y}{a_y^2 \gamma D^2}(\beta^2 + w_y^2)cos\theta - \frac{\alpha a_x w_x^2 w_y \beta^2 sin\theta}{a_y \gamma D} \\ &-\frac{4\alpha a_x w_x^2 \beta^2 l_y^2 g_y}{\gamma w_y a_y^2 D^2}(\beta^2 w_y^2 - \beta^2 w_x^2 + w_x^2 w_y^2)cos\theta - \frac{i\epsilon(z) l_y^2 g_y}{2\gamma a_y w_y},\end{aligned} \tag{2.16}$$

$$\begin{aligned}\frac{da_x}{dz} = &\frac{8\alpha a_y w_y^2 \beta^2 l_x^2 g_x}{a_x w_x^2 D^2}(\beta^2 w_x^2 - \beta^2 w_y^2 + w_x^2 w_y^2)cos\theta - \frac{2\alpha a_y w_y^2 \beta^2 sin\theta}{D} \\ &-\frac{2\alpha a_y w_y^2 \beta^2 l_x^2 g_x}{a_x D^2}(\beta^2 + w_x^2)cos\theta + \frac{i\epsilon(z) l_x^2 g_x}{w_x^2},\end{aligned} \tag{2.17}$$

$$\begin{aligned}\frac{da_y}{dz} = &\frac{8\alpha a_x w_x^2 \beta^2 l_y^2 g_y}{\gamma a_y w_y^2 D^2}(\beta^2 w_y^2 - \beta^2 w_x^2 + w_x^2 w_y^2)cos\theta + \frac{2\alpha a_x w_x^2 \beta^2 sin\theta}{\gamma D} \\ &-\frac{2\alpha a_x w_x^2 \beta^2 l_y^2 g_y}{\gamma a_y D^2}(\beta^2 + w_y^2)cos\theta + \frac{i\epsilon(z) l_y^2 g_y}{2\gamma w_y^2},\end{aligned} \tag{2.18}$$

$$\frac{dg_x}{dz} = \frac{a_x}{2w_x^2} - \frac{2\alpha a_y w_y^2 \beta^2}{D^2}(\beta^2 w_x^2 - \beta^2 w_y^2 + w_x^2 w_y^2)cos\theta, \tag{2.19}$$

$$\gamma\frac{dg_y}{dz} = \frac{(1+\gamma^2)a_y}{4w_y^2} - \frac{2\alpha a_x w_x^2 \beta^2}{D^2}(\beta^2 w_y^2 - \beta^2 w_x^2 + w_x^2 w_y^2)cos\theta, \tag{2.20}$$

$$\frac{d\sigma_x}{dz} = -\frac{2}{w_x^2} + \frac{2\alpha a_y w_x^2 w_y^2 \beta^2}{a_x D^2}(\beta^2 + w_x^2)cos\theta, \tag{2.21}$$

$$\gamma\frac{d\sigma_y}{dz} = -\frac{1+\gamma^2}{w_y^2} + \frac{2\alpha a_x w_x^2 w_y^2 \beta^2}{a_y D^2}(\beta^2 + w_y^2)cos\theta, \tag{2.22}$$

$$\alpha = \frac{2}{D}\frac{a_x a_y w_x^2 w_y^2 \beta^2 cos\theta}{\nu - \beta^2\Delta}, \qquad \Delta = \frac{a_x^2 w_x^2}{\beta^2 + w_x^2} - \frac{a_y^2 w_y^2}{\beta^2 + w_y^2}. \tag{2.23}$$

The method yields first-order ordinary coupled differential Equations (2.15) - (2.23). These equations are known as modulation equations. The standard fourth-order Runge Kutta method is employed to solve these modulation equations numerically.

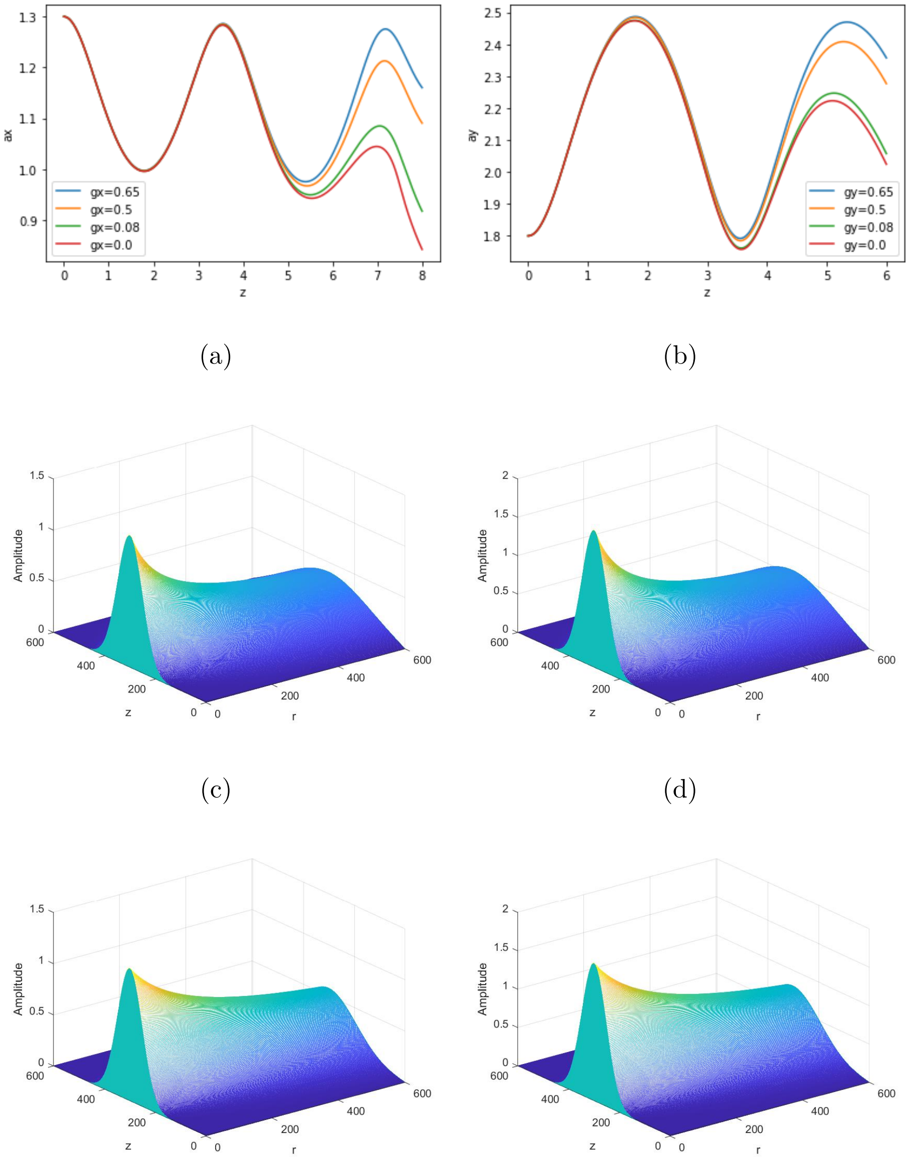

(a) (b)

(c) (d)

(e) (f)

Figure 2.3: Beam propagation with periodic damping plotted for damping coefficient $\epsilon_s = 3$ for an initial excitation with a_{x0}=1.3, a_{y0}=1.8, w_{x0}=12, w_{y0}=12, σ_{x0}=0, σ_{y0}=0. In the first row (Results of variational analysis): (a) evolution of amplitude along the x-direction, (b) evolution of amplitude along the y-direction. The second and third-row corresponds to numerical results. In the second row: (c) the evolution of amplitude along the x-direction, (d) evolution of amplitude along the y-direction for g_x=g_y=0; In the third row: (e) the evolution of amplitude along the x-direction, (f) evolution of amplitude along the y-direction for g_x=g_y=0.08.

The system of coupled partial differential equations given in the governing Equations (2.5) - (2.7) has been directly solved numerically using the finite difference method. In this method, a rectangular grid is imposed on the problem and the grid planes are spaced by Δz and Δr such that $z_k = k\Delta z$ and $r_n = n\Delta r$, respectively. The condition for stability is achieved by selecting $\frac{\Delta z}{\Delta r^2} \leq 0.5$. An initial trial function was chosen as per the variational ansatz as given in Equation (2.10). In the presence and absence of diffractive radiation, the beam propagation with different damping profiles is studied and these numerical results of Equations (2.5) - (2.7) are compared with the variational results.

2.3 Results and discussions

The analysis has been done to investigate the effect of diffractive radiation shed on various damping profiles such as constant damping, periodic damping, and hyperbolic damping. In all cases, the initial conditions are chosen as a_{x0}=1.3, a_{y0}=1.8, w_{x0}=12, w_{y0}=12, σ_{x0}=0, and σ_{y0}=0. The amplitude evolutions of the beam in two transverse directions are studied for different radiation shelf heights.

Constant damping

Figure (2.2) displays the beam propagation with constant damping plotted for damping coefficient $\epsilon_s = 3$. The solutions of modulation equations are plotted in Figures 2.2(a) and (b). They give the evolution of amplitude in two transverse directions for different values of the radiation shelf height. When the values of g_x and g_y are increased from 0 to 0.35, the damping is counterbalanced by the radiation shelf. The numerical analysis of Equations (2.5) - (2.7) using the finite difference method also shows that the damping effect can be counteracted by the radiation shelf as plotted in Figures 2.2(c)-(f). The second row represents the evolution of amplitude for g_x=g_y=0 and the third row represents the evolution of amplitude for g_x=g_y=0.08. The amplitudes along the transverse directions are damped as shown in Figures 2.2(c) and (d) respectively for g_x=g_y=0. In the presence of a radiation shelf with heights of 0.08, the damping effects of the amplitudes get reduced as depicted in Figures 2.2(e) and (f). The variational and numerical analysis show that here a large value of diffractive radiation is needed to counteract the effect of damping.

Periodic damping

Consider the periodic damping profile [8],

$$\epsilon(z) = \epsilon_s[cos(\omega(z - L/2)) + cos(\omega(z + L/2))], \tag{2.24}$$

where ϵ_s is the strength of damping and ω is the width of damping. The damping effect is counteracted by even higher diffractive radiation as compared to case 1 as shown in Figure (2.3). When the values of g_x and g_y are increased from 0 to 0.65, the damping effects are canceled. The variational results are shown in Figures 2.3(a) and (b). The amplitude variation with different radiation shelf heights obtained from the numerical analysis is shown in Figures 2.3(c)-(f). The second row represents the evolution of amplitude for g_x=g_y=0 and the third row represents the evolution of amplitude for g_x=g_y=0.08. The evolution of X and Y in the absence of radiation shelf are shown in Figures 2.3(c) and (d) respectively. Figures 2.3(e) and (f) show the amplitude evolutions for g_x=g_y=0.08. Both results show that the diffractive radiation can cancel the damping effect, but here its value is greater than that of the previous case.

Hyperbolic damping

When there is a hyperbolic damping profile in the medium in the form [8]

$$\epsilon(z) = \epsilon_s[sech(\omega(z - L/2)) + sech(\omega(z + L/2))], \tag{2.25}$$

the damping effect is compensated by very small diffractive radiation as shown in Figure (2.4). When the values of g_x and g_y are increased from 0 to 0.08, the damping effects are canceled. The first row represents the variational results.

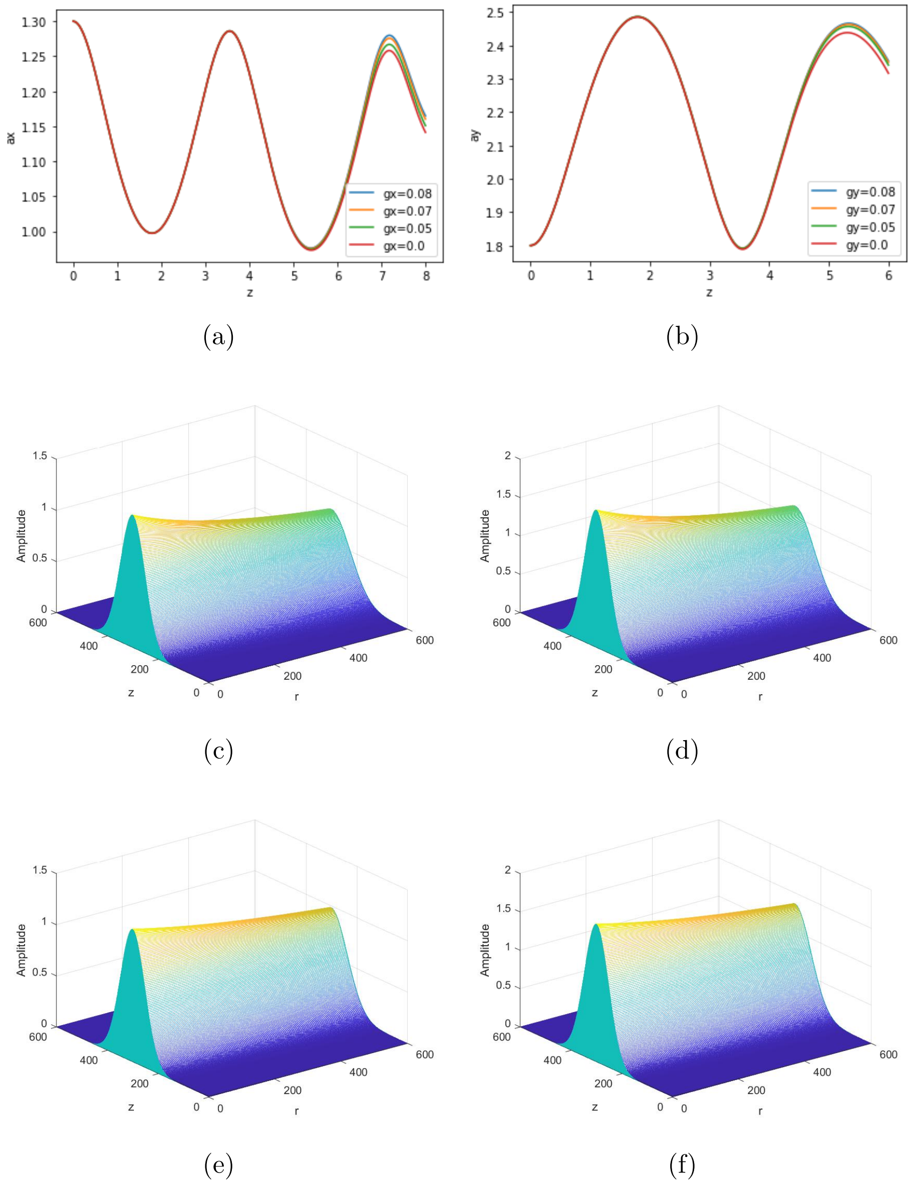

(a) (b)

(c) (d)

(e) (f)

Figure 2.4: Beam propagation with hyperbolic damping plotted for damping coefficient $\epsilon_s = 3$ for an initial excitation with a_{x0}=1.3, a_{y0}=1.8, w_{x0}=12, w_{y0}=12, σ_{x0}=0, σ_{y0}=0. In the first row (Results of variational analysis): (a) evolution of amplitude along the x-direction, (b) evolution of amplitude along the y-direction. The second and third-row corresponds to numerical results. In the second row: (c) the evolution of amplitude along the x-direction, (d) evolution of amplitude along the y-direction for g_x=g_y=0; In the third row: (e) the evolution of amplitude along the x-direction, (f) evolution of amplitude along the y-direction for g_x=g_y=0.08.

The numerical results are depicted in the second and third rows. The second and the third rows show the evolution of X and Y for g_x= g_y=0 and g_x= g_y=0.08 respectively. Figures 2.4(c) and (d) elucidate the evolution of X and Y for g_x=g_y=0. The damping of X and Y is canceled by the presence of diffractive radiation as shown in Figures 2.4(e) and (f) respectively. Both results show that a very small value of diffractive radiation can counterbalance the effect of hyperbolic damping.

From the above three cases, it is clear that the diffractive radiation helps the beam to evolve as a nematicon even if the medium has some kind of damping. In the case of constant and periodic damping, the damping effect is canceled by high diffractive radiation. But, a small value of diffractive radiation height can counteract the hyperbolic damping and as a result, the nematicon propagates through the medium.

2.4 Conclusion

This chapter analyzes the interplay between diffractive radiation and the damping coefficient in a nematic liquid crystal with nonlocal nonlinearity. The system is analyzed using both semi-analytical and numerical methods. When the damping profile is either constant or varies periodically along the propagation distance, nematicon propagation occurs only if the height of the diffractive radiation shelf is significant. However, even a very small diffractive radiation shelf height can offset the impact of hyperbolic damping on the beam, allowing the nematicon to propagate through the medium.

The damping effects addressed in the study are relevant in real-world systems where loss mechanisms such as absorption or scattering in materials occur. Understanding how to minimize or counteract such effects with diffractive radiation can enhance the performance and efficiency of soliton-based technologies. For example, in fiber optic communications, diffractive radiation helps maintain the stability of optical solitons over long distances, improving signal transmission by reducing signal loss and distortion. Furthermore, the study sheds light on the role of different damping mechanisms and their implications for the development of tunable optical devices. In these devices, the ability to control or adapt to different damping profiles could allow for more flexible and dynamic control of light propagation. This could be particularly useful in adaptive optics, nonlinear optics, and in systems requiring precise control over light-matter interactions.

The competition of thermal nonlinearity and self-focusing is analyzed in the next chapter.

Bibliography

[1] Pu S, Chen M, Li Y, Zhang L. Solitons in liquid crystals with competing nonlinearities. Optics Communications. 2019 nov;450:78-86.

[2] Karimi N, Virkki M, Alberucci A, Buchnev O, Kauranen M, Priimagi A, et al. Molding Optical Waveguides with Nematicons. Advanced Optical Materials. 2017 may;5(14):1700199.

[3] Aya S, Araoka F. Kinetics of motile solitons in nematic liquid crystals. Nature Communications. 2020 jun;11(1).

[4] Strinic AI, Belic MR. Beam Propagation in Nematic Liquid Crystals. Acta Physica Polonica A. 2007 nov;112(5):877-83.

[5] Assanto G, Smyth NF. Spin-optical solitons in liquid crystals. Physical Review A. 2020 sep;102(3):033501.

[6] Penzenstadler E, Trebin HR. Fine structure of point defects and soliton decay in nematic liquid crystals. Journal de Physique. 1989;50(9):1027-40.

[7] Kralj M, Kralj M, Kralj S. Topological Defects in Nematic Liquid Crystals: Laboratory of Fundamental Physics. physica status solidi (a). 2021 feb;218(17):2000752.

[8] Xia W. Refraction of Nonlinear Light Beams in Nematic Liquid Crystals; 2012. Edinburgh, UK. Ph.D. thesis, University of Edinburgh.

Chapter 3

Competition of Nonlinearities in Nematicon Dynamics

This chapter investigates the thermal behavior of single-peak and double-peak solitons in a nematic liquid crystal through numerical simulations. Single-peak nematicons can be obtained at low thermal response coefficients, where the focusing reorientational nonlinearity dominates. Conversely, at higher thermal response coefficients, the defocusing thermal nonlinearity surpasses the focusing reorientational nonlinearity, causing the beam to broaden, form a flat-top profile, and eventually split into double-peak nematicons. Linear stability analysis reveals that single-peak nematicons remain stable regardless of thermal response coefficient values, while double-peak nematicons are stable only at high thermal response coefficient values. Understanding the thermal responses of nematicons can aid in the development of all-optical switches and laser beam shaping.

The results of this chapter are published as:

- N. M. Sajitha, T. P. Suneera, 'Thermal response of single-peak and double-peak nematicons'. The European Physical Journal Plus. 2023 Dec; 138(12): Article ID 1073.

3.1 Introduction

Numerous theoretical and experimental investigations have been conducted on thermo-reorientational solitary waves arising from competing nonlinear effects [1, 2]. These waves form as a result of the nonlocal refractive index response to extraordinary polarized light beams, which undergo both self-focusing due to molecular reorientation and self-defocusing due to heat generated by optical absorption [3, 4]. The latter process can be facilitated through appropriate dye doping, where photon energy is absorbed from the beam and converted into heat [2, 5]. In media with a single type of nonlocal nonlinearity, complex soliton structures are often unstable. However, the coexistence of focusing reorientational and defocusing thermal nonlinearities stabilizes these complex soliton structures [6, 7].

This chapter is driven by the intent to explore the influence of different nonlinear effects on soliton behavior in nematic liquid crystals, particularly highlighting the roles of focusing reorientational and defocusing thermal nonlinearities. By numerically investigating these dynamics, the research aims to clarify how thermal responses affect the structure and stability of solitons. This understanding could have implications for optimizing soliton behavior in optical applications, where controlling beam shape and stability is crucial. The study is particularly interested in exploring how varying thermal response coefficients lead to the formation of either single-peak or double-peak nematicons, and how these solitons maintain stability under different conditions.

This study holds significance for two key reasons. Firstly, it sheds light on the dynamic relationship between focusing reorientational nonlinearity and defocusing thermal nonlinearity. This balance plays a crucial role in managing the stability and behavior of optical beams in a range of liquid crystal based devices. Secondly, the findings on the stability of solitons, particularly the impact of thermal response coefficients on their ability to withstand perturbations, are essential for designing stable optical systems. Gaining a deeper understanding of these mechanisms is vital for advancing liquid crystal technologies in areas such as telecommunications, signal processing, and optical data storage.

This chapter considers the thermal response of single-peak and double-peak nematicons in the nonlocal regime. The beam propagation in the NLC has been studied for various values of thermal response coefficients. This chapter is organized as follows. Section 3.2 describes the theoretical model for beam propagation in a nematic liquid crystal in the nonlocal regime. The governing equations of the system are solved using the finite difference method. The results and discussions are presented in section 3.3. In section 3.4, the stability of the solutions against the small perturbations has been investigated using linear stability analysis. Section 3.5 concludes the chapter.

3.2 Theoretical model

Consider an optical beam which propagates through a positive uniaxial NLC along the z-direction as shown in Figure (3.1). The optic axis of the nematic is aligned along the y-axis and the director angle ξ describes its reorientation in the xy plane. The governing equations of the beam are given by [2, 8–10]

$$2ik_0n_{\perp}\frac{\partial E_x}{\partial z}+\frac{\partial^2 E_x}{\partial x^2}+\frac{\partial^2 E_x}{\partial y^2}+k_o^2\epsilon_a E_x sin^2\xi+\frac{1}{2}k_0^2\epsilon_a E_y e^{ik_0(n_{\parallel}-n_{\perp})z}sin2\xi=0, \tag{3.1}$$

$$2ik_0n_{\parallel}\frac{\partial E_y}{\partial z}+\frac{\partial^2 E_y}{\partial x^2}+\frac{n_{\parallel}^2}{n_{\perp}^2}\frac{\partial^2 E_y}{\partial y^2}-k_o^2\epsilon_a E_y sin^2\xi+\frac{1}{2}k_0^2\epsilon_a E_x e^{-ik_0(n_{\parallel}-n_{\perp})z}sin2\xi=0. \tag{3.2}$$

Here, E_x and E_y represent the x and y components of the electric fields. k_0 denotes the ordinary wave vector. The refractive indices parallel and perpendicular to the director alignment are denoted by $n_{\parallel}$ and $n_{\perp}$, respectively. ϵ_a denotes the nematic birefringence and is related with the refractive indices by ϵ_a=$n_{\parallel}^2-n_{\perp}^2$.

The governing equation of the molecular director is given by [10]

$$K\nabla^2\xi+\frac{1}{4}\epsilon_0\epsilon_a\left[2(\mid E_x\mid^2-\mid E_y\mid^2)sin2\xi+2ReE_xE_y^*e^{-ik_0(n_\parallel-n_\perp)z}cos2\xi\right]=0. \quad (3.3)$$

Here, ∇^2 is the two-dimensional Laplacian. K denotes the elastic constant of the medium, which is assumed to be the same for bend, splay, and twist deformations of the NLC molecules.

The localized heating produced by light absorption causes the thermo-optic changes in the material properties of the NLC. Hence the refractive indices $n_\parallel$ and $n_\perp$ as well as the elastic constant K of the medium are temperature dependent.

The equation of the heat flow is given by [11]

$$S\nabla^2T=-\alpha\Gamma\mid E\mid^2, \qquad \text{where,} \quad \Gamma=\frac{1}{2}\epsilon_0cn_e. \quad (3.4)$$

S denotes thermal conductivity, α be the thermal absorption coefficient of the material, and T is the temperature. ϵ_0 and c represent the permittivity of free space and the velocity of light in vacuum respectively. The refractive index n_e of the extraordinary polarized waves is given by

$$n_e^2=\frac{n_\parallel^2n_\perp^2}{n_\parallel^2cos^2\xi+n_\perp^2sin^2\xi}. \quad (3.5)$$

Let T_0 be the NLC temperature in the absence of the beam, and A_T represents the typical temperature increase brought on by the beam. Then $T=T_0+A_T\tau$, where the variation of the nondimensional temperature from T_0 is denoted by τ. We get the heat equation in the nondimensional form as

$$\mu_T\nabla^2\tau=-\mid X\mid^2-\mid Y\mid^2, \qquad \text{where,} \quad \mu_T=\frac{SA_T}{\alpha\Gamma W_b^2A_b^2}, \quad (3.6)$$

where μ_T is the nondimensional thermal diffusivity [3]. A_b and W_b are the amplitude and width of the beam respectively.

Figure 3.1: The interaction geometry. A nematic liquid crystal with ellipses which have long axes parallel to y is used to represent the elongated NLC. The input light beam is shown with a green arrow impinging normally to the molecular director on the sample. The angle ξ describes the reorientation of the optic axis, n in the (x, y) plane.

The equations of the x and y components of the electric field of the beam are given by

$$E_x = Xe^{ik_0 n_\perp z}, \qquad E_y = Ye^{ik_0 n_\parallel z}. \tag{3.7}$$

X and Y are the amplitudes of electric fields in two transverse directions. When Equation (3.7) is substituted in Equations (3.1) - (3.3) and taking into account the temperature dependence on material parameters, and nondimensionalizing Equations (3.1) - (3.3), we get

$$2i\frac{\partial X}{\partial z} + \frac{\partial^2 X}{\partial x^2} + \frac{\partial^2 X}{\partial y^2} + Xsin^2\xi + \frac{1}{2}Ye^{\frac{iz}{1+\gamma(\tau)}}sin2\xi = 0, \tag{3.8}$$

$$2i\gamma(\tau)\frac{\partial Y}{\partial z} + \frac{\partial^2 Y}{\partial x^2} + \gamma(\tau)^2\frac{\partial^2 Y}{\partial y^2} - Ysin^2\xi + \frac{1}{2}Xe^{\frac{-iz}{1+\gamma(\tau)}}sin2\xi = 0, \tag{3.9}$$

$$\nu(\tau)\nabla^2\xi + (\mid X \mid^2 - \mid Y \mid^2)sin2\xi + 2Re(XY^* e^{\frac{-iz}{1+\gamma(\tau)}})cos2\xi = 0. \tag{3.10}$$

The nonlocality (ν) and the anisotropy (γ) are temperature dependent. They are related to the elastic constant K and the extra-ordinary refractive index n_e by the equations [11],

$$\nu = \frac{8K}{\epsilon_0 \epsilon_a A_b^2 W_b^2 sin2\xi}, \quad \gamma = \frac{2n_e}{\sqrt{\epsilon_a sin2\xi}}. \tag{3.11}$$

According to experimental measurements, the refractive index eigenvalues for the standard NLC mixture E7 vary nearly linearly with temperature up to about 40^0C [11]. Refractive index $n_{\|}$ decreases by approximately 0.6% between 20 and 40 degrees Celsius, while $n_{\perp}$ increases by approximately 1.3% [10, 11]. As a result, $\gamma(\tau)$ can be expanded to second order in a Taylor series as $\gamma(\tau) = 1 - \gamma_1 \tau$, where γ_1 is related to $\frac{d\gamma}{d\tau}$ at $T = T_0$.

The numerical solutions to the system of Equations (3.8) - (3.10) has been found using the finite difference method. In this method, a rectangular grid is imposed on the problem and the grid planes are separated by Δz and Δr such that $z_k = k\Delta z$ and $r_n = n\Delta r$, respectively. The stability requirement is fulfilled by selecting $\frac{\Delta z}{\Delta r^2} \leq 0.5$. The solutions of the Equations (3.8) and (3.9) are selected as [3],

$$X = a_x \left[e^{\frac{-(r-m)^2}{w_x^2}} + e^{\frac{-(r+m)^2}{w_x^2}} \right] e^{i\sigma_x}, \qquad Y = a_y \left[e^{\frac{-(r-m)^2}{w_y^2}} + e^{\frac{-(r+m)^2}{w_y^2}} \right] e^{i\sigma_y}, \tag{3.12}$$

where $r^2 = x^2 + y^2$. The amplitudes of the beam are a_x and a_y, widths are w_x and w_y, and the phases are σ_x and σ_y along the two transverse directions.
The solutions of the Equation (3.10) is selected as [12],

$$\xi = \alpha e^{\frac{-r^2}{\beta^2}} + A \left[Ei \left(\frac{-r^2}{\beta^2} \right) - ln \left(\frac{r^2}{d^2} \right) \right]. \tag{3.13}$$

Here, the first term represents the local contribution, while the second and third terms represent the nonlocal contributions of the director angle. α and A represent the amplitudes of the local and nonlocal contributions of the director respectively and β be the width of the director. α depends on the propagation distance z

through the relation [13],

$$\alpha = \frac{2}{D}\frac{a_x a_y w_x^2 w_y^2 \beta^2 cos\theta}{\nu - \beta^2\Delta}, \tag{3.14}$$

where,

$$D = \beta^2 w_x^2 + \beta^2 w_y^2 + w_x^2 w_y^2, \quad \theta = \frac{z}{1+\gamma} - \sigma_x + \sigma_y, \quad \Delta = \frac{a_x^2 w_x^2}{\beta^2 + w_x^2} - \frac{a_y^2 w_y^2}{\beta^2 + w_y^2}. \tag{3.15}$$

The thickness of the NLC cell is represented by L. Then $d = L/2$. β is given by the relation, $\beta = L/(2\ln 100)$. Ei denotes the exponential integral function.

$$E_i = -\int_{-z}^{+\infty} e^{-t} t^{-1} dt. \tag{3.16}$$

The solutions to the radially symmetric heat Equation (3.6) are $\ln r$ and a constant. We assume that the temperature within the circular peak of nematicon is constant due to the high thermal diffusivity μ_T. As the homogeneous solution moves away from the axis, the temperature decreases [3].

$$\tau = \tau_0, \quad 0 \le r \le m; \qquad \tau = \tau_1 \ln\frac{R}{r}, \quad m < r < R. \tag{3.17}$$

Furthermore, it obeys the boundary condition $\tau = 0$ at $r = R$.

The propagation of the beam has been analyzed in a nematic liquid crystal in the nonlocal regime and the numerical results of Equations (3.8) - (3.10) are presented graphically in section 3.3.

3.3 Results and discussions

The analysis has been done to investigate the thermal response of single-peak and double-peak nematicons in a uniaxial NLC. The initial conditions are chosen as a_{x0}=1.5, a_{y0}=1.2, w_{x0}=12, w_{y0}=12, σ_{x0}=0, and σ_{y0}=0. We studied the propagation of the nematicons through uniaxial NLC for different values of thermal response coefficients. We solved Equations (3.8) - (3.10) numerically employing the finite difference method. The different parameters are chosen as $\mu_T = 300$, $\nu = 600$, $\gamma_1 = 0.1$, $\alpha = 2$, $A = 0.5$, and $m = 2.2$.

Let the medium has no thermal response initially. The thermal response coefficients (τ_0 and τ_1) are zero in this case. Figures 3.2(a) and (b) depict the evolution of amplitude along the x and y directions respectively. The nematicons have a single-peak if there is no thermal response as shown in Figures 3.2(a) and (b). The study was carried out for a range of thermal response coefficients. The single-peak nematicons are obtained for the thermal coefficients within the range 0.1 to 0.3. Here, for low values of thermal response coefficients, the nonlinearity is mainly driven by the molecular reorientation, and the nematicons have a typical single-peak shape.

When the thermal response coefficients are $\tau_0 = \tau_1 = 0.5$, the evolutions of the beam along two transverse directions are shown in Figures 3.3(a) and (b) respectively. The beam broadens and develops a flat top. As the thermal response coefficients increase, defocusing thermal nonlinearity dominates over focusing reorientational nonlinearity. Hence the beam exhibits the particular behavior as shown in Figure (3.3).

Figures (3.4) and (3.5) depict the advancement of the beam when the thermal response coefficients are $\tau_0 = \tau_1 = 0.6$, and $\tau_0 = \tau_1 = 1.0$ respectively. When $\tau_0 = \tau_1 = 0.6$, a dip is formed on the flat top of the beam along the two transverse directions as evident in Figures 3.4(a) and (b). The dip formed becomes much deeper as the thermal response coefficients increase from 0.6 to 1.0 as elucidated in Figures 3.5(a) and (b). When the thermal response coefficients increase, defocusing thermal nonlinearity exceeds focusing reorientational nonlinearity.

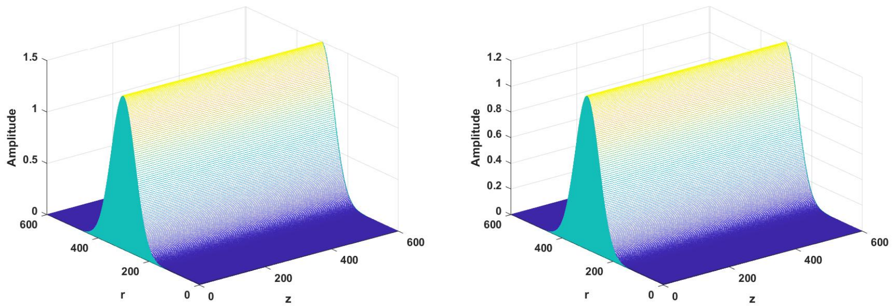

(a) (b)

Figure 3.2: Evolution of the amplitude in two transverse directions for $\tau_0 = \tau_1 = 0$: (a) Along the x-direction, and (b) along the y-direction.

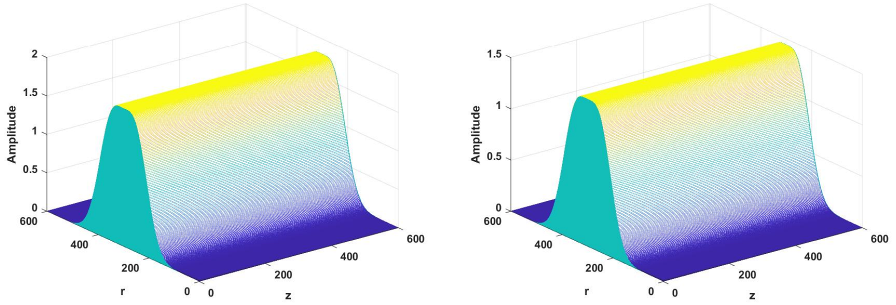

(a) (b)

Figure 3.3: Evolution of the amplitude in two transverse directions for $\tau_0 = \tau_1 =$ 0.5: (a) Along the x-direction, and (b) along the y-direction.

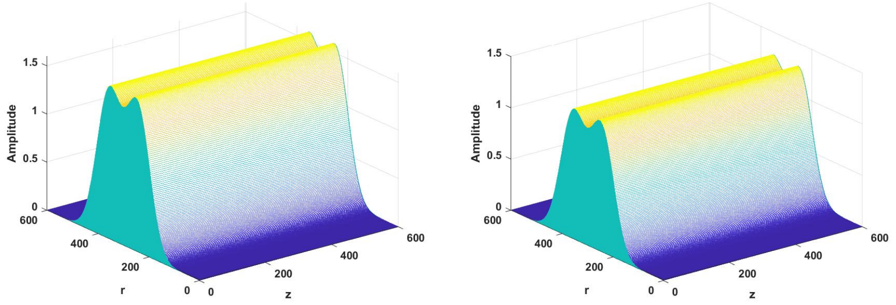

(a) (b)

Figure 3.4: Evolution of the amplitude in two transverse directions for $\tau_0 = \tau_1 =$ 0.6: (a) Along the x-direction, and (b) along the y-direction.

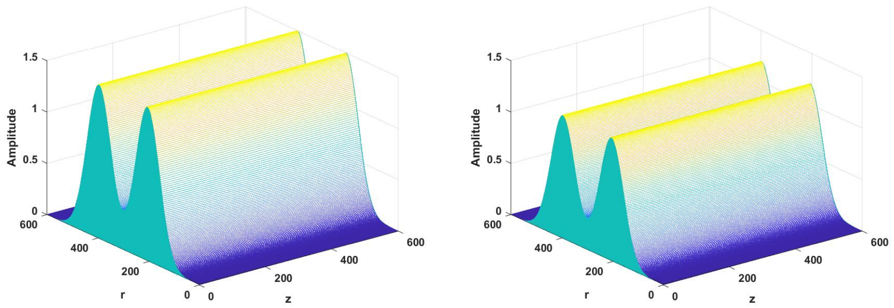

(a) (b)

Figure 3.5: Evolution of the amplitude in two transverse directions for $\tau_0 = \tau_1 =$ 1.0: (a) Along the x-direction, and (b) along the y-direction.

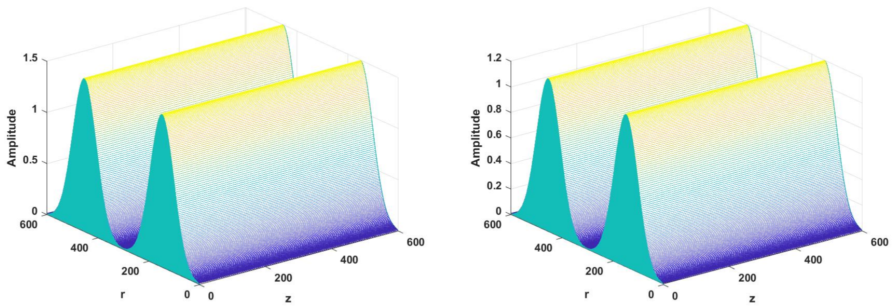

(a) (b)

Figure 3.6: Evolution of the amplitude in two transverse directions for $\tau_0 = \tau_1 =$ 1.6: (a) Along the x-direction, and (b) along the y-direction.

When the thermal response coefficient increases further, the dip between two peaks increases and finally splits into two distinct peaks at $\tau_0 = \tau_1 = 1.6$ as shown in Figure (3.6). Figures 3.6(a) and (b) depict the advancement of amplitude along x and y directions. For large values of thermal response coefficients, the defocusing thermal nonlinearity is significantly greater than the focusing reorientational nonlinearity. As a result, the output beam profile splits and transforms into double-peak nematicons at $\tau_0 = \tau_1 = 1.6$.

From the above results, it is clear that the beam evolves as single-peak nematicons for low values of thermal response coefficients. The focusing reorientational nonlinearity prevails over the defocusing thermal nonlinearity in this regime. For comparatively large values of thermal response coefficients, the defocusing thermal nonlinearity exceeds the focusing reorientational nonlinearity. As a result, the beam broadens and develops a flat top, and eventually splits into double-peak nematicons. The relative strengths of the focusing reorientational and defocusing thermal nonlinearities have a significant influence on the transition from single-peak to double-peak nematicons.

3.4 Linear stability analysis

The solutions of the system has been studied in terms of the propagation constant μ:

$$P \quad = Xexp(-i\mu z), \qquad Q \quad = Yexp(-i\mu z). \tag{3.18}$$

The substitution of P and Q in Equations (3.8) and (3.9) give eigenvalue problem:

$$2i\frac{\partial P}{\partial z} + \frac{\partial^2 P}{\partial x^2} + \frac{\partial^2 P}{\partial y^2} + Psin^2\xi + \frac{1}{2}Qe^{\frac{iz}{1+\gamma(\tau)}}sin2\xi = -2\mu P, \tag{3.19}$$

$$2i\gamma(\tau)\frac{\partial Q}{\partial z} + \frac{\partial^2 Q}{\partial x^2} + \gamma(\tau)^2\frac{\partial^2 Q}{\partial y^2} - Qsin^2\xi + \frac{1}{2}Pe^{\frac{-iz}{1+\gamma(\tau)}}sin2\xi = -2\mu\gamma Q. \tag{3.20}$$

The linear stability of the stationary states of the coupled system has been investigated using Bogoliubov-de Gennes (BDG) equations. Consider small perturbations of the stationary states of the system as:

$$R = P + a(r,z)exp(-i\mu z), \qquad S = Q + b(r,z)exp(-i\mu z), \tag{3.21}$$

where,

$$a(r,z) = a_1(r)exp(i\lambda z) + a_2(r)exp(-i\lambda^* z), \tag{3.22}$$

$$b(r,z) = b_1(r)exp(i\lambda z) + b_2(r)exp(-i\lambda^* z), \tag{3.23}$$

where the asterisk indicates the complex conjugation. Assuming a_1, a_2, b_1, and b_2 are very small, the pair of coupled Equations (3.19) and (3.20) are linearized after being transformed into radial coordinates. This results in a set of four homogeneous equations that are satisfied by a_1, a_2, b_1, and b_2, and are shown in matrix form below:

$$\lambda \begin{pmatrix} a_1 \\ a_2^* \\ b_1 \\ b_2^* \end{pmatrix} = C \begin{pmatrix} a_1 \\ a_2^* \\ b_1 \\ b_2^* \end{pmatrix}, \tag{3.24}$$

where the matrix C is given by,

$$\begin{pmatrix} L_1 & 0 & \frac{1}{4} e^{\frac{iz}{1+\gamma(\tau)}} sin2\xi & \frac{R^2}{2} \\ \frac{R^2}{2} & -L_1 & 0 & -\frac{1}{4} e^{\frac{-iz}{1+\gamma(\tau)}} sin2\xi \\ \frac{1}{4\gamma(\tau)} e^{\frac{-iz}{1+\gamma(\tau)}} sin2\xi & \frac{S^2}{2} & L_2 & 0 \\ 0 & -\frac{1}{4\gamma(\tau)} e^{\frac{iz}{1+\gamma(\tau)}} sin2\xi & \frac{S^2}{2} & -L_2 \end{pmatrix}, \tag{3.25}$$

$$L_1 = \frac{1}{2} \left(\frac{d^2}{dr^2} + \frac{1}{r}\frac{d}{dr} + sin^2\xi + |R|^2 + 2\mu \right), \tag{3.26}$$

$$L_2 = \frac{1}{2\gamma} \left(\frac{d^2}{dr^2} + \frac{1}{r}\frac{d}{dr} - sin^2\xi + |S|^2 + 2\gamma\mu \right). \tag{3.27}$$

Spectral methods based on Chebyshev polynomials are used to solve the system. To evaluate the diffraction operators, a grid is chosen that extends 40 along r.

The perturbation eigenvalues have been studied as functions of the propagation constants. The type of eigenvalue determines the stability of the solution. Any eigenvalue with an imaginary part will cause the perturbed solution to grow exponentially with z, resulting in the corresponding solutions being linearly unstable. If all imaginary eigenvalues are equal to zero, the solutions are completely stable.

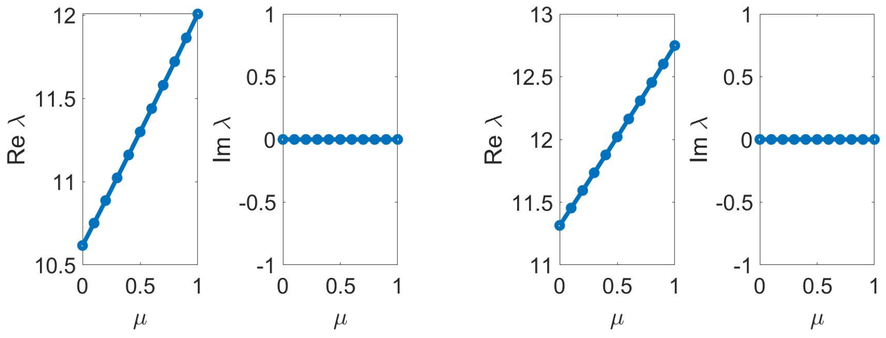

(a) (b)

Figure 3.7: The results of linear stability analysis of the system for thermal response coefficients (a) $\tau_0 = \tau_1 = 0$, and (b) $\tau_0 = \tau_1 = 0.2$. The real and imaginary parts of the perturbation eigenvalues (λ) versus the propagation constant μ are shown.

Figures (3.7) and (3.8) show stability plots for various values of thermal response coefficients. Figure (3.7) depicts the stability plots for single-peak nematicons for zero and low values of thermal response coefficients. Figures 3.7(a), and (b) show that for thermal response coefficients $\tau_0 = \tau_1 = 0$, and $\tau_0 = \tau_1 = 0.2$ the magnitudes of imaginary eigenvalues are zero, indicating that the corresponding solutions are linearly stable. That is, single-peak nematicons are linearly stable.

Figure (3.8) shows stability plots for double-peak nematicons with various thermal response coefficient values. Figure 3.8(a) shows the stability plots for the thermal response coefficients $\tau_0 = \tau_1 = 0.5$, while Figure 3.8(b) shows the stability plots for the thermal response coefficients $\tau_0 = \tau_1 = 0.6$. The stability plots for the thermal response coefficients $\tau_0 = \tau_1 = 1.0$ are shown in Figure 3.8(c). The magnitudes of imaginary eigenvalues in Figures 3.8(a)-(c) are not zero, indicating that the corresponding solutions are linearly unstable. Solutions with purely real eigenvalues are stable for double-peak nematicons with $\tau_0 = \tau_1 = 1.6$, as shown in Figure 3.8(d).

According to the linear stability analysis, single-peak nematicons are stable irrespective of thermal response coefficient values (τ_0 and τ_1 from 0 to 0.3) whereas double-peak nematicons are stable only when $\tau_0 = \tau_1 = 1.6$. The thermal

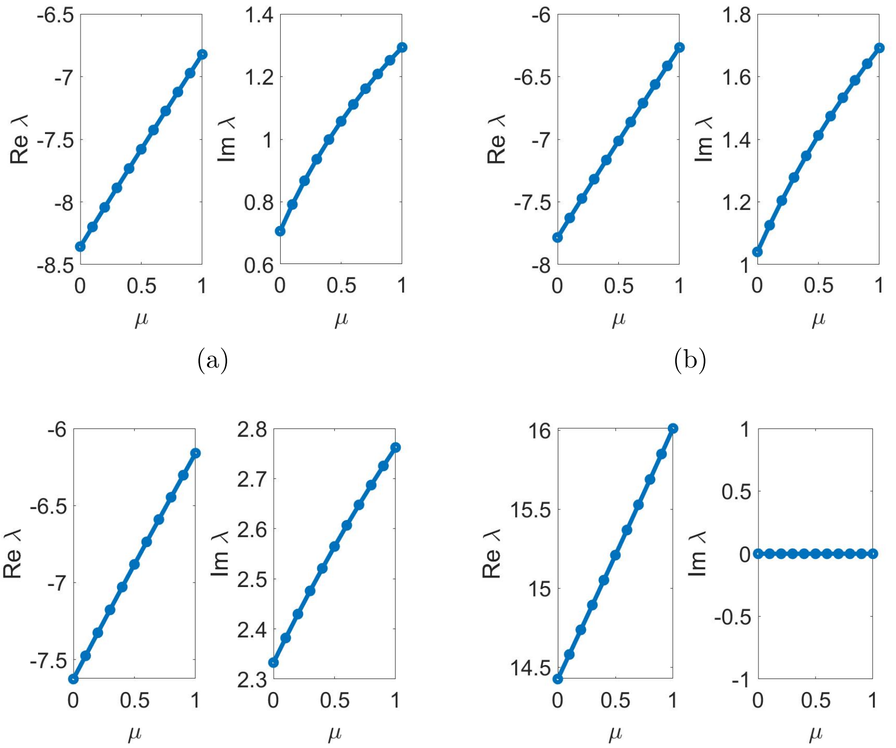

(a) (b)

(c) (d)

Figure 3.8: The results of linear stability analysis of the system for thermal response coefficients (a) $\tau_0 = \tau_1 = 0.5$, (b) $\tau_0 = \tau_1 = 0.6$, (c) $\tau_0 = \tau_1 = 1.0$, and (d) $\tau_0 = \tau_1 = 1.6$. The real and imaginary parts of the perturbation eigenvalues (λ) versus the propagation constant μ are shown.

response coefficients have a considerable impact on the stabilization of double-peak nematicons. The thermal response coefficients reduce the total nonlinear response of the medium, making the beam more resistant to perturbation.

3.5 Conclusion

The thermal response of single-peak and double-peak solitons in a nematic liquid crystal has been investigated through numerical simulations. Single-peak nematicons emerge when the thermal response coefficients are relatively low, with the focusing reorientational nonlinearity being dominant in this range. However, as the thermal response coefficients increase, the defocusing thermal nonlinearity surpasses the focusing reorientational nonlinearity, causing the beam to expand, flatten at the top, and eventually split into double-peak nematicons. The interaction between the focusing reorientational and defocusing thermal nonlinearities gives rise to both single-peak and double-peak nematicons. Stability analysis indicates that single-peak nematicons remain stable regardless of thermal response coefficient values, while double-peak nematicons exhibit stability only at higher thermal response coefficients. These coefficients significantly influence the formation and stability of double-peak nematicons, reducing the overall nonlinear response of the medium and making the beam more resistant to perturbations.

The transition between single-peak and double-peak nematicons, triggered by thermal effects, can be employed in designing all-optical switches. These switches which rely solely on light without needing electronic components are essential for faster more efficient photonic circuits. The broadening and splitting of beams due to defocusing thermal nonlinearity can be applied in laser beam shaping. This is useful for applications requiring precise control of beam profiles such as in medical laser systems, material processing, or optical trapping.

Bibliography

[1] Khan CC. Thermal effects on nonlinear optical beam propagation in nematic liquid crystals. The University of Edinburgh; 2021.

[2] Alberucci A, Laudyn UA, Piccardi A, Kwasny M, Klus B, Karpierz MA, et al. Nonlinear continuous-wave optical propagation in nematic liquid crystals: Interplay between reorientational and thermal effects. Physical Review E. 2017 Jul;96(1):012703.

[3] Assanto G, Khan C, Smyth NF. Multihump thermo-reorientational solitary waves in nematic liquid crystals: Modulation theory solutions. Physical Review A. 2021 jul;104(1):013526.

[4] Jung PS, Krolikowski W, Laudyn UA, Trippenbach M, Karpierz MA. Supermode spatial optical solitons in liquid crystals with competing nonlinearities. Physical Review A. 2017 feb;95(2):023820.

[5] Smyth NF, Assanto G, Skuse BD. Optical path control of solitary waves in dye-doped nematic liquid crystals. Photonics Letters of Poland. 2009 dec;1(4).

[6] Esbensen BK, Bache M, Bang O, Krolikowski W. Anomalous interaction of nonlocal solitons in media with competing nonlinearities. Physical Review A. 2012 sep;86(3):033838.

[7] Kartashov YV, Vysloukh VA, Torner L. Stabilization of higher-order vortices and multihump solitons in media with synthetic nonlocal nonlinearities. Physical Review A. 2009 jan;79(1):013803.

[8] Sajitha NM, Suneera TP. Interplay between diffractive radiation shed and damping coefficient on nematicon propagation. Journal of Modern Optics. 2022 nov;69(20):1134-41.

[9] Dong L, Ye F. Stability of multipole-mode solitons in thermal nonlinear media. Physical Review A. 2010 jan;81(1):013815.

[10] Laudyn UA, Piccardi A, Kwasny M, Karpierz MA, Assanto G. Thermo-optic soliton routing in nematic liquid crystals. Optics Letters. 2018 may;43(10):2296.

[11] Assanto G, Khan C, Piccardi A, Smyth NF. Temperature control of nematicon trajectories. Physical Review E. 2019 dec;100(6):062702.

[12] Aleksić NB, Petrović MS, Strinić AI, Belić MR. Solitons in highly nonlocal nematic liquid crystals: Variational approach. Physical Review A. 2012 mar;85(3):033826.

[13] Sajitha NM, Suneera TP. The effect of parabolic potential on the generation of higher harmonics of nematicons. Physica Scripta. 2023 Apr;98(5):055502.

Chapter 4

Higher Harmonic Generation in NLC

This chapter explores the dynamics of nonlocal spatial optical solitons within a uniaxial nematic liquid crystal subjected to a parabolic potential. The governing equations are solved using semi-analytical and numerical methods. The findings confirm the existence of nematicons under the effect of the parabolic potential, where they exhibit periodic oscillatory behavior. The oscillation wavelength is found to decrease linearly as the potential strength increases. Additionally, adjusting the strength of the parabolic potential enables the generation of higher harmonics of nematicons. The stability of the stationary solutions to small perturbations is analyzed using the Bogoliubov–de Gennes equations. The ability to generate higher harmonics of nematicons by adjusting the parabolic potential paves the way for new developments in nonlinear optics.

The results of this chapter are published as:

- N. M. Sajitha, T. P. Suneera, ‘The effect of parabolic potential on the generation of higher harmonics of nematicons’. Physica Scripta. 2023 Apr; 98(5): 055502.

4.1 Introduction

Phase matching is crucial for efficient harmonic generation in nonlinear optical processes ensuring that interacting waves maintain a consistent phase relationship during propagation. This coherence maximizes energy transfer from the fundamental frequency to its harmonics. In nematic liquid crystals, achieving phase matching for harmonic generation can be complex due to their anisotropic and reconfigurable refractive indices. By applying external electric or magnetic fields, one can manipulate the molecular orientation of NLCs thereby adjusting their optical properties to meet phase-matching conditions. This tunability makes NLCs promising candidates for applications in nonlinear optics particularly in scenarios requiring dynamic control over phase-matching conditions [1]. In quantum systems such as cylindrical parabolic quantum wires the application of a parabolic potential has been shown to affect third-harmonic generation. The study of these systems offers valuable information on the impact of parabolic potentials on harmonic generation processes [2]. When an electromagnetic wave passes through a doped NLC it interacts with the medium which can be understood as a perturbation [3, 4]. Harmonic generation in NLCs finds applications in various fields such as photonics, spectroscopy, and microscopy [1, 5, 6].

The motivation behind this study is to deepen our understanding of the nematicons within a uniaxial nematic liquid crystal subjected to a parabolic potential. This research aims to explore how the parabolic potential influences the formation, oscillatory behavior, and stability of nematicons. The study seeks to uncover the relationship between the strength of the parabolic potential and the properties of nematicons, such as oscillation wavelength and harmonic generation by employing both semi-analytical and numerical methods as well as evaluate their stability through small perturbation analysis using Bogoliubov-de Gennes equations.

This chapter considers the behavior of nematicons in the presence of a parabolic potential. The beam propagation in the NLC is analyzed with various strengths of parabolic potential. It is found that higher harmonics of nematicons can be generated by tuning the strength of the parabolic potential in a properly doped nematic liquid crystal. This chapter is organized as follows. In section 4.2, the theoretical model for beam propagation in a nematic liquid crystal with nonlocal nonlinearity having a parabolic potential is described. The equations governing the system are solved using semi-analytic and numerical methods. Section 4.3 presents the results and discussions. The stability of the solution against small perturbations has been examined using linear stability analysis in section 4.4. Section 4.5 concludes the chapter.

4.2 Theoretical model

Take into account an optical beam that is moving through a positive uniaxial NLC in the z-direction. The optic axis of the nematic is aligned along the y-direction and the reorientation of the optic axis in the xy plane is described by the angle ξ as shown in Figure (4.1). A perturbation is brought about on an electromagnetic beam when it passes through the doped NLCs. This perturbation appears as the potential of the medium. The system is modeled by a nonlinear Schrodinger-type equation with a parabolic potential for the optical beam and an elliptic Poisson equation for the molecular director. The governing equations of the system are given by

$$2ik_0n_\perp\frac{\partial E_x}{\partial z}+\frac{\partial^2 E_x}{\partial x^2}+\frac{\partial^2 E_x}{\partial y^2}+k_o^2\epsilon_a E_x sin^2\xi+\frac{1}{2}k_0^2\epsilon_a E_y e^{ik_0(n_\parallel-n_\perp)z}sin2\xi +V(x,y)E_x=0, \tag{4.1}$$

$$2ik_0n_\parallel\frac{\partial E_y}{\partial z}+\frac{\partial^2 E_y}{\partial x^2}+\frac{n_\parallel^2}{n_\perp^2}\frac{\partial^2 E_y}{\partial y^2}-k_o^2\epsilon_a E_y sin^2\xi+\frac{1}{2}k_0^2\epsilon_a E_x e^{-ik_0(n_\parallel-n_\perp)z}sin2\xi -V(x,y)E_y=0, \tag{4.2}$$

$$K\nabla^2\xi+\frac{1}{4}\epsilon_0\epsilon_a\left[2(|E_x|^2-|E_y|^2)sin2\xi+2ReE_xE_y^*e^{-ik_0(n_\parallel-n_\perp)z}cos2\xi\right]=0. \tag{4.3}$$

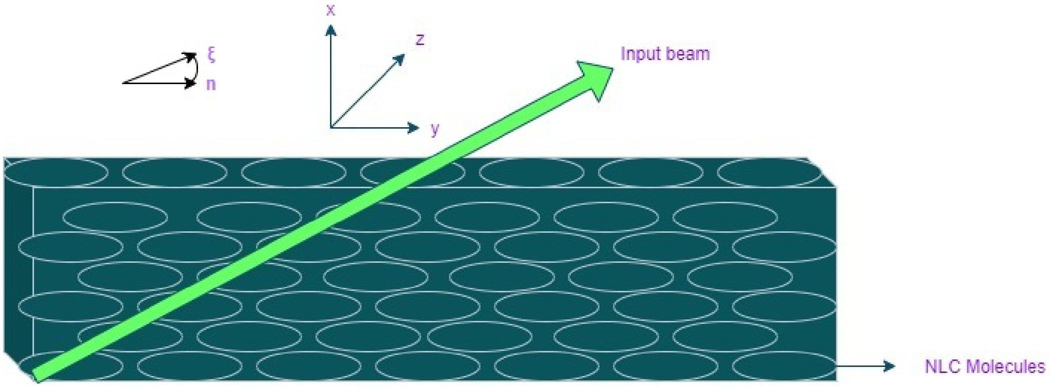

Figure 4.1: The interaction geometry. The elongated NLC is represented by a nematic liquid crystal with ellipses, having long axes parallel to y. The green arrow depicts the input light beam impinging normally to the molecular director on the sample. The angle ξ describes the reorientation of the optic axis, n in the (x, y) plane.

The x and y components of the electric fields are denoted as E_x and E_y respectively, and the director angle is ξ. z is the propagation distance. ϵ_a is the birefringence of the nematic, and k_0 is the ordinary wave vector. K stands for the elastic constant of the medium. The refractive indices parallel to the director alignment are $n_{\|}$ and perpendicular to it are $n_{\perp}$. The different constants in the model are taken from the material properties of the standard E7 mixture at room temperature, which is a positive uniaxial NLC with $n_{\|}$=1.73 and $n_{\perp}$=1.53, and elastic constant K=12pN [7]. The two-dimensional Laplacian is represented by $\nabla^2\xi$. $V(x, y)$ is the parabolic potential which is given by

$$V(x, y) = V_0(x^2 + y^2), \tag{4.4}$$

where V_0 is the strength of parabolic potential.

The equations describing the x and y components of the electric field of the beam are

$$E_x = Xe^{ik_0 n_{\perp} z}, \qquad E_y = Ye^{ik_0 n_{\|} z}. \tag{4.5}$$

The components of electric fields in two transverse directions are represented by

X and Y. By substituting Equation (4.5) in Equations (4.1) - (4.3), we obtain,

$$2i\frac{\partial X}{\partial z} + \frac{\partial^2 X}{\partial x^2} + \frac{\partial^2 X}{\partial y^2} + Xsin^2\xi + \frac{1}{2}Ye^{\frac{iz}{1+\gamma}}sin2\xi + V(x,y)X = 0, \tag{4.6}$$

$$2i\gamma\frac{\partial Y}{\partial z} + \frac{\partial^2 Y}{\partial x^2} + \gamma^2\frac{\partial^2 Y}{\partial y^2} - Ysin^2\xi + \frac{1}{2}Xe^{\frac{-iz}{1+\gamma}}sin2\xi - V(x,y)Y = 0, \tag{4.7}$$

$$\nu\nabla^2\xi + (|X|^2 - |Y|^2)sin2\xi + 2Re(XY^*e^{\frac{-iz}{1+\gamma}})cos2\xi = 0, \tag{4.8}$$

where,

$$\gamma = \frac{n_\parallel}{n_\perp}, \qquad \nu = \frac{4Kk_0^2}{\epsilon_0 A_b^2}. \tag{4.9}$$

Anisotropy and nonlocality are indicated in the above equation by the symbols γ and ν, respectively. A_b is the amplitude of the input optical beam.

The variational method has been used to analyze the Equations (4.6) – (4.8). The Lagrangian density of the system is obtained by

$$\begin{aligned} L = i(X^*X_z - XX_z^*) - |X_x|^2 - |X_y|^2 - i\gamma(Y^*Y_z - YY_z^*) - |Y_x|^2 - \gamma^2|Y_y|^2 \\ -\frac{1}{2}\nu|\nabla\xi|^2 + Re(XY^*e^{\frac{-iz}{1+\gamma}})sin2\xi + (|X|^2 - |Y|^2)sin^2\xi \\ +V(x,y)(|X|^2 - |Y|^2), \end{aligned} \tag{4.10}$$

where the asterisk stands for complex conjugation. The subscripts x,y, and z represent the partial derivatives with respect to x,y, and z respectively.
The trial solutions of the beam are selected as

$$X = (a_x e^{\frac{-r^2}{w_x^2}} + ig_x)e^{i\sigma_x}, \qquad Y = (a_y e^{\frac{-r^2}{w_y^2}} + ig_y)e^{i\sigma_y}, \tag{4.11}$$

where $r^2 = x^2 + y^2$. The amplitudes of the beam are a_x and a_y, widths are w_x and w_y, and the phases are σ_x and σ_y in the two transverse directions. In addition, the heights of the diffractive radiation in the x and y directions, respectively, are g_x and g_y.

Including both local and nonlocal contributions, the trial function for the director angle is [8]

$$\xi = \alpha e^{\frac{-r^2}{\beta^2}} + A\left[Ei\left(\frac{-r^2}{\beta^2}\right) - ln\left(\frac{r^2}{d^2}\right)\right]. \tag{4.12}$$

Here, the first term represents the local contribution, in which α represents the amplitude and β is the width of the director. The second and third terms represent the nonlocal contributions, the amplitude of which is denoted by A. The half of the thickness of the NLC cell is represented by d. Assuming L as the thickness of the NLC, d satisfies the equation $d = L/2$. Ei denotes the exponential integral function. The parameters a_x, a_y, w_x, w_y, σ_x, σ_y, g_x, g_y, A, and α are functions of z.

The trial functions in Equations (4.11) and (4.12) are substituted into the Lagrangian (4.10), which is then averaged by integrating x and y from $-\infty$ to $+\infty$. ie,

$$\mathcal{L} = \int_{-\infty}^{+\infty} L dx dy. \tag{4.13}$$

By using Equation (4.13) the averaged Lagrangian is given by

$$\begin{aligned}\frac{\mathcal{L}}{\pi} = {} & -(a_x^2 w_x^2 + 2l_x^2 g_x^2){\sigma_x}' + 2w_x^2 g_x {a_x}' + 4a_x w_x g_x {w_x}' - 2a_x w_x^2 {g_x}' - a_x^2 \\ & - \gamma(a_y^2 w_y^2 + 2l_y^2 g_y^2){\sigma_y}' + 2\gamma w_y^2 g_y {a_y}' + 4\gamma a_y w_y g_y {w_y}' - 2\gamma a_y w_y^2 {g_y}' \\ & - \frac{1}{2}(1+\gamma^2)a_y^2 + \frac{2}{D}\alpha a_x a_y w_x^2 w_y^2 \beta^2 \cos\theta - \frac{1}{2}\nu\alpha^2 \\ & + \frac{1}{2}\alpha^2\left[\frac{a_x^2 w_x^2 \beta^2}{\beta^2 + w_x^2} - \frac{a_y^2 w_y^2 \beta^2}{\beta^2 + w_y^2}\right] + 2A\left[\ln\left(\frac{\pi w_x^4}{4d^2}\right) - \ln\left(\frac{\pi w_y^4}{4d^2}\right)\right] \\ & + A^2\left[a_x^2 \ln\left(\frac{\pi w_x^6}{16d^4}\right) - a_y^2 \ln\left(\frac{\pi w_y^6}{16d^4}\right)\right] + \frac{V_0}{4}(a_x^2 w_x^4 + a_y^2 w_y^4),\end{aligned} \tag{4.14}$$

where $'$ represents derivative with respect to z.
Here, D and θ are given by,

$$D = \beta^2 w_x^2 + \beta^2 w_y^2 + w_x^2 w_y^2, \qquad \theta = \frac{z}{1+\gamma} - \sigma_x + \sigma_y. \tag{4.15}$$

The standard variational approach for the system is given by,

$$\frac{\partial \mathcal{L}}{\partial p_i} - \frac{d}{dz}\left(\frac{\partial \mathcal{L}}{\partial\, p_i'}\right) = 0, \tag{4.16}$$

where p_i corresponds to all parameters free to vary in the ansatz. In the ansatz used in Equations (4.11) and (4.12), $p_i(z) = a_x$, a_y, w_x, w_y, σ_x, σ_y, g_x, g_y, A, and α. The variational equations for the beam parameters are obtained,

$$\begin{aligned}\frac{dw_x}{dz} = -\frac{l_x^2 g_x}{a_x w_x^3} + \frac{2\alpha a_y w_x w_y^2 \beta^2 l_x^2 g_x}{a_x^2 D^2}(\beta^2 + w_x^2) cos\theta + \frac{\alpha a_y w_x w_y^2 \beta^2 sin\theta}{a_x D} \\ -\frac{4\alpha a_y w_y^2 \beta^2 l_x^2 g_x}{w_x a_x^2 D^2}(\beta^2 w_x^2 - \beta^2 w_y^2 + w_x^2 w_y^2) cos\theta,\end{aligned} \tag{4.17}$$

$$\begin{aligned}\frac{dw_y}{dz} = -\frac{l_y^2 g_y (1+\gamma^2)}{2\gamma a_y w_y^3} + \frac{2\alpha a_x w_x^2 w_y \beta^2 l_y^2 g_y}{a_y^2 \gamma D^2}(\beta^2 + w_y^2) cos\theta - \frac{\alpha a_x w_x^2 w_y \beta^2 sin\theta}{a_y \gamma D} \\ -\frac{4\alpha a_x w_x^2 \beta^2 l_y^2 g_y}{\gamma w_y a_y^2 D^2}(\beta^2 w_y^2 - \beta^2 w_x^2 + w_x^2 w_y^2) cos\theta,\end{aligned} \tag{4.18}$$

$$\begin{aligned}\frac{da_x}{dz} = \frac{8\alpha a_y w_y^2 \beta^2 l_x^2 g_x}{a_x w_x^2 D^2}(\beta^2 w_x^2 - \beta^2 w_y^2 + w_x^2 w_y^2) cos\theta - \frac{2\alpha a_y w_y^2 \beta^2 sin\theta}{D} \\ -\frac{2\alpha a_y w_y^2 \beta^2 l_x^2 g_x}{a_x D^2}(\beta^2 + w_x^2) cos\theta,\end{aligned} \tag{4.19}$$

$$\begin{aligned}\frac{da_y}{dz} = \frac{8\alpha a_x w_x^2 \beta^2 l_y^2 g_y}{\gamma a_y w_y^2 D^2}(\beta^2 w_y^2 - \beta^2 w_x^2 + w_x^2 w_y^2) cos\theta + \frac{2\alpha a_x w_x^2 \beta^2 sin\theta}{\gamma D} \\ -\frac{2\alpha a_x w_x^2 \beta^2 l_y^2 g_y}{\gamma a_y D^2}(\beta^2 + w_y^2) cos\theta,\end{aligned} \tag{4.20}$$

$$\begin{aligned}\frac{dg_x}{dz} = \frac{a_x}{2w_x^2} - \frac{2\alpha a_y w_y^2 \beta^2}{D^2}(\beta^2 w_x^2 - \beta^2 w_y^2 + w_x^2 w_y^2) cos\theta + \frac{2A}{a_x w_x^2} \\ +A^2 a_x \ln\left(\frac{\pi w_x^4}{16 d^4}\right) + \frac{V_0 a_x w_x^2}{8},\end{aligned} \tag{4.21}$$

$$\begin{aligned}\gamma\frac{dg_y}{dz} = \frac{(1+\gamma^2) a_y}{4w_y^2} - \frac{2\alpha a_x w_x^2 \beta^2}{D^2}(\beta^2 w_y^2 - \beta^2 w_x^2 + w_x^2 w_y^2) cos\theta + \frac{2A}{a_y w_y^2} \\ +A^2 a_y \ln\left(\frac{\pi w_y^4}{16 d^4}\right) + \frac{V_0 a_y w_y^2}{8},\end{aligned} \tag{4.22}$$

$$\frac{d\sigma_x}{dz} = -\frac{2}{w_x^2} + \frac{2\alpha a_y w_x^2 w_y^2 \beta^2}{a_x D^2}(\beta^2 + w_x^2)cos\theta - \frac{4A}{a_x^2 w_x^2} - A^2 \ln\left(\frac{\pi w_x^4}{16d^4}\right) + V_0 w_x^2, \tag{4.23}$$

$$\gamma\frac{d\sigma_y}{dz} = -\frac{1+\gamma^2}{w_y^2} + \frac{2\alpha a_x w_x^2 w_y^2 \beta^2}{a_y D^2}(\beta^2 + w_y^2)cos\theta - \frac{4A}{a_y^2 w_y^2} - A^2 \ln\left(\frac{\pi w_y^4}{16d^4}\right) + V_0 w_y^2. \tag{4.24}$$

And the algebraic equations are

$$A = \frac{-\ln\left(\frac{\pi w_x^4}{4d^2}\right) - \ln\left(\frac{\pi w_y^4}{4d^2}\right)}{a_x^2 \ln\left(\frac{\pi w_x^6}{16d^4}\right) - a_y^2 \ln\left(\frac{\pi w_y^6}{16d^4}\right)}, \qquad \alpha = \frac{2}{D}\frac{a_x a_y w_x^2 w_y^2 \beta^2 cos\theta}{\nu - \beta^2 \Delta}, \tag{4.25}$$

where $\Delta = \dfrac{a_x^2 w_x^2}{\beta^2 + w_x^2} - \dfrac{a_y^2 w_y^2}{\beta^2 + w_y^2}$, and β is determined by the thickness L of the NLC cell, given by $\beta = \dfrac{L}{2\ln 100}$.

The method results in first-order coupled ordinary differential Equations (4.17) - (4.24). These are the so-called modulation equations. The numerical solutions of these modulation equations are obtained by the standard fourth-order Runge Kutta method.

The finite difference method has been used to directly solve the system of coupled partial differential equations included in the governing Equations (4.6) - (4.8) numerically. In this method, a rectangular grid is imposed on the problem and the grid planes are spaced apart by Δz and Δr such that $z_k = k\Delta z$ and $r_n = n\Delta r$, respectively. By choosing $\frac{\Delta z}{\Delta r^2} \leq 0.5$, the stability requirement is met. An initial trial function was chosen as per the variational ansatz as given in Equations (4.11) and (4.12). The numerical results of Equations (4.6) - (4.8) are compared with the variational results.

4.3 Results and discussions

The analysis has been done to investigate the effect of parabolic potential on the nematicon. The initial conditions are chosen as a_{x0}=1.0, a_{y0}=1.4, w_{x0}=12, w_{y0}=12, σ_{x0}=0, σ_{y0}=0, g_{x0}=0, and g_{y0}=0. The evolutions of the beam in two transverse directions are studied for various parabolic potential strengths.

The plots presented in Figure (4.2) display the evolution of the beam in two transverse directions with the parabolic potential strength of $V_0 = 0.5$ V/μm. The periodic oscillatory nature of nematicon is revealed by the solutions of modulation equations which are plotted in Figures 4.2(a) and (b). The numerical analysis of Equations (4.6) - (4.8) using the finite difference method also gives the periodic oscillations of the nematicon as depicted in Figures 4.2(c) and (d). Additionally, Figures 4.2(a)-(d) illustrate that the wavelength of periodic oscillations is about 39 μm in both the x and y directions.

Figure (4.3) shows the evolutions of the amplitudes along two transverse directions in a parabolic potential strength of V_0=1.0 V/μm. By using numerical and variational methods, it is found that nematicons have a periodic oscillatory nature. The results of the variational analysis are shown in the first row. The second row displays the numerical results. Figures 4.3(a)-(d) show that oscillations have a wavelength of about 24 μm. In this case, oscillation wavelength decreases in comparison to the previous case.

From Figures (4.2) and (4.3), we found that the nematicon exists in a range of parabolic potential and the nematicon has an oscillatory (periodic) solution. The wavelength of oscillation decreases from 39 μm to 24 μm as the potential strength increases from 0.5 V/μm to 1.0 V/μm.

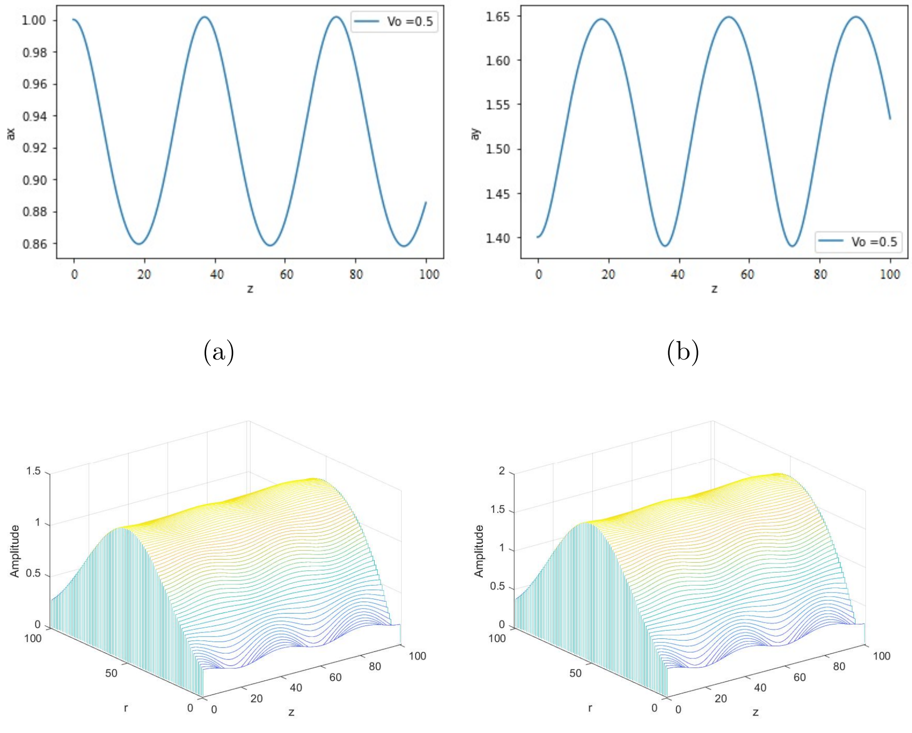

(a)
(b)
(c)
(d)

Figure 4.2: Evolution of beam in two transverse directions in a parabolic potential with a strength of $Vo = 0.5$ V/μm for an initial excitation with a_{x0}=1.0, a_{y0}=1.4, w_{x0}=12, w_{y0}=12, σ_{x0}=0, σ_{y0}=0, g_{x0}=0, g_{y0}=0. Upper row represents the amplitude variation along x and y directions from variational analysis and lower row represents the amplitude variation from numerical analysis.

The analysis has been done for various strengths of the potentials from 0.1 V/μm to 1.1 V/μm. The periodic oscillatory nature of the nematicon solution is revealed by both the variational and numerical results, and we found that the wavelength of oscillations decreases with increasing potential strength. Table (4.1) lists the potential strengths and their corresponding wavelengths of nematicon oscillation.

The linear relationship between wavelength and parabolic potential is shown in Figure (4.4). The variational results are shown in red solid line while the numerical results are shown in green dotted line. The wavelength of the periodic oscillations of the nematicon decreases linearly with increasing potential strength.

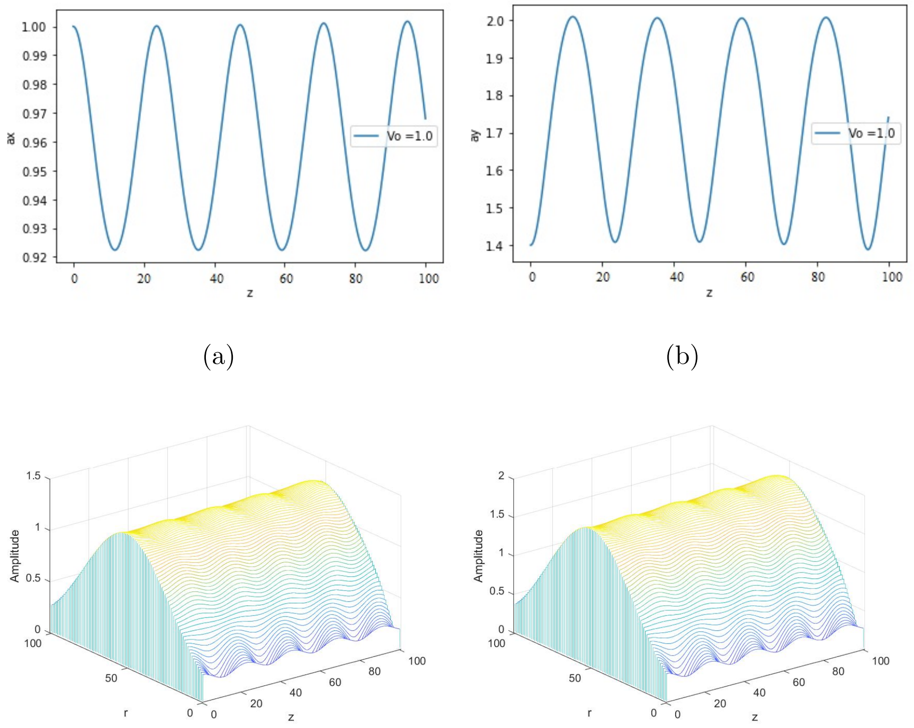

(a) (b)

(c) (d)

Figure 4.3: Evolution of beam in two transverse directions in a parabolic potential with a strength of $Vo = 1.0$ V/μm for an initial excitation with a_{x0}=1.0, a_{y0}=1.4, w_{x0}=12, w_{y0}=12, σ_{x0}=0, σ_{y0}=0, g_{x0}=0, g_{y0}=0. Upper row represents the amplitude variation along x and y directions from variational analysis and lower row represents the amplitude variation from numerical analysis.

Figure (4.5) depicts the evolution of width and phase in a parabolic potential. The modulation Equations (4.17) - (4.24) are solved semi-analytically, and the dynamics of the width and phases in a parabolic potential with a strength of $Vo = 0.5$ V/μm are presented in Figures 4.5(a)-(d). The first raw represents the variation of width along two transverse directions which shows it is periodic. The evolution of phase is shown in the second raw. When $Vo = 0.5$ V/μm, the phase exhibits the regular periodic behavior as shown in Figures 4.5(c) and (d). All of the parabolic potential strengths discussed above possess this regular periodic behavior of phase. So, all the potential strengths listed in Table (4.1) satisfy the phase-matching requirements for the generation of higher harmonics.

Potential strength (V/μm)	Wavelength (μm)
0.1	54
0.5	39
0.8	31
1.0	24
1.1	16

Table 4.1: The strength of parabolic potential and the corresponding wavelength of periodic oscillations of higher harmonics of nematicons.

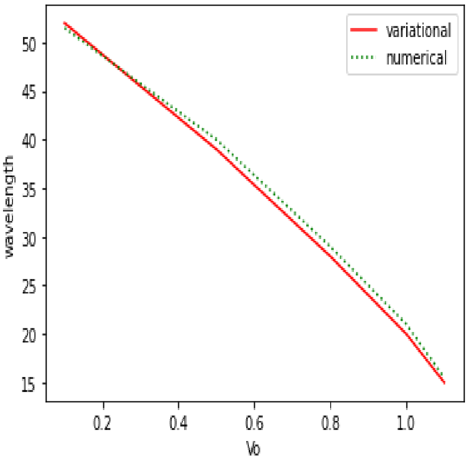

Figure 4.4: Wavelength (μm) of periodic oscillations versus parabolic potential (V/μm). Variational results: Red (solid) line, Numerical results: Green (dotted) line.

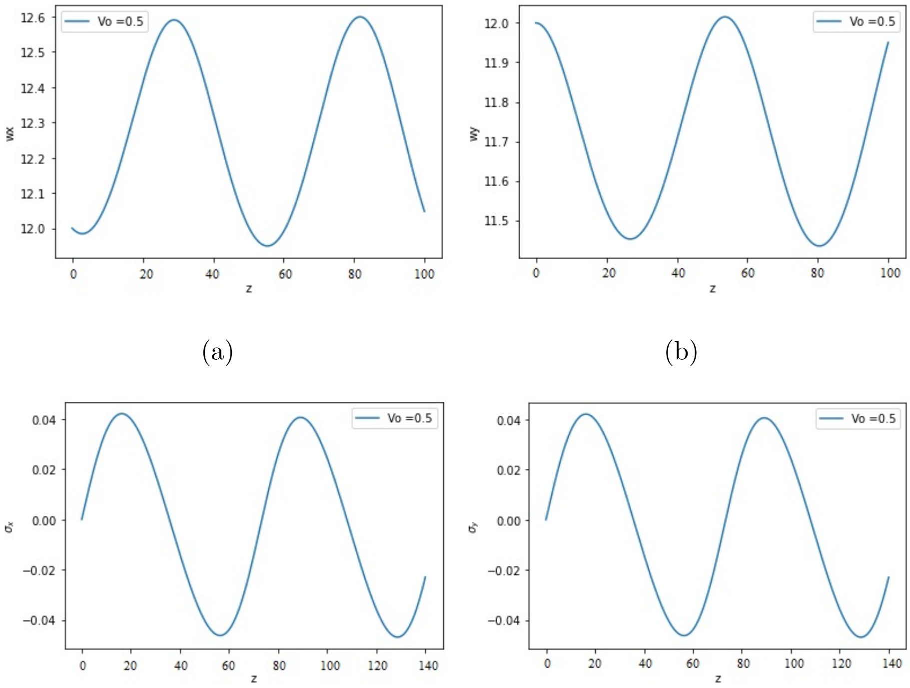

(a) (b)

(c) (d)

Figure 4.5: Evolutions of width and phase in two transverse directions in a parabolic potential with a strength of $Vo = 0.5$ V/μm for an initial excitation with a_{x0}=1.0, a_{y0}=1.4, w_{x0}=12, w_{y0}=12, σ_{x0}=0, σ_{y0}=0, g_{x0}=0, g_{y0}=0.

The fundamental frequency of the nematicon can be obtained using the parameter ν, the nonlocality given in Equation (4.9). The square of the fundamental frequency is proportional to nonlocality, and the fundamental frequency of nematicon is 0.13 THz, corresponding to a wavelength of 8.0 μm. So, by varying the strength of the parabolic potential, higher harmonics of nematicons can be generated whose wavelengths are multiples of 8.0 μm as shown in Table (4.1). When the strength of the parabolic potential is 1.1 V/μm, we get the second harmonic with a wavelength of 16 μm. The third, fourth, and higher harmonics are obtained by varying the strength of the parabolic potential by 1.0 V/μm, 0.8 V/μm, 0.5 V/μm, and 0.1 V/μm. As illustrated above, higher harmonics of nematicons can be generated by tuning the strength of parabolic potential.

This work has been analyzed the generation of higher harmonics of nematicons in an NLC with parabolic potential. The parabolic potential can be created experimentally in NLC by doping it with a suitable dopant such as dye, carbon nanotubes (CNTs), or nanoparticles [4, 9, 10].

4.4 Linear stability analysis

The solutions of the system has been studied in terms of the propagation constant μ:

$$P = Xexp(-i\mu z), \qquad Q = Yexp(-i\mu z). \tag{4.26}$$

The substitution of P and Q in Equations (4.6) and (4.7) give eigenvalue problem:

$$2i\frac{\partial P}{\partial z} + \frac{\partial^2 P}{\partial x^2} + \frac{\partial^2 P}{\partial y^2} + Psin^2\xi + \frac{1}{2}Qe^{\frac{iz}{1+\gamma}}sin2\xi + V(x,y)P = -2\mu P, \tag{4.27}$$

$$\begin{aligned} 2i\gamma\frac{\partial Q}{\partial z} + \frac{\partial^2 Q}{\partial x^2} + \gamma^2\frac{\partial^2 Q}{\partial y^2} - Qsin^2\xi + \frac{1}{2}Pe^{\frac{-iz}{1+\gamma}}sin2\xi \\ -V(x,y)Q = -2\mu\gamma Q. \end{aligned} \tag{4.28}$$

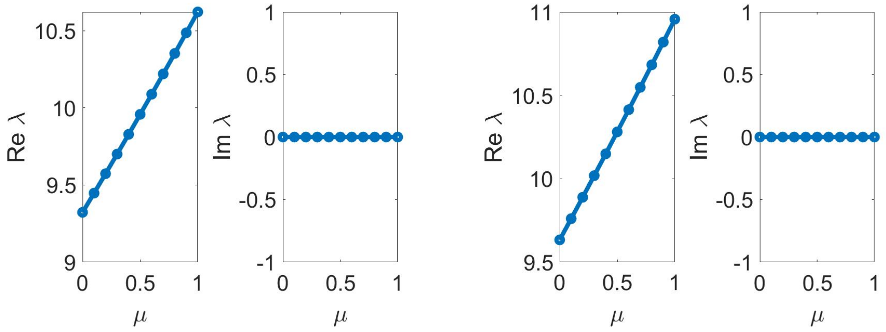

(a) (b)

Figure 4.6: The results of linear stability analysis of the system in a parabolic potential with the strength of (a) $V_0 = 0.5$ V/μm and (b) $V_0 = 1.0$ V/μm. The real and imaginary parts of the perturbation eigenvalues (λ) versus the propagation constant μ are shown.

Using Bogoliubov-De Genes (BDG) equations, the linear stability of the stationary states of the coupled system has been investigated. Consider small perturbations of the stationary states of the system as:

$$R = P + a(r,z)exp(-i\mu z), \qquad S = Q + b(r,z)exp(-i\mu z), \tag{4.29}$$

where,

$$a(r,z) = a_1(r)exp(i\lambda z) + a_2(r)exp(-i\lambda^* z), \tag{4.30}$$

$$b(r,z) = b_1(r)exp(i\lambda z) + b_2(r)exp(-i\lambda^* z), \tag{4.31}$$

where the asterisk denotes the complex conjugation. Assuming a_1, a_2, b_1, and b_2 are very small, the pair of coupled Equations (4.27) and (4.28) are linearized after being transformed into radial coordinates. This leads to a set of four homogeneous equations that are fulfilled by a_1, a_2, b_1, and b_2, and are shown in matrix form as follows:

$$\lambda \begin{pmatrix} a_1 \\ a_2^* \\ b_1 \\ b_2^* \end{pmatrix} = C \begin{pmatrix} a_1 \\ a_2^* \\ b_1 \\ b_2^* \end{pmatrix}, \tag{4.32}$$

where,

$$C = \begin{pmatrix} L_1 + V(r) & 0 & \frac{1}{4}e^{\frac{iz}{1+\gamma}} sin2\xi & 0 \\ 0 & -L_1 - V(r) & 0 & -\frac{1}{4}e^{\frac{-iz}{1+\gamma}} sin2\xi \\ \frac{1}{4\gamma}e^{\frac{-iz}{1+\gamma}} sin2\xi & 0 & L_2 + V(r) & 0 \\ 0 & -\frac{1}{4\gamma}e^{\frac{iz}{1+\gamma}} sin2\xi & 0 & -L_2 - V(r) \end{pmatrix}, \tag{4.33}$$

where,

$$L_1 = \frac{1}{2}\left(\frac{d^2}{dr^2} + \frac{1}{r}\frac{d}{dr} + sin^2\xi + 2\mu\right), \tag{4.34}$$

$$L_2 = \frac{1}{2\gamma}\left(\frac{d^2}{dr^2} + \frac{1}{r}\frac{d}{dr} - sin^2\xi + 2\gamma\mu\right). \tag{4.35}$$

To solve the system, spectral methods based on Chebyshev polynomials are employed. To evaluate the diffraction operators, a grid is chosen that extends 40 along r [11, 12].

The perturbation eigenvalues as functions of the propagation constants have been studied. The stability of the solution is determined by the type of eigenvalue. For real values of λ, the solution is stable. The oscillatory instability of the solution is brought on by the complex values of λ. Figure (4.6) consists of stability plots for two different strengths of parabolic potential. Figures 4.6(a) and (b) illustrate that solutions are stable with purely real eigenvalues.

4.5 Conclusion

The influence of a parabolic potential on a uniaxial nematic liquid crystal with nonlocal nonlinearity is investigated through semi-analytical and numerical methods. In such a potential, the nematicon exhibits periodic oscillatory behavior. As the potential strength increases, the oscillation wavelength shortens linearly. Adjusting the potential's strength can lead to the generation of higher harmonics of nematicons. Linear stability analysis shows that nematicons are stable when subjected to a parabolic potential.

The findings of this study have significant practical implications in optical communications and photonics. The controlled generation and manipulation of nematicons within a parabolic potential environment can benefit optical signal processing. By adjusting the potential strength, engineers can produce various oscillation patterns and wavelengths, offering the potential for tunable optical devices. As the wavelength decreases with increased potential strength, the propagation of light can be precisely controlled, which is useful for designing adaptable optical waveguides in photonic systems. The ability to generate higher harmonics of nematicons by modifying the parabolic potential opens new avenues in nonlinear optics. These harmonics could be leveraged for frequency conversion or for producing light with tailored properties for advanced communication technologies. Additionally, such harmonic generation offers opportunities for developing sophisticated nonlinear optical devices, applicable in fields like imaging and laser technology, where precise light control is essential. Furthermore, stability analysis using the Bogoliubov-De Gennes equations extends its relevance to photonic systems. Gaining insight into the conditions for nematicon stability against perturbations aids in designing durable photonic circuits, a key component for future innovations in quantum computing and signal processing.

The next chapter extends the study of nematicons in a parabolic potential by exploring how thermal effects influence beam propagation.

Bibliography

[1] ichi Kosugi J, Kajikawa K. Phase-matched third-harmonic generation from nematic liquid crystals. Applied Physics Letters. 2004 jun;84(24):5013-5.

[2] Wang G. Third-harmonic generation in cylindrical parabolic quantum wires with an applied electric field. Physical Review B. 2005 Oct;72(15):155329.

[3] Assanto G, Minzoni AA, Smyth NF, Worthy AL. Refraction of nonlinear beams by localized refractive index changes in nematic liquid crystals. Physical Review A. 2010 nov;82(5):053843.

[4] Smyth NF, Assanto G, Skuse BD. Optical path control of solitary waves in dye-doped nematic liquid crystals. Photonics Letters of Poland. 2009 dec;1(4).

[5] Trashkeev SI, Vasenin NT, Vatnik SM, Vedin IA, Ivanenko AV, Klementyev VM. Harmonic generation in a nematic liquid crystal. Laser Physics Letters. 2020 jun;17(7):075002.

[6] Nyushkov BN, Trashkeev SI, Klementyev VM, Pivtsov VS, Kobtsev SM. Generation of harmonics and supercontinuum in nematic liquid crystals. Quantum Electronics. 2013 feb;43(2):107-13.

[7] Assanto G, Smyth NF. Spin-optical solitons in liquid crystals. Physical Review A. 2020 sep;102(3):033501.

[8] Aleksić NB, Petrović MS, Strinić AI, Belić MR. Solitons in highly nonlocal

nematic liquid crystals: Variational approach. Physical Review A. 2012 mar;85(3):033826.

[9] Lin FC, Wu PC, Jian BR, Lee W. Dopant Effect and Cell-Configuration-Dependent Dielectric Properties of Nematic Liquid Crystals. Advances in Condensed Matter Physics. 2013;2013:1-5.

[10] Urbanski M. On the impact of nanoparticle doping on the electro-optic response of nematic hosts. Liquid Crystals Today. 2015 sep;24(4):102-15.

[11] Suneera TP, Subha PA. Higher eigenmodes of nonlocal gap solitons in parity-time symmetric complex potential with a defocusing nonlinearity. Chaos, Solitons &amp Fractals. 2017 may;98:183-8.

[12] Suneera TP, Subha PA. Nonlocal gap solitons in parity-time symmetric coupler with transverse real potential. Journal of Optics. 2018 aug;20(9):095504.

Chapter 5

Thermal Effects on Nematicons in Parabolic Potential

In this chapter, the thermal behavior of nematicons in a parabolic potential is studied numerically. Single-peak nematicons can occur in the absence of thermal response coefficients where focusing reorientational nonlinearity dominates. When thermal response is present, the competition between focusing reorientational and defocusing thermal nonlinearities causes single-peak nematicons to transform into double-peak ones. The energy landscape modified by these nonlinearities stabilizes double-peak nematicons as equilibrium states. For small thermal response coefficients, double-peak nematicons exhibit periodic oscillations with the oscillation wavelength increasing as the thermal response coefficient rises. The oscillations of the double-peak nematicon are lost at large thermal response coefficients. Stability analysis shows that single-peak and oscillating double-peak nematicons are stable, while non-oscillating double-peak nematicons are unstable. This study is pivotal, as the ability to manipulate nematicons using both thermal and reorientational nonlinearities can greatly benefit advanced photonic devices.

The results of this chapter are published as:

- N. M. Sajitha, T. P. Suneera, ‘Thermal response of nematicons in a parabolic potential’. Physica Scripta. 2024 May; 99(6): 065567.

5.1 Introduction

In recent years, liquid crystals have emerged as an excellent material platform for investigating solitons and their interactions [1–4]. In their ordered phases, like the nematic phase, liquid crystals exhibit high birefringence, and their dielectric properties can be modulated by external fields or light through a nonlinear response [5]. This response is often governed by thermo-optic or reorientational processes [6]. The thermal effects resemble those found in other dielectric materials when absorption occurs while the reorientational response is characteristic of liquid crystals that possess a certain degree of orientational order [7].

When an electromagnetic wave passes through a doped NLC, it experiences a disturbance that manifests as a parabolic potential in the medium [8, 9]. Experimentally, this parabolic potential can be generated by introducing dopants like dyes, carbon nanotubes (CNTs), or nanoparticles into the NLC [9–11]. In many nonlinear optical systems, including NLCs, the nonlinear response of the medium is a nonlocal function of wave intensity, meaning that the refractive index at a certain location is influenced by the light intensity in the surrounding region [12]. Examples of nonlocal responses in optics include the thermo-optic effect, where absorbed light heats a material and influences its optical properties at distant points, and the reorientational nonlinearity in liquid crystals where elastic interactions spread the impact of local electromagnetic disturbances [13–15]. The unique optical properties of nematic liquid crystals allow both reorientational and thermal solitons to coexist, and their interaction can either enhance or diminish the overall nonlinear response [14]. At high optical powers, the interaction between focusing reorientational and defocusing thermal nonlinearities can give rise to one and two dimensional multihumped solitary waves as well as ring shaped waves with a volcano like profile in the plane perpendicular to the direction of propagation [16].

The motivation behind the chapter stems from a desire to understand the thermal behavior of nematicons within a parabolic potential. Nematicons are primarily influenced by reorientational nonlinearity where light induced molecular reorientation causes a focusing effect. However, when thermal responses are introduced, the competition between focusing reorientational nonlinearity and defocusing thermal nonlinearity becomes significant.

The chapter focuses on how this competition affects the characteristics of nematicons, particularly the transformation of single-peak nematicons into double-peak structures as a result of significant defocusing thermal nonlineraity. By analyzing the impact of thermal response coefficients on the stability and oscillatory patterns of these light beams, the study aims to reveal the energy dynamics and mechanisms that contribute to stabilization. Gaining insights into these interactions is vital for improving the control and manipulation of light in photonic devices, where the ability to adjust and stabilize light propagation is crucial for various applications, including optical communications, signal processing, and nonlinear optics.

This chapter investigates the thermal response of nematicons in a parabolic potential in the nonlocal regime. Beam dynamics have been studied for various thermal response coefficients. The chapter is organized as follows. Section 5.2 discusses the theoretical model of the system. The governing equations of the system are numerically solved using the finite difference method. Section 5.3 presents the results and discussions. The stability of the solution under small perturbation has been studied using linear stability analysis in section 5.4. Section 5.5 concludes the chapter.

5.2 Theoretical model

Take into consideration an optical beam traveling in the z-direction through a positive uniaxial NLC. Figure (5.1) displays the geometry of the NLC cell. The optic axis of the nematic is aligned along the y-axis, and its reorientation in the xy plane is indicated by the angle ξ. NLCs can be created with parabolic refractive index variations by adding dopants or applying some external excitations. So we can model the system by a nonlinear Schrodinger-type equation with a parabolic potential for the optical beam and an elliptic Poisson equation for the molecular director.

The governing equations of the system are given by

$$2ik_0 n_\perp \frac{\partial E_x}{\partial z} + \frac{\partial^2 E_x}{\partial x^2} + \frac{\partial^2 E_x}{\partial y^2} + k_o^2 \epsilon_a E_x sin^2\xi + \frac{1}{2} k_0^2 \epsilon_a E_y e^{ik_0(n_\parallel - n_\perp)z} sin 2\xi \\ + V(x,y) E_x = 0, \tag{5.1}$$

$$2ik_0 n_\parallel \frac{\partial E_y}{\partial z} + \frac{\partial^2 E_y}{\partial x^2} + \frac{n_\parallel^2}{n_\perp^2} \frac{\partial^2 E_y}{\partial y^2} - k_o^2 \epsilon_a E_y sin^2\xi + \frac{1}{2} k_0^2 \epsilon_a E_x e^{-ik_0(n_\parallel - n_\perp)z} sin 2\xi \\ - V(x,y) E_y = 0, \tag{5.2}$$

$$K\nabla^2\xi + \frac{1}{4}\epsilon_0 \epsilon_a \left[2(\mid E_x \mid^2 - \mid E_y \mid^2) sin 2\xi + 2Re E_x E_y^* e^{-ik_0(n_\parallel - n_\perp)z} cos 2\xi \right] = 0. \tag{5.3}$$

E_x and E_y denote the x and y components of the electric fields, respectively. The symbol ξ represents the director angle, and z represents the propagation distance. The ordinary wave vector is denoted by k_0, while the nematic birefringence is denoted by ϵ_a. $n_\parallel$ and $n_\perp$ denote the refractive indices parallel and perpendicular to the director alignment, respectively. ∇^2 represents the two-dimensional Laplacian. K specifies the elastic constant of the medium, which is considered to be the same for bend, splay, and twist deformations of the NLC molecules. $V(x,y)$ is the parabolic potential which is given by

$$V(x,y) = V_0(x^2 + y^2), \tag{5.4}$$

where V_0 is the strength of parabolic potential. The thermo-optic changes in the optical properties of the NLC are produced by localized heating caused by light absorption as the beam moves through the medium. The refractive indices $n_\parallel$, $n_\perp$ and the elastic constant K of the medium are temperature dependent when thermal effects on material properties are included.

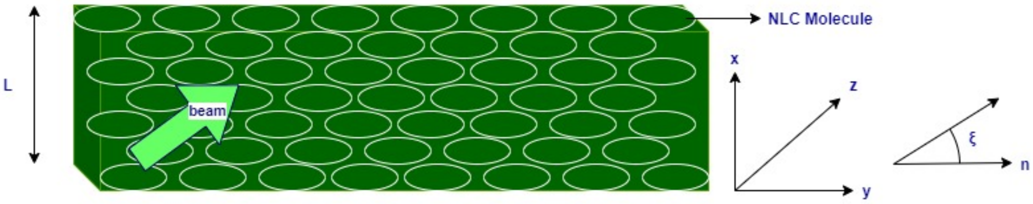

Figure 5.1: The interaction geometry. The elongated NLC is represented as a nematic liquid crystal with ellipses with long axes parallel to y. The input light beam is depicted with a green arrow impinging normally on the molecular director. The angle ξ indicates the reorientation of the optic axis, n in the (x, y) plane.

The heat equation governs heat flow in the NLC and can be expressed as [17]

$$S\nabla^2 T = -\alpha\Gamma \mid E \mid^2, \qquad \text{where,} \quad \Gamma = \frac{1}{2}\epsilon_0 c n_e. \tag{5.5}$$

Thermal conductivity is denoted by the letter S and α stands for the thermal absorption coefficient of the material. T is the temperature, ϵ_0 is the permittivity of free space, and c is the speed of light. The refractive index of the extraordinary polarized waves, denoted by n_e, is given by

$$n_e^2 = \frac{n_\parallel^2 n_\perp^2}{n_\parallel^2 cos^2\xi + n_\perp^2 sin^2\xi}. \tag{5.6}$$

Let T_0 represent the NLC temperature in the absence of the beam, and A_T denote the typical temperature increase caused by optical heating. Then $T = T_0 + A_T\tau$, where τ represents the nondimensional temperature change from T_0. The heat equation in nondimensional form is given as

$$\mu_T \nabla^2 \tau = - \mid X \mid^2 - \mid Y \mid^2, \qquad \text{where,} \quad \mu_T = \frac{S A_T}{\alpha\Gamma W_b^2 A_b^2}, \tag{5.7}$$

where μ_T is the nondimensional thermal diffusivity [16]. A_b and W_b are the amplitude and width of the input wave packet. The equations of the x and y

components of the electric field of the beam are

$$E_x = Xe^{ik_0 n_\perp z}, \qquad E_y = Ye^{ik_0 n_\parallel z}. \tag{5.8}$$

The amplitudes of electric fields in two transverse directions are represented by X and Y. When the equations for E_x and E_y from Equation (5.8) are substituted into Equations (5.1)-(5.3) and the thermal effect on material parameters is taken into consideration, as well as nondimensionalizing Equations (5.1)-(5.3), we get

$$2i\frac{\partial X}{\partial z} + \frac{\partial^2 X}{\partial x^2} + \frac{\partial^2 X}{\partial y^2} + Xsin^2\xi + \frac{1}{2}Ye^{\frac{iz}{1+\gamma(\tau)}}sin2\xi + V(x,y)X = 0, \tag{5.9}$$

$$\begin{aligned} 2i\gamma(\tau)\frac{\partial Y}{\partial z} + \frac{\partial^2 Y}{\partial x^2} + \gamma(\tau)^2\frac{\partial^2 Y}{\partial y^2} - Ysin^2\xi + \frac{1}{2}Xe^{\frac{-iz}{1+\gamma(\tau)}}sin2\xi \\ -V(x,y)Y = 0, \end{aligned} \tag{5.10}$$

$$\nu(\tau)\nabla^2\xi + (\mid X \mid^2 - \mid Y \mid^2)sin2\xi + 2Re(XY^*e^{\frac{-iz}{1+\gamma(\tau)}})cos2\xi = 0. \tag{5.11}$$

Both the nonlocality (ν) and the anisotropy (γ) depend on temperature. The following equations connect them to the elastic constant K and the extra-ordinary refractive index n_e [17],

$$\nu = \frac{8K}{\epsilon_0\epsilon_a A_b^2 W_b^2 sin2\xi}, \quad \gamma = \frac{2n_e}{\sqrt{\epsilon_a sin2\xi}}. \tag{5.12}$$

According to experimental data, the refractive index eigenvalues for the standard NLC mixture E7 vary nearly linearly with temperature up to about 40^0C [17]. Between 20 and 40 degrees Celsius, the refractive index $n_\parallel$ decreases by approximately 0.6% whereas the refractive index $n_\perp$ increases by approximately 1.3% [7, 17]. As a result, $\gamma(\tau)$ can be expanded to second order in a Taylor series as $\gamma(\tau) = 1 - \gamma_1\tau$, where γ_1 is related to $\frac{d\gamma}{d\tau}$ at $T = T_0$. The dependence of temperature on elastic constant, K is minimal [18]. Therefore, it will be ignored in our discussions.

The finite difference method has been employed to obtain numerical solutions to the system of Equations (5.9)-(5.11). A rectangular grid is imposed on the problem, and the grid planes are separated by Δz and Δr, respectively, so that $z_k = k\Delta z$ and $r_n = n\Delta r$. The stability condition is met by using $\frac{\Delta z}{\Delta r^2} \leq 0.5$. The solutions to Equations (5.9) and (5.10) are chosen as [16],

$$X = a_x \left[e^{\frac{-(r-m)^2}{w_x^2}} + e^{\frac{-(r+m)^2}{w_x^2}} \right] e^{i\sigma_x}, \qquad Y = a_y \left[e^{\frac{-(r-m)^2}{w_y^2}} + e^{\frac{-(r+m)^2}{w_y^2}} \right] e^{i\sigma_y}, \tag{5.13}$$

where $r^2 = x^2 + y^2$. The beam amplitudes are a_x and a_y, the widths are w_x and w_y, and the phases are σ_x and σ_y in the two transverse directions.
The solution of Equation (5.11) is chosen as [19],

$$\xi = \alpha e^{\frac{-r^2}{\beta^2}} + A \left[Ei\left(\frac{-r^2}{\beta^2} \right) - ln\left(\frac{r^2}{d^2} \right) \right]. \tag{5.14}$$

In Equation (5.14), the first term stands for the local contribution with the amplitude α, while the second and third terms represent the nonlocal contributions having amplitude A and width β. α depends on the propagation distance z through the relation [20],

$$\alpha = \frac{2}{D} \frac{a_x a_y w_x^2 w_y^2 \beta^2 cos\theta}{\nu - \beta^2 \Delta}, \tag{5.15}$$

where,

$$D = \beta^2 w_x^2 + \beta^2 w_y^2 + w_x^2 w_y^2, \quad \theta = \frac{z}{1+\gamma} - \sigma_x + \sigma_y, \quad \Delta = \frac{a_x^2 w_x^2}{\beta^2 + w_x^2} - \frac{a_y^2 w_y^2}{\beta^2 + w_y^2}. \tag{5.16}$$

β is given by the relation, $\beta = L/(2\ln 100)$. Assuming L is the thickness of the NLC, $d = L/2$. Ei denotes the exponential integral function.

$$E_i = -\int_{-z}^{+\infty} e^{-t} t^{-1} dt. \tag{5.17}$$

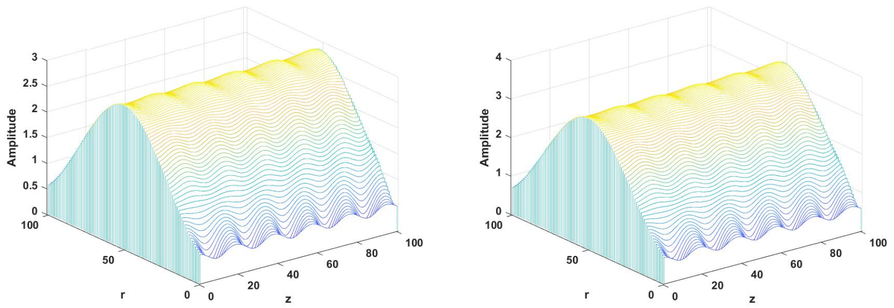

(a) (b)

Figure 5.2: Evolution of the amplitude in two transverse directions for $\tau_0 = \tau_1 = 0$: (a) Along the x-direction, and (b) along the y-direction.

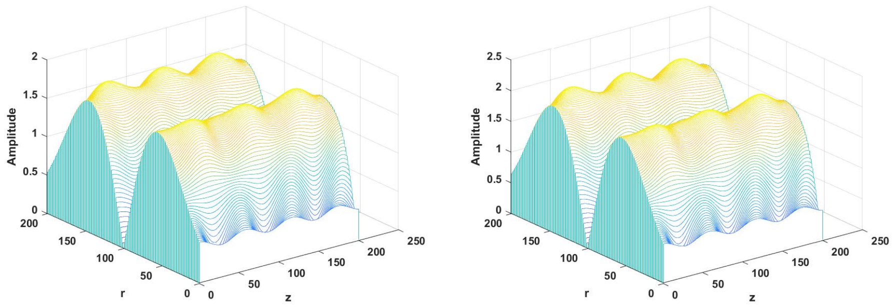

(a) (b)

Figure 5.3: Evolution of the amplitude in two transverse directions for $\tau_0 = \tau_1 = 0.8$: (a) Along the x-direction, and (b) along the y-direction.

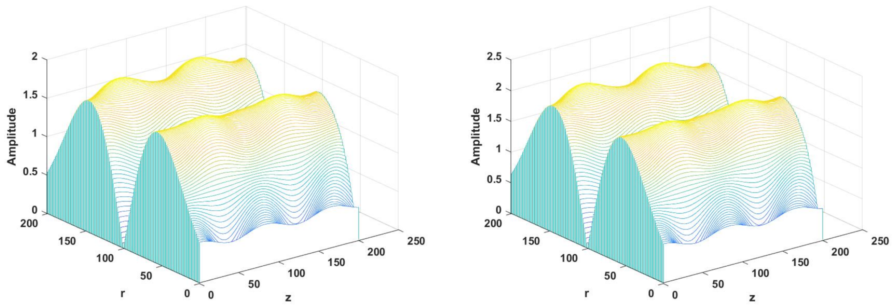

(a) (b)

Figure 5.4: Evolution of the amplitude in two transverse directions for $\tau_0 = \tau_1 = 1.4$: (a) Along the x-direction, and (b) along the y-direction.

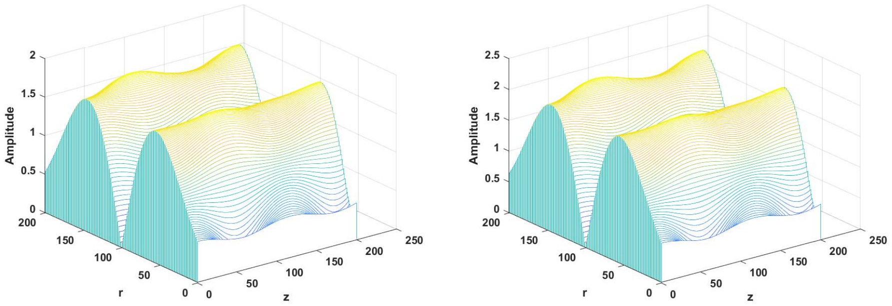

(a) (b)

Figure 5.5: Evolution of the amplitude in two transverse directions for $\tau_0 = \tau_1 = 2.0$: (a) Along the x-direction, and (b) along the y-direction.

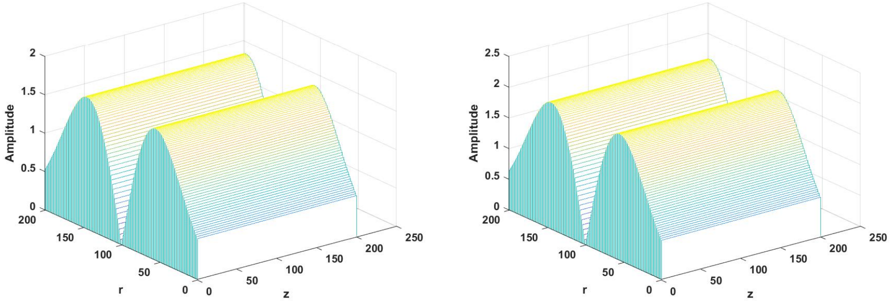

(a) (b)

Figure 5.6: Evolution of the amplitude in two transverse directions for $\tau_0 = \tau_1 = 2.4$: (a) Along the x-direction, and (b) along the y-direction.

There are two homogeneous solutions $\ln r$ and a constant for the radially symmetric heat Equation (5.7). Due to the high thermal diffusivity μ_T, we assume that the temperature within the circular peak of nematicon is constant. The temperature decays as the homogeneous solution moves away from the axis [16].

$$\tau = \tau_0, \quad 0 \leq r \leq m; \qquad \tau = \tau_1 \ln \frac{R}{r}, \quad m < r < R. \tag{5.18}$$

Also, it follows the boundary condition $\tau = 0$ at $r = R$.

The thermal response of the system has been studied numerically in section 5.3.

5.3 Results and discussions

The analysis has been done to investigate the thermal response of nematicons in a parabolic potential employing the finite difference method. The strength of the potential is taken as $V_0 = 1.2$ V/μm throughout the analysis. The initial conditions are a_{x0}=2.0, a_{y0}=2.4, w_{x0}=12, w_{y0}=12, σ_{x0}=0, and σ_{y0}=0. The different parameters are chosen as $\mu_T = 300$, $\nu = 600$, $\gamma_1 = 0.1$, $\alpha = 2$, $A = 0.5$, and $m = 2.2$.

Figure (5.2) depicts the evolution of the beam in two transverse directions in the absence of thermal response coefficients. In the absence of thermal response, nonlinearity is mainly driven by molecular reorientation, and the nematicons exhibit a single-peak shape. Single-peak nematicons with periodic oscillation have been obtained in a parabolic potential as shown in Figures 5.2(a) and (b).

When the thermal response coefficients are $\tau_0 = \tau_1 = 0.8$, the evolutions of the beam along two transverse directions are depicted in Figure (5.3). In the presence of thermal response, the competition between focusing reorientational and defocusing thermal nonlinearities results in the transition of single-peak to double-peak nematicons. In this region, the defocusing thermal nonlinearity exceeds the focusing reorientational nonlinearity, causing the output beam profile to split and transform into double-peak nematicons. The double-peak nematicons are obtained and they exhibit periodic oscillation in a parabolic potential. Figures 5.3(a) and (b) show that the wavelength of periodic oscillations is around 56 μm in both x and y directions. Figure (5.4) depicts the propagation of amplitudes in two transverse directions for the thermal response coefficients $\tau_0 = \tau_1 = 1.4$. Figures 5.4(a) and (b) indicate that oscillations have a wavelength of around 79 μm. The oscillation wavelength is longer than in the prior case.

The advancement of amplitudes in x and y directions for the thermal response coefficients $\tau_0 = \tau_1 = 2.0$ is depicted in Figure (5.5). Figures 5.5(a) and (b) show that double-peak nematicons with periodic oscillations have a wavelength of about 115 μm. The wavelength of the oscillation increases as the thermal response coefficients increase.

Thermal response coefficients	Wavelength
0.2	44
0.4	47
0.6	51
0.8	56
1.0	62
1.2	70
1.4	79
1.6	90
1.8	102
2.0	115

Table 5.1: Thermal response coefficients and the corresponding wavelength (μm) of periodic oscillations of double-peak nematicon.

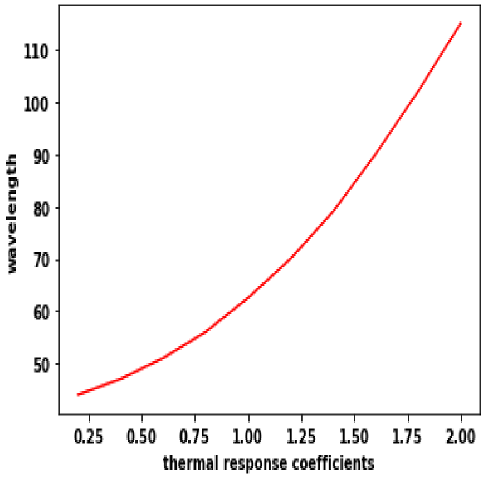

Figure 5.7: The thermal response coefficients versus wavelength (μm) of periodic oscillations.

The analysis has been carried out for thermal response coefficients ranging from 0.2 to 2.0 in a parabolic potential strength of $V_0 = 1.2$ V/μm. The periodic oscillatory nature of the nematicon solution is revealed by numerical methods, and we found that the wavelength of oscillations increases with increasing thermal response coefficients.

For relatively large values of thermal response coefficients, double-peak nematicons lose oscillations as shown in Figure (5.6) which is plotted for $\tau_0 = \tau_1 = 2.4$. Table (5.1) shows the thermal response coefficients and related wavelengths of nematicon oscillation in a parabolic potential strength of $V_0 = 1.2$ V/μm. The relationship between wavelength and thermal response coefficients is depicted in Figure (5.7). The wavelength of the periodic oscillations of the nematicon increases with increasing thermal response coefficients.

Figures (5.3)-(5.6) show the double-peak nematicons because the competing nonlinearities modify the energy landscape experienced by the light beam within the medium. The presence of both focusing reorientational and defocusing thermal nonlinearities creates multiple maxima in the energy landscape, allowing for the stabilization of double-peak nematicons as equilibrium states. The double-peak nematicons might indicate a bistable behavior in the medium, where the optical energy can be stably localized in two different spatial regions.

From the above results, it is clear that the competition between focusing reorientational and defocusing thermal nonlinearities leads to the formation of single-peak and double-peak nematicons. Single-peak nematicons have been found only in the absence of thermal response coefficients and exhibit periodic oscillations in a parabolic potential. Double-peak nematicons can exist in the presence of thermal response coefficients because the defocusing thermal nonlinearity exceeds the focusing reorientational nonlinearity. When the defocusing thermal nonlinearity exceeds the focusing reorientational nonlinearity, the equilibrium state is achieved through the redistribution of energy to the double-peak structure. Double-peak nematicons also exhibit periodic oscillations in a parabolic potential. With increasing thermal response coefficients, the wavelength of periodic oscillations increases. However, even in a parabolic potential, the oscillatory nature of nematicons is lost when thermal response coefficients are sufficiently high.

5.4 Linear stability analysis

The solutions of the system have been studied in terms of the propagation constant μ:

$$P \quad = Xexp(-i\mu z), \qquad Q \quad = Yexp(-i\mu z). \tag{5.19}$$

The substitution of P and Q in Equations (5.9) and (5.10) give eigenvalue problem:

$$\begin{aligned}2i\frac{\partial P}{\partial z} + \frac{\partial^2 P}{\partial x^2} + \frac{\partial^2 P}{\partial y^2} + Psin^2\xi + \frac{1}{2}Qe^{\frac{iz}{1+\gamma(\tau)}}sin2\xi \\ +V(x,y)P = -2\mu P,\end{aligned} \tag{5.20}$$

$$\begin{aligned}2i\gamma(\tau)\frac{\partial Q}{\partial z} + \frac{\partial^2 Q}{\partial x^2} + \gamma(\tau)^2\frac{\partial^2 Q}{\partial y^2} - Qsin^2\xi + \frac{1}{2}Pe^{\frac{-iz}{1+\gamma(\tau)}}sin2\xi \\ -V(x,y)Q = -2\mu\gamma Q.\end{aligned} \tag{5.21}$$

Bogoliubov-de Gennes (BDG) equations have been used to study the linear stability of system. The stationary states of the systems are slightly perturbed, such that:

$$R = P + a(r,z)exp(-i\mu z), \qquad S = Q + b(r,z)exp(-i\mu z), \tag{5.22}$$

where,

$$a(r,z) = a_1(r)exp(i\lambda z) + a_2(r)exp(-i\lambda^* z), \tag{5.23}$$

$$b(r,z) = b_1(r)exp(i\lambda z) + b_2(r)exp(-i\lambda^* z), \tag{5.24}$$

where the asterisk represents the complex conjugation. The pair of coupled Equations (5.20) and (5.21) are linearized after being converted into radial coordinates, assuming that a_1, a_2, b_1, and b_2 are very small. The four homogeneous equations are satisfied by a_1, a_2, b_1, and b_2, as seen in the matrix below:

$$\lambda \begin{pmatrix} a_1 \\ a_2^* \\ b_1 \\ b_2^* \end{pmatrix} = C \begin{pmatrix} a_1 \\ a_2^* \\ b_1 \\ b_2^* \end{pmatrix}, \tag{5.25}$$

where the matrix C is given by,

$$\begin{pmatrix} L_1 + V(r) & 0 & \frac{1}{4}e^{\frac{iz}{1+\gamma(\tau)}}sin2\xi & \frac{R^2}{2} \\ \frac{R^2}{2} & -L_1 - V(r) & 0 & -\frac{1}{4}e^{\frac{-iz}{1+\gamma(\tau)}}sin2\xi \\ \frac{1}{4\gamma(\tau)}e^{\frac{-iz}{1+\gamma(\tau)}}sin2\xi & \frac{S^2}{2} & L_2 + V(r) & 0 \\ 0 & -\frac{1}{4\gamma(\tau)}e^{\frac{iz}{1+\gamma(\tau)}}sin2\xi & \frac{S^2}{2} & -L_2 - V(r) \end{pmatrix}, \tag{5.26}$$

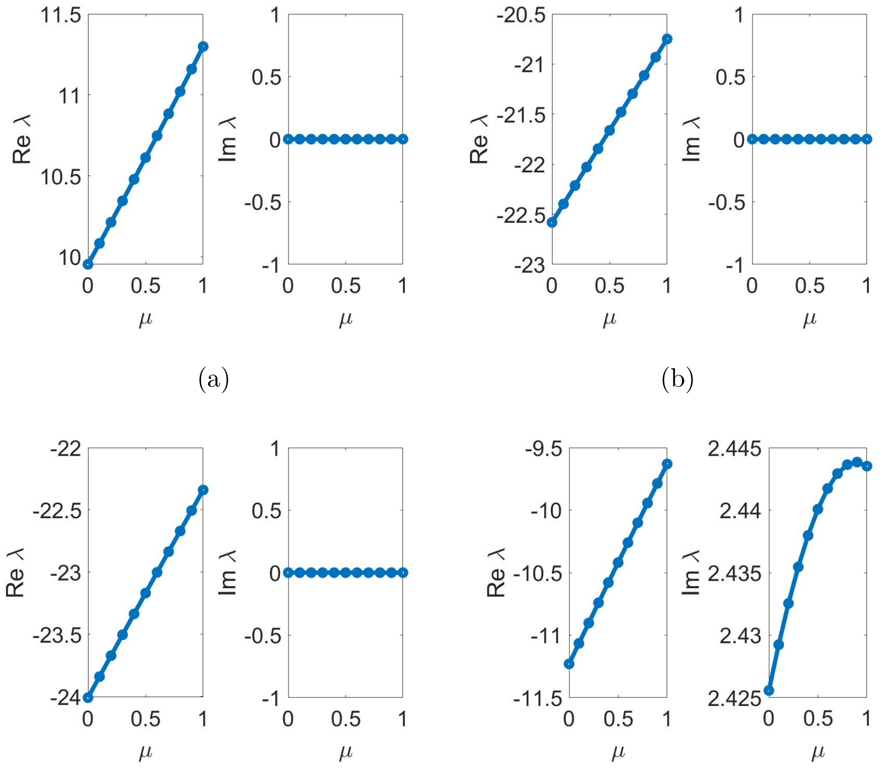

(a) (b)

(c) (d)

Figure 5.8: The results of linear stability analysis of the system for thermal response coefficients (a) $\tau_0 = \tau_1 = 0$, (b) $\tau_0 = \tau_1 = 0.8$, (c) $\tau_0 = \tau_1 = 2.0$, and (d) $\tau_0 = \tau_1 = 2.4$. The real and imaginary parts of the perturbation eigenvalues (λ) versus the propagation constant μ are shown.

$$L_1 = \frac{1}{2}\left(\frac{d^2}{dr^2} + \frac{1}{r}\frac{d}{dr} + sin^2\xi + |R|^2 + 2\mu\right), \tag{5.27}$$

$$L_2 = \frac{1}{2\gamma}\left(\frac{d^2}{dr^2} + \frac{1}{r}\frac{d}{dr} - sin^2\xi + |S|^2 + 2\gamma\mu\right). \tag{5.28}$$

The system is solved using spectral methods based on Chebyshev polynomials. A grid 40 along r is chosen to evaluate the diffraction operators.

The perturbation eigenvalues have been analyzed as functions of the propagation constants. The type of eigenvalue determines the stability of the solution. Any eigenvalue with an imaginary part will cause the perturbed solution to grow exponentially with z, which gives rise to linearly unstable solutions. If all imaginary eigenvalues are equal to zero, the solutions are completely stable.

Figure (5.8) shows stability plots for single-peak and double-peak nematicons. The strength of the potential is assumed to be $V_0 = 1.2$ V/μm. Figure 5.8(a) depicts the stability plots for single-peak nematicons in the absence of thermal response coefficients. The solutions are stable with purely real eigenvalues. Figures 5.8(b)-(d) depict stability plots for double-peak nematicons with different thermal response coefficients. Figures 5.8(b), (c), and (d) depict the stability plots for $\tau_0 = \tau_1 = 0.8$, $\tau_0 = \tau_1 = 2.0$, and $\tau_0 = \tau_1 = 2.4$ respectively. The magnitudes of imaginary eigenvalues are zero in Figures 5.8(b) and (c), showing that the associated solutions are linearly stable. In Figure 5.8(d), the magnitudes of imaginary eigenvalues are not zero, indicating that the corresponding solutions are linearly unstable.

According to the linear stability analysis, single-peak and double-peak nematicons having periodic oscillations are stable, while the double-peak nematicons with a non-oscillatory nature are unstable.

5.5 Conclusion

The thermal response of nematicons in a parabolic potential has been studied numerically. Single-peak nematicons are observed only when thermal response coefficients are absent, as focusing reorientational nonlinearity dominates under these conditions. However, when thermal effects are introduced, the interaction between focusing reorientational and defocusing thermal nonlinearities causes the transformation of single-peak nematicons into double-peak nematicons. In this regime, the beam profile splits into double-peaks because the defocusing thermal nonlinearity surpasses the focusing reorientational nonlinearity. These competing nonlinearities modify the energy landscape encountered by the light beam in the medium. The combination of focusing reorientational and defocusing thermal nonlinearities creates multiple maxima in the energy landscape, stabilizing double-peak nematicons as equilibrium states. Under a parabolic potential, periodic oscillations can be observed in nematicons. For low thermal response coefficients, double-peak nematicons with periodic oscillations form. The thermal response significantly influences the oscillation wavelength of these double-peak nematicons, with the wavelength increasing as the thermal response coefficients rise. When thermal response coefficients are large, double-peak nematicons cease to oscillate. Linear stability analysis shows that both single-peak nematicons and oscillatory double-peak nematicons are stable, while non-oscillatory double-peak nematicons are unstable.

The findings presented in this chapter offer several practical applications, particularly in the design and control of optical systems. The ability to manipulate nematicons through a combination of thermal and reorientational nonlinearities could be highly useful for creating tunable optical waveguides. By adjusting thermal response coefficients, engineers can control whether nematicons exhibit single or double-peak structures as well as their oscillatory behavior which is important for fine-tuning light propagation in photonic circuits. The insights from this study into the competition between focusing and defocusing nonlinearities can aid in the development of optical devices requiring precise control over beam shaping and energy distribution. For instance, double-peak nematicons with periodic oscillations, stabilized by the interplay of nonlinear effects could be applied to advanced signal processing systems that require dynamic light modulation. Additionally, the dependence of oscillation wavelength on thermal response coefficients provides a new mechanism for engineers to adjust optical signal characteristics in real-time, enhancing the flexibility of optical communication technologies. Moreover, the understanding of stability conditions derived from this research could prove valuable in designing robust photonic systems. Identifying when nematicons remain stable against perturbations allows for the creation of stable optical structures, which are crucial for applications such as quantum computing, laser technologies, and imaging systems where reliable light confinement and stability are required.

Bibliography

[1] Shen Y, Dierking I. Recent Progresses on Experimental Investigations of Topological and Dissipative Solitons in Liquid Crystals. Crystals. 2022 jan;12(1):94.

[2] Nys I, Berteloot B, Poy G. Surface Stabilized Topological Solitons in Nematic Liquid Crystals. Crystals. 2020 sep;10(9):840.

[3] Aya S, Araoka F. Kinetics of motile solitons in nematic liquid crystals. Nature Communications. 2020 jun;11(1).

[4] Altawallbeh Z, Az-Zo'bi E, Alleddawi AO, Şenol M, Akinyemi L. Novel liquid crystals model and its nematicons. Optical and Quantum Electronics. 2022 Oct;54(12):1-17.

[5] Jiang Y, Wang F, Khater MMA, Al-Sehemi AG, Ullah S, Al-Hartomy OA, et al. Abundant novel nematicon soliton wave solutions in liquid crystals with Kerr law nonlinearity. Journal of Ocean Engineering and Science. 2022 Apr.

[6] Zhang G, Song N, Ding Z. Solitary waves for one-dimensional nematicon equations. Journal of Mathematical Analysis and Applications. 2019 jul;475(1):686-98.

[7] Laudyn UA, Piccardi A, Kwasny M, Karpierz MA, Assanto G. Thermo-optic soliton routing in nematic liquid crystals. Optics Letters. 2018 may;43(10):2296.

[8] Assanto G, Minzoni AA, Smyth NF, Worthy AL. Refraction of nonlinear beams by localized refractive index changes in nematic liquid crystals. Physical Review A. 2010 nov;82(5):053843.

[9] Smyth NF, Assanto G, Skuse BD. Optical path control of solitary waves in dye-doped nematic liquid crystals. Photonics Letters of Poland. 2009 dec;1(4).

[10] Urbanski M. On the impact of nanoparticle doping on the electro-optic response of nematic hosts. Liquid Crystals Today. 2015 sep;24(4):102-15.

[11] Singh BP, Sikarwar S, Pandey KK, Manohar R, Depriester M, Singh DP. Carbon Nanotubes Blended Nematic Liquid Crystal for Display and Electro-Optical Applications. Electronic Materials. 2021 Oct;2(4):466-81.

[12] Assanto G. Nematicons: reorientational solitons from optics to photonics. Liquid Crystals Reviews. 2018 Jul;6(2):170-94.

[13] Zarnescu A. Mathematical problems of nematic liquid crystals: between dynamical and stationary problems. Philosophical Transactions of the Royal Society A: Mathematical, Physical and Engineering Sciences. 2021 may;379(2201):20200432.

[14] Kwaśny M, Ostromęcka I, Klus BW, Laudyn UA. Interplay of reorientational and thermal solitons: unveiling the dynamic coexistence and enhanced nonlinear response in nematic liquid crystals. Optical Materials Express. 2023 jun;13(7):2071.

[15] Laudyn U, Piccardi A, Kwasny M, Klus B, Karpierz M, Assanto G. Interplay of Thermo-Optic and Reorientational Responses in Nematicon Generation. Materials. 2018 sep;11(10):1837.

[16] Assanto G, Khan C, Smyth NF. Multihump thermo-reorientational solitary waves in nematic liquid crystals: Modulation theory solutions. Physical Review A. 2021 jul;104(1):013526.

[17] Assanto G, Khan C, Piccardi A, Smyth NF. Temperature control of nematicon trajectories. Physical Review E. 2019 dec;100(6):062702.

[18] Jung PS, Krolikowski W, Laudyn UA, Trippenbach M, Karpierz MA. Supermode spatial optical solitons in liquid crystals with competing nonlinearities. Physical Review A. 2017 feb;95(2):023820.

[19] Aleksić NB, Petrović MS, Strinić AI, Belić MR. Solitons in highly nonlocal nematic liquid crystals: Variational approach. Physical Review A. 2012 mar;85(3):033826.

[20] Sajitha NM, Suneera TP. The effect of parabolic potential on the generation of higher harmonics of nematicons. Physica Scripta. 2023 Apr;98(5):055502.

Chapter 6

Dynamics of Gap Nematicons

This chapter investigates the formation and stability of single-peak and multi-peak gap nematicons using numerical methods. The study focuses on both stationary and dynamic solutions within the first band gap. Single-peak and multi-peak gap nematicons are found to exist in this region, with single-peak nematicons observed over a broad range of propagation constants. However, multi-peak gap nematicons are only present above a specific minimum propagation constant. The intensity distribution across the peaks of a multi-peak gap nematicon is strongly influenced by the input beam intensity. Stability analysis reveals that single-peak gap nematicons are stable. Among multi-peak gap nematicons those with equal peak amplitudes are stable, while those with unequal amplitudes are unstable. The primary application of this study is that multi-peak gap nematicons improve data-carrying capacity, facilitating faster data transmission in optical communications compared to single-peak nematicons.

The results of this chapter are published as:

- N. M. Sajitha, T. P. Suneera, 'The formation and stability of single-peak and multi-peak gap nematicons in a periodic potential'. Liquid Crystals. 2024 Sep; 1–13.

6.1 Introduction

Due to the distinctive dispersion curves and band gaps in periodic media, studying nonlinear wave phenomena is particularly fascinating. One notable area of research involves gap solitons, soliton-like states that travel through periodic media [1]. Theoretically, these gap solitons can propagate at any speed from zero to the speed of light [2]. Spatial gap solitons have potential applications in fields such as image memory, signal processing, and communication [3–5]. Gap solitons remain a promising topic for future technological applications such as nonlinear optical switches, soliton lasers, pulse compressors, and optical buffers [6–8].

Understanding gap soliton behavior in nematic liquid crystals is essential for their use in nonlinear optics, particularly in applications like optical switching and signal processing [9, 10]. Nematic liquid crystals are commonly employed in spatial light modulators (SLMs) which alter the phase, amplitude, or polarization of light [11]. Gap solitons provide a means to control light propagation in these devices enabling precise manipulation of optical signals. This capability has promising applications in photonics such as optical communication, data processing, and sensing [12]. For instance, gap solitons could be key to developing optical switches and routers for high-speed data networks. Research on gap soliton formation and dynamics in nematic liquid crystals enhances our understanding of nonlinear wave behavior in complex media, advancing both fundamental physics and the study of other nonlinear systems. Devices based on nematic liquid crystals are lightweight, compact, and cost-effective compared to conventional optical components [13]. Gap solitons have the potential to improve the performance and miniaturization of these devices, paving the way for applications in fields like telecommunications and biomedical imaging [14].

This chapter delves into the formation and stability of gap nematicons, localized optical structures within a periodic potential. Through numerical analysis, it examines single-peak and multi-peak gap nematicons within the first band gap, exploring conditions that enable their existence. A key focus is on understanding how these structures differ in stability and formation based on variables like propagation constant and initial beam intensity. Additionally, the research analyzes how the intensity is distributed among peaks in multi-peak nematicons, influenced significantly by the initial beam strength. Using Bogoliubov-de Gennes equations, the study further analyzes the stability characteristics of these nematicons.

This chapter is organized as follows. Section 6.2 describes the theoretical model for beam propagation in a nematic liquid crystal with a periodic potential in the nonlocal regime. Section 6.3 describes the band gap spectrum produced by the periodic potential. The stationary solutions are also discussed in section 6.3. The propagation dynamics of gap nematicons are described in section 6.4. Section 6.5 contains the results and discussions. In section 6.6, the stability of the nematicon against small perturbations has been investigated using linear stability analysis. Section 6.7 concludes the chapter.

6.2 Theoretical model

Consider an optical beam moving in the z-direction through a positive uniaxial NLC. Figure (6.1) depicts the geometry of the NLC cell. The optic axis of the nematic is aligned along the y-direction and its reorientation in the xy plane is indicated by the angle ξ. A nonlinear Schrodinger-type equation with periodic potential models the optical beam and an elliptic Poisson equation for the molecular director. The governing equations of the system are given by [15, 16]

$$2ik_0n_\perp\frac{\partial E_x}{\partial z}+\frac{\partial^2 E_x}{\partial x^2}+\frac{\partial^2 E_x}{\partial y^2}+k_o^2\epsilon_a E_x sin^2\xi+\frac{1}{2}k_0^2\epsilon_a E_y e^{ik_0(n_\parallel-n_\perp)z}sin2\xi \\ +V(x,y)E_x=0, \qquad (6.1)$$

$$2ik_0n_\parallel\frac{\partial E_y}{\partial z}+\frac{\partial^2 E_y}{\partial x^2}+\frac{n_\parallel^2}{n_\perp^2}\frac{\partial^2 E_y}{\partial y^2}-k_o^2\epsilon_a E_y sin^2\xi+\frac{1}{2}k_0^2\epsilon_a E_x e^{-ik_0(n_\parallel-n_\perp)z}sin2\xi \\ -V(x,y)E_y=0, \qquad (6.2)$$

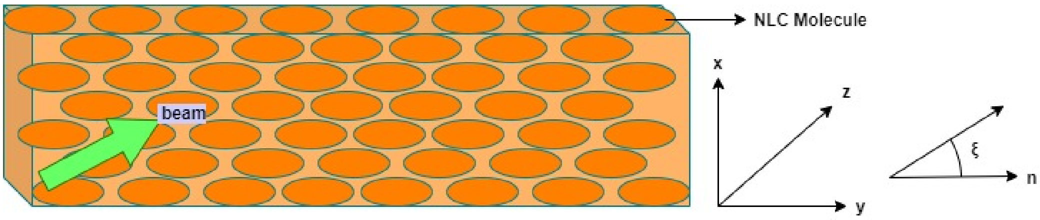

Figure 6.1: The interaction geometry. A nematic liquid crystal with ellipses with long axes parallel to y is used to represent the elongated NLC. The green arrow indicates the input light beam impinging normally to the molecular director on the sample. The reorientation of the optic axis, n in the (x, y) plane is described by the angle ξ.

$$K\nabla^2\xi + \frac{1}{4}\epsilon_0\epsilon_a\left[2(|E_x|^2 - |E_y|^2)sin2\xi + 2ReE_xE_y^*e^{-ik_0(n_{\parallel}-n_{\perp})z}cos2\xi\right] = 0. \tag{6.3}$$

E_x and E_y refer to the x and y components of the electric fields with k_0 being the ordinary wave vector. The director angle is denoted by ξ. z be the propagation distance. ϵ_a represents the birefringence of the nematic. The elastic constant K of the medium is assumed to be a constant for all types of deformations such as bend, splay, and twist. The refractive indices parallel and perpendicular to the director alignment are represented by $n_{\parallel}$ and $n_{\perp}$, respectively. The different constants in the model are taken from the material properties of the standard E7 mixture at room temperature, which is a positive uniaxial NLC with $n_{\parallel}$=1.73 and $n_{\perp}$=1.53, and elastic constant K=12pN [17]. The two-dimensional Laplacian is represented by $\nabla^2\xi$. $V(x, y)= V_0\ cos^2\left(\sqrt{x^2 + y^2}\right)$. $V(x, y)$ is the periodic potential of period π and a strength of V_0.

The equations describing the x and y components of the electric field of the beam are

$$E_x = Xe^{ik_0n_{\perp}z}, \qquad E_y = Ye^{ik_0n_{\parallel}z}. \tag{6.4}$$

The components of electric fields in two transverse directions are represented by X and Y. By substituting Equation (6.4) in Equations (6.1) - (6.3), we obtain,

$$2i\frac{\partial X}{\partial z}+\frac{\partial^2 X}{\partial x^2}+\frac{\partial^2 X}{\partial y^2}+Xsin^2\xi+\frac{1}{2}Ye^{\frac{iz}{1+\gamma}}sin2\xi+V(x,y)X=0, \tag{6.5}$$

$$2i\gamma\frac{\partial Y}{\partial z}+\frac{\partial^2 Y}{\partial x^2}+\frac{\partial^2 Y}{\partial y^2}-Ysin^2\xi+\frac{1}{2}Xe^{\frac{-iz}{1+\gamma}}sin2\xi-V(x,y)Y=0, \tag{6.6}$$

$$\nu\nabla^2\xi+(|X|^2-|Y|^2)sin2\xi+2Re(XY^*e^{\frac{-iz}{1+\gamma}})cos2\xi=0, \tag{6.7}$$

where,

$$\gamma=\frac{n_\parallel}{n_\perp}, \qquad \nu=\frac{4Kk_0^2}{\epsilon_0 A_b^2}. \tag{6.8}$$

The symbols γ and ν in the above equations represent anisotropy and nonlocality, respectively. The amplitude of the input optical beam is denoted by A_b.

6.3 Band gap spectrum and stationary solutions

6.3.1 Band gap spectrum

Assuming solutions of Equations (6.5) - (6.7) in terms of the propagation constant μ,

$$X(x,y,z) \; = P(x,y)e^{-i\mu z}, \qquad Y(x,y,z) \; = Q(x,y)e^{-i\mu z}, \tag{6.9}$$

yield steady-state equations,

$$\frac{\partial^2 P}{\partial x^2}+\frac{\partial^2 P}{\partial y^2}+Psin^2\xi+\frac{1}{2}Qe^{\frac{iz}{1+\gamma}}sin2\xi+V(x,y)P=-2\mu P, \tag{6.10}$$

$$\frac{\partial^2 Q}{\partial x^2}+\frac{\partial^2 Q}{\partial y^2}-Qsin^2\xi+\frac{1}{2}Pe^{\frac{-iz}{1+\gamma}}sin2\xi-V(x,y)Q=-2\mu\gamma Q, \tag{6.11}$$

$$\nu\nabla^2\xi + (|P|^2 - |Q|^2)sin2\xi + 2Re(PQ^*e^{\frac{-iz}{1+\gamma}})cos2\xi = 0. \tag{6.12}$$

Since the potential is periodic, the system supports Bloch waves of the form

$$P(x,y) \;\; = P_k(x,y)e^{i(kx+ky)}, \qquad Q(x,y) \;\; = Q_k(x,y)e^{i(kx+ky)}, \tag{6.13}$$

where k represents the Bloch momentum with the periodicity condition

$$P_k(x+\pi,y) \;\; = P_k(x,y), \qquad Q_k(x,y+\pi) \;\; = Q_k(x,y). \tag{6.14}$$

The Bloch solutions satisfy the equation:

$$\begin{aligned}\frac{\partial^2 P_k}{\partial x^2} + \frac{\partial^2 P_k}{\partial y^2} - 2k^2P_k + P_k sin^2\xi + \frac{1}{2}Q_k e^{\frac{iz}{1+\gamma}} sin2\xi \\ +V(x,y)P_k = -2\mu P_k,\end{aligned} \tag{6.15}$$

$$\begin{aligned}\frac{\partial^2 Q_k}{\partial x^2} + \frac{\partial^2 Q_k}{\partial y^2} - (1+\gamma^2)k^2Q_k - Q_k sin^2\xi + \frac{1}{2}P_k e^{\frac{-iz}{1+\gamma}} sin2\xi \\ -V(x,y)Q_k = -2\mu\gamma Q_k,\end{aligned} \tag{6.16}$$

$$\nu\nabla^2\xi + (|P_k|^2 - |Q_k|^2)sin2\xi + 2Re(P_kQ_k^*e^{\frac{-iz}{1+\gamma}})cos2\xi = 0. \tag{6.17}$$

This work focuses on radially symmetric solutions, hence Equations (6.15) - (6.17) are expressed in radial coordinates as

$$\begin{aligned}\frac{\mathrm{d}^2 P_k}{\mathrm{d}r^2} + \frac{1}{r}\frac{\mathrm{d}P_k}{\mathrm{d}r} - 2k^2P_k + P_k sin^2\xi + \frac{1}{2}Q_k e^{\frac{iz}{1+\gamma}} sin2\xi \\ +V(r)P_k = -2\mu P_k,\end{aligned} \tag{6.18}$$

$$\begin{aligned}\frac{\mathrm{d}^2 Q_k}{\mathrm{d}r^2} + \frac{1}{r}\frac{\mathrm{d}Q_k}{\mathrm{d}r} - (1+\gamma^2)k^2Q_k - Q_k sin^2\xi + \frac{1}{2}P_k e^{\frac{-iz}{1+\gamma}} sin2\xi \\ -V(r)Q_k = -2\mu\gamma Q_k,\end{aligned} \tag{6.19}$$

$$\nu\frac{\mathrm{d}^2\xi}{\mathrm{d}r^2} + \frac{\nu}{r}\frac{\mathrm{d}\xi}{\mathrm{d}r} + (|P_k|^2 - |Q_k|^2)sin2\xi + 2Re(P_kQ_k^*e^{\frac{-iz}{1+\gamma}})cos2\xi = 0. \tag{6.20}$$

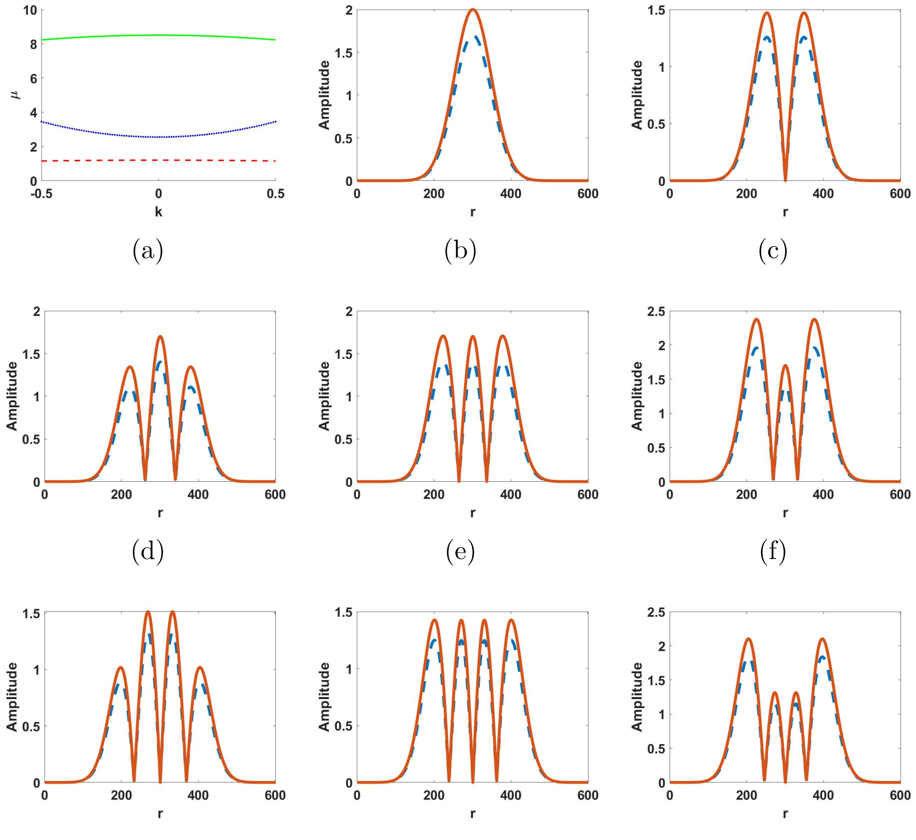

(a) (b) (c)

(d) (e) (f)

(g) (h) (i)

Figure 6.2: Band gap spectrum and the stationary states. First row: (a) Band gap spectrum - The eigenvalue μ versus Bloch momentum k, with the first band in red (dashed) line, the second band in blue (dotted) line, and the third band in green (solid) line; (b) single-peak gap nematicons for a_{x0}=1.7, a_{y0}=2.0; (c) two peak gap nematicons for a_{x0}=4.1, a_{y0}=4.8. Second row for three peak gap nematicons: (d) a_{x0}=4.1, a_{y0}=4.9; (e) a_{x0}=4.5, a_{y0}=5.3; (f) a_{x0}=4.8, a_{y0}=5.6. Third row for four peak gap nematicons: (g) a_{x0}=8.3, a_{y0}=9.0; (h) a_{x0}=8.8, a_{y0}=9.5; (i) a_{x0}=9.6, a_{y0}=10.3. In all three rows, the strength of periodic potential is $V_0 = 1.7$. P blue (dashed) and Q red (solid) in Figures 6.2(b)-(i).

The periodic potential in radial coordinates is given by $V(r) = V_0\ cos^2 r$, where V_0 represents the strength of the periodic potential. The eigenvalues are computed for Bloch momentum k for the strength of the periodic potential $V_0 = 1.7$. Figure 6.2(a) depicts a band gap spectrum with three bands. The first band is shown in red (dashed) line, the second in blue (dotted) line, and the third in green (solid) line. The first finite band gap covers an interval of 1.1999 $\leq\mu\leq$ 2.55, and the second band gap spans an interval of 3.45 $\leq\mu\leq$ 8.2.

6.3.2 Stationary solutions

Consider uniaxial NLC has a cylindrical symmetry. A rotational symmetry about the propagation direction z is also assumed for the system. Then, $x^2 + y^2 = r^2$ and $\nabla^2 = \frac{1}{r}\frac{\partial}{\partial r} + \frac{\partial^2}{\partial r^2}$. The stationary differential Equations (6.10)-(6.12) becomes

$$\frac{\mathrm{d}^2 P}{\mathrm{d}r^2} + \frac{1}{r}\frac{\mathrm{d}P}{\mathrm{d}r} + Psin^2\xi + \frac{1}{2}Qe^{\frac{iz}{1+\gamma}}sin2\xi + V(r)P = -2\mu P, \tag{6.21}$$

$$\frac{\mathrm{d}^2 Q}{\mathrm{d}r^2} + \frac{1}{r}\frac{\mathrm{d}Q}{\mathrm{d}r} - Qsin^2\xi + \frac{1}{2}Pe^{\frac{-iz}{1+\gamma}}sin2\xi - V(r)Q = -2\mu\gamma Q, \tag{6.22}$$

$$\nu\frac{\mathrm{d}^2 \xi}{\mathrm{d}r^2} + \frac{\nu}{r}\frac{\mathrm{d}\xi}{\mathrm{d}r} + (|P|^2 - |Q|^2)sin2\xi + 2Re(PQ^* e^{\frac{-iz}{1+\gamma}})cos2\xi = 0. \tag{6.23}$$

Equations (6.21) - (6.23) have been numerically analyzed, and the stationary solutions P and Q for different values of propagation constants in the first band gap are shown in Figures 6.2(b)-(i).

Figure 6.2(b) shows that the single-peak gap nematicons are obtained for a propagation constant of $\mu = 1.25$. Multi-peak gap nematicons can exist only above a certain minimum value of propagation constant. The effects of input beam intensities on various peaks in a multi-peak gap nematicon have been investigated. When the propagation constant $\mu = 1.9$, two peak gap nematicons can be found, as depicted in Figure 6.2(c). Three peak gap nematicons can be found when the propagation constant $\mu = 2.2$, as shown in the second row. As depicted in Figure 6.2(e), the amplitudes of the multiple peaks in the three peak gap nematicon are the same for the input wave amplitudes a_{x0}=4.5, a_{y0}=5.3. The amplitudes of various peaks in the three peak gap nematicon vary as the amplitudes of the input wave decrease or increase, as shown in Figures 6.2(d) and (f). Four peak gap nematicons can be found when the propagation constant is $\mu = 2.45$, as in the third row. As shown in Figure 6.2(h), the amplitudes of the four-peak gap nematicon are the same for the input wave amplitudes a_{x0}=8.8, a_{y0}=9.5. The amplitudes of multiple peaks in a four-peak gap nematicon vary as the amplitude or intensity of the input wave changes, as shown in Figures 6.2(g) and (i).

6.4 Propagation dynamics of gap nematicons

The dynamic solution of the Equations (6.5) - (6.7) are studied in terms of the propagation constant μ as

$$X(x,y,z) \ = R(x,y,z)e^{-i\mu z}, \qquad Y(x,y,z) \ = S(x,y,z)e^{-i\mu z}. \tag{6.24}$$

The substitution of X and Y in Equations (6.5) - (6.7) give the nonlinear eigenvalue problem as

$$2i\frac{\partial R}{\partial z}+\frac{\partial^2 R}{\partial x^2}+\frac{\partial^2 R}{\partial y^2}+Rsin^2\xi+\frac{1}{2}Se^{\frac{iz}{1+\gamma}}sin2\xi+V(x,y)R=-2\mu R, \tag{6.25}$$

$$2i\gamma\frac{\partial S}{\partial z}+\frac{\partial^2 S}{\partial x^2}+\frac{\partial^2 S}{\partial y^2}-Ssin^2\xi+\frac{1}{2}Re^{\frac{-iz}{1+\gamma}}sin2\xi-V(x,y)S=-2\mu\gamma S, \tag{6.26}$$

$$\nu\nabla^2\xi+(|R|^2-|S|^2)sin2\xi+2Re(RS^*e^{\frac{-iz}{1+\gamma}})cos2\xi=0. \tag{6.27}$$

For radial symmetry, the Equations (6.25) - (6.27) becomes

$$2i\frac{\partial R}{\partial z}+\frac{\partial^2 R}{\partial r^2}+\frac{1}{r}\frac{\partial R}{\partial r}+Rsin^2\xi+\frac{1}{2}Se^{\frac{iz}{1+\gamma}}sin2\xi+V(r)R=-2\mu R, \tag{6.28}$$

$$2i\gamma\frac{\partial S}{\partial z}+\frac{\partial^2 S}{\partial r^2}+\frac{1}{r}\frac{\partial S}{\partial r}-Ssin^2\xi+\frac{1}{2}Re^{\frac{-iz}{1+\gamma}}sin2\xi-V(r)S=-2\mu\gamma S, \tag{6.29}$$

$$\nu\frac{\partial^2\xi}{\partial r^2}+\frac{\nu}{r}\frac{\partial\xi}{\partial r}+(|R|^2-|S|^2)sin2\xi+2Re(RS^*e^{\frac{-iz}{1+\gamma}})cos2\xi=0. \tag{6.30}$$

R, S and ξ satisfy the equations [18],

$$R=\left(a_x e^{\frac{-r^2}{w_x^2}}\right)e^{i\sigma_x}, \qquad S=\left(a_y e^{\frac{-r^2}{w_y^2}}\right)e^{i\sigma_y}, \tag{6.31}$$

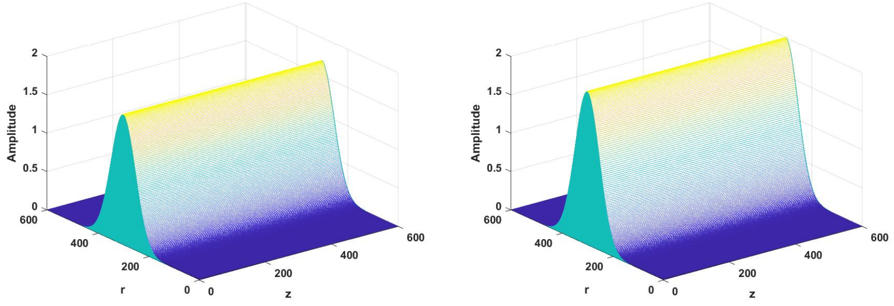

(a) (b)

Figure 6.3: Evolution of beam for an initial excitation with a_{x0}=1.7, a_{y0}=2.0, w_{x0}=12, w_{y0}=12, σ_{x0}=0, σ_{y0}=0 with propagation constant μ=1.25 for a periodic potential strength of $V_0 = 1.7$. (a) Evolution of R; (b) Evolution of S.

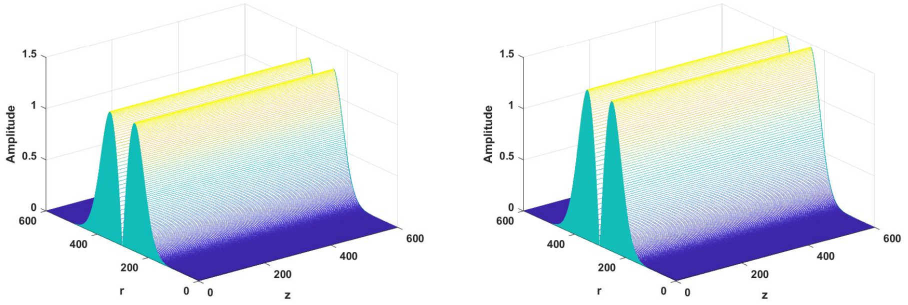

(a) (b)

Figure 6.4: Evolution of beam for an initial excitation with a_{x0}=4.1, a_{y0}=4.8, w_{x0}=12, w_{y0}=12, σ_{x0}=0, σ_{y0}=0 with propagation constant μ=1.9 for a periodic potential strength of $V_0 = 1.7$. (a) Evolution of R; (b) Evolution of S.

and

$$\xi = \alpha e^{\frac{-r^2}{\beta^2}} + A\left[Ei\left(\frac{-r^2}{\beta^2}\right) - ln\left(\frac{r^2}{d^2}\right)\right]. \tag{6.32}$$

In Equation (6.32), $r^2 = x^2 + y^2$ and α depends on the propagation distance z through the relation [19],

$$\alpha = \frac{2}{D}\frac{a_x a_y w_x^2 w_y^2 \beta^2 cos\theta}{\nu - \beta^2 \Delta}, \tag{6.33}$$

where,

$$D = \beta^2 w_x^2 + \beta^2 w_y^2 + w_x^2 w_y^2, \qquad \theta = \frac{z}{1+\gamma} - \sigma_x + \sigma_y. \tag{6.34}$$

The amplitudes of the beam are a_x and a_y, widths are w_x and w_y, and the phases are σ_x and σ_y in the two transverse directions. The first term in Equation (6.32) denotes the local contribution of the director in which α be the amplitude and β be the width, while the second and third terms denote the nonlocal contributions of the director with amplitude A. β is given by the relation, β=$L/(2\ln 100)$. The thickness of the NLC cell is denoted by L. d stands for half the thickness of the NLC cell. Ei represents the exponential integral function, $E_i = -\int_{-z}^{+\infty} e^{-t}t^{-1}dt$.

The finite difference method has been implemented to solve the system of coupled partial differential Equations (6.28) - (6.30). This method imposes a rectangular grid on the problem with the grid planes separated by Δz and Δr, so that $z_m = m\Delta z$ and $r_n = n\Delta r$, respectively. By selecting $\frac{\Delta z}{\Delta r^2} \leq 0.5$, the stability requirement is met.

In this work, the nematicon solutions are studied in the first band gap. The propagation of the beam is investigated in the presence of a periodic potential and the numerical results of Equations (6.28) - (6.30) are presented graphically in section 6.5.

6.5 Results and discussions

The analysis has been done to investigate the formation and stability of single-peak and multi-peak gap nematicons. The numerical solutions of Equations (6.28) - (6.30) are investigated in the first band gap of the spectrum, where the propagation constant values range between 1.1999 $\leq\mu\leq$ 2.55.

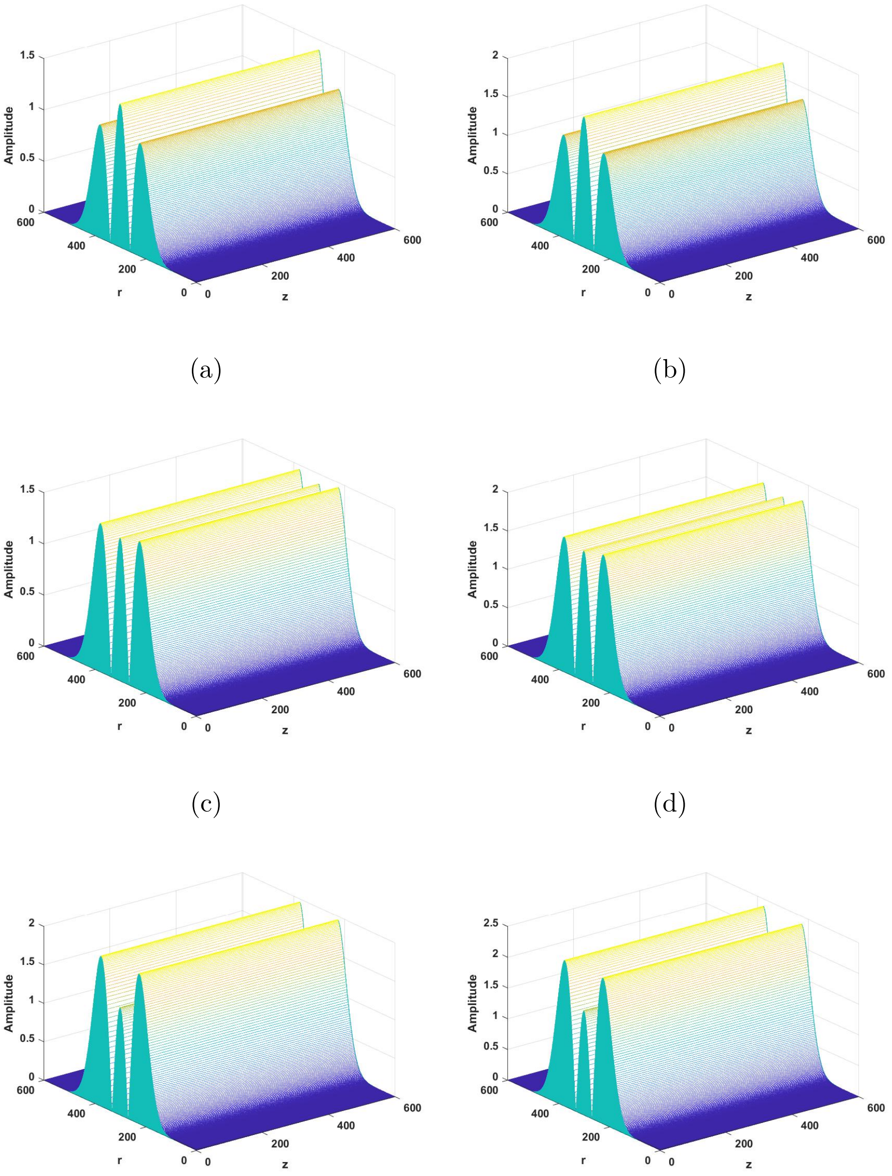

(a) (b)

(c) (d)

(e) (f)

Figure 6.5: Evolution of beam for an initial excitation with w_{x0}=12, w_{y0}=12, σ_{x0}=0, σ_{y0}=0 with propagation constant μ=2.2. First column: evolution of R; second column: evolution of S. First row for a_{x0}=4.1, a_{y0}=4.9; second row for a_{x0}=4.5, a_{y0}=5.3; third row for a_{x0}=4.8, a_{y0}=5.6. In all three rows, the strength of periodic potential is $V_0 = 1.7$.

6.5.1 Single-peak gap nematicons

Figure (6.3) shows the formation of single-peak gap nematicons when the input wave amplitudes are a_{x0}=1.7 and a_{y0}=2.0. Figures 6.3(a) and (b) depict the evolution of the dynamic solutions R and S of Equations (6.28) - (6.30) for a potential strength of $V_0 = 1.7$ and propagation constant $\mu = 1.25$.

The analysis has been carried out for various propagation constant values ranging from 1.2 to 1.8. Even when the amplitudes of the input waves are varied, only a single-peak gap nematicon can be found for all of these propagation constant values.

6.5.2 Multi-peak gap nematicons

The study has been carried out for μ=1.9 by varying the amplitude of the input beam in the numerical analysis of Equations (6.28) - (6.30) using the finite difference method. The results are shown in Figure (6.4), which depicts the formation of two peak gap nematicons when the input wave amplitudes are a_{x0}=4.1 and a_{y0}=4.8. Figures 6.4(a) and (b) show the evolution of the amplitudes R and S of two peak gap nematicons when $V_0 = 1.7$.

When the propagation constant μ=2.2, three peak gap nematicons can be found, as shown in Figure (6.5). The first row shows the evolution of amplitudes for a_{x0}=4.1 and a_{y0}=4.9, while the second row shows the evolution of amplitudes for a_{x0}=4.5 and a_{y0}=5.3. When the amplitudes of the input waves are a_{x0}=4.8 and a_{y0}=5.6, the amplitude evolution of three peak gap nematicons is depicted in the third row of Figure (6.5). We can obtain different types of three peak gap nematicon profiles by varying the amplitudes of the input waves for a particular value of the propagation constant (μ=2.2). The amplitudes of the multiple peaks in the three peak gap nematicon are the same for the input wave amplitudes a_{x0}=4.5 and a_{y0}=5.3, as shown in the second row. The amplitudes of various peaks in the three peak gap nematicon vary as the amplitudes of the input wave decrease or increase, as shown in the first and third rows.

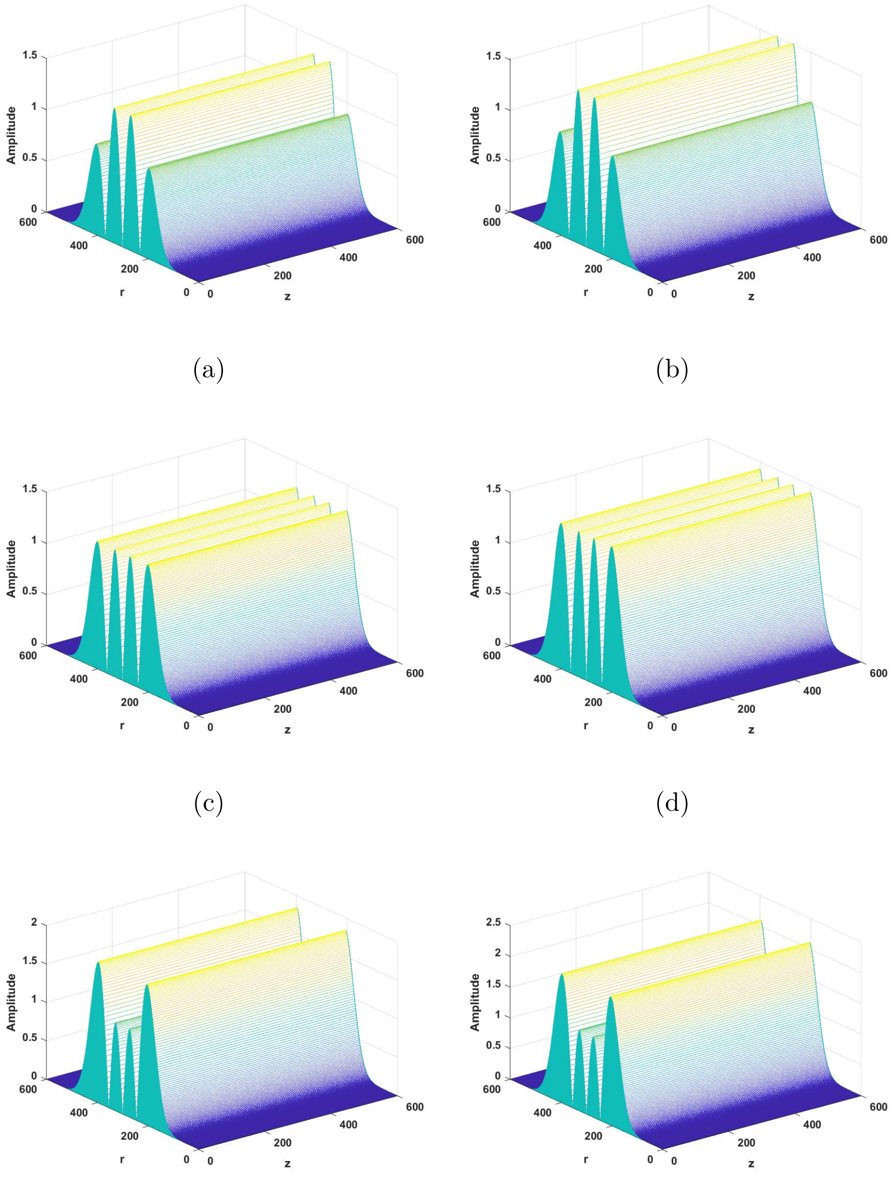

(a) (b)

(c) (d)

(e) (f)

Figure 6.6: Evolution of beam for an initial excitation with w_{x0}=12, w_{y0}=12, σ_{x0}=0, σ_{y0}=0 with propagation constant μ=2.45. First column: evolution of R; second column: evolution of S. First row for a_{x0}=8.3, a_{y0}=9.0; second row for a_{x0}=8.8, a_{y0}=9.5; third row for a_{x0}=9.6, a_{y0}=10.3. In all three rows, the strength of periodic potential is $V_0 = 1.7$.

Four peak gap nematicons can be found when the propagation constant is μ=2.45, as shown in Figure (6.6). The first row depicts the evolution of the amplitudes of four peak gap nematicons for a_{x0}=8.3 and a_{y0}=9.0. The second row shows the evolution of amplitudes for a_{x0}=8.8 and a_{y0}=9.5. The third row shows the amplitude evolution for input wave amplitudes of a_{x0}=9.6, a_{y0}=10.3. We can obtain various types of four-peak gap nematicons for different input wave amplitudes. As shown in the second row, the amplitudes of the four-peak gap nematicon are the same for the input wave amplitudes a_{x0}=8.8 and a_{y0}=9.5. The amplitudes of multiple peaks in a four-peak gap nematicon vary as the amplitude or the intensity of the input wave changes, as shown in the first and third rows.

The above results show that the single-peak gap nematicons can be found for a wide range of propagation constants ranging from 1.2 to 1.8. Even when the amplitudes of the input waves change in these propagation constant ranges, multi-peak gap nematicons do not exist. The multi-peak gap nematicons exist only above a certain minimum value of the propagation constant. If the propagation constant is greater than a minimum value, then the variation of input wave amplitudes yields various profiles of multi-peak gap nematicons.

As the input beam intensity varies, the nonlocal response of the material can cause the redistribution of light energy among different peaks in the multi-peak gap nematicon. The nonlinear response of the nematic liquid crystal to the input beam intensity plays a significant role. At certain input intensities, nonlinear effects such as self-focusing can lead to the concentration of light energy into specific peaks, resulting in unequal peak amplitudes. However, at other intensities, the nonlinear response may favor a more uniform distribution of light energy among the peaks, resulting in equal peak amplitudes.

Both the single-peak and multi-peak gap nematicons offer a wide range of applications in areas such as optical communication, signal processing, imaging, and computing. Multi-peak gap nematicons inherently have more localized intensity peaks compared to single-peak gap nematicons. Each peak in a multi-peak gap nematicon can potentially carry independent information channels, thereby increasing the overall data-carrying capacity.

6.6 Linear stability analysis

The linear stability of the stationary states of the coupled system has been investigated using Bogoliubov-de Gennes (BDG) equations. For radial symmetry, consider small perturbations of the stationary states of the system in the form

$$X = R + a(r,z)e^{-i\mu z}, \qquad Y = S + b(r,z)e^{-i\mu z}, \tag{6.35}$$

where the perturbations are given by [20, 21]

$$a(r,z) = a_1(r)e^{i\lambda z} + a_2(r)e^{-i\lambda^* z}, \tag{6.36}$$

$$b(r,z) = b_1(r)e^{i\lambda z} + b_2(r)e^{-i\lambda^* z}, \tag{6.37}$$

the asterisk indicates the complex conjugation. The pair of coupled Equations (6.28) and (6.29) are linearized, assuming a_1, a_2, b_1, and b_2 are very small. This results in a set of four homogeneous equations that are satisfied by a_1, a_2, b_1, and b_2 and are shown in matrix form below:

$$\lambda \begin{pmatrix} a_1 \\ a_2^* \\ b_1 \\ b_2^* \end{pmatrix} = C \begin{pmatrix} a_1 \\ a_2^* \\ b_1 \\ b_2^* \end{pmatrix}, \tag{6.38}$$

where,

$$C = \begin{pmatrix} L_1 + V(r) & 0 & \frac{1}{4}e^{\frac{iz}{1+\gamma}} sin2\xi & \frac{R^2}{2} \\ \frac{R^2}{2} & -L_1 - V(r) & 0 & -\frac{1}{4}e^{\frac{-iz}{1+\gamma}} sin2\xi \\ \frac{1}{4\gamma}e^{\frac{-iz}{1+\gamma}} sin2\xi & \frac{S^2}{2} & L_2 + V(r) & 0 \\ 0 & -\frac{1}{4\gamma}e^{\frac{iz}{1+\gamma}} sin2\xi & \frac{S^2}{2} & -L_2 - V(r) \end{pmatrix}, \tag{6.39}$$

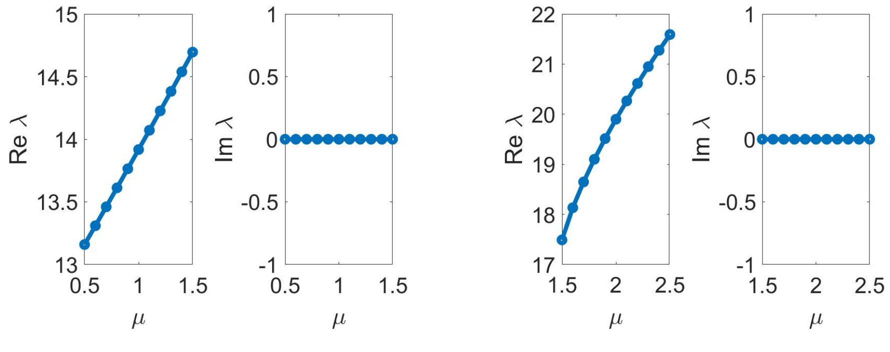

(a) (b)

Figure 6.7: The results of linear stability analysis of the system in a periodic potential with the strength of $V_0 = 1.7$. (a) Stability analysis of single-peak gap nematicons for a_{x0}=1.7, a_{y0}=2.0. (b) Stability analysis of two peak gap nematicons for a_{x0}=4.1, a_{y0}=4.8. The real and imaginary parts of the perturbation eigenvalues (λ) versus the propagation constant μ are shown.

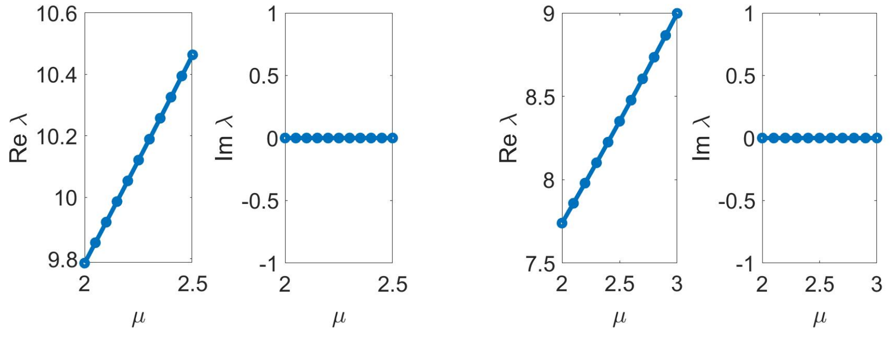

(a) (b)

Figure 6.8: The results of linear stability analysis of the system in a periodic potential with the strength of $V_0 = 1.7$. (a) Stability analysis of three peak gap nematicons for a_{x0}=4.5, a_{y0}=5.3. (b) Stability analysis of four peak gap nematicons for a_{x0}=8.8, a_{y0}=9.5. The real and imaginary parts of the perturbation eigenvalues (λ) versus the propagation constant μ are shown.

$$L_1 = \frac{1}{2}\left(\frac{d^2}{dr^2} + \frac{1}{r}\frac{d}{dr} + sin^2\xi + |R|^2 + 2\mu\right), \tag{6.40}$$

$$L_2 = \frac{1}{2\gamma}\left(\frac{d^2}{dr^2} + \frac{1}{r}\frac{d}{dr} - sin^2\xi + |S|^2 + 2\gamma\mu\right). \tag{6.41}$$

The system is solved using spectral methods based on Chebyshev polynomials. A grid that extends 40 along r is chosen to evaluate the diffraction operators.

The perturbation eigenvalues as functions of the propagation constants have been analyzed. The nature of the eigenvalue determines the stability of the solution. If all imaginary eigenvalues are equal to zero, the solutions are completely stable. That is when the system has only real eigenvalues of λ.

Figure (6.7) consists of stability plots for a periodic potential strength of $V_0 = 1.7$ for single-peak and two peak gap nematicons. Figure 6.7(a) depicts the stability analysis of single-peak gap nematicon, while Figure 6.7(b) depicts the stability analysis of two peak gap nematicon. Figure 6.7(a) illustrates that the magnitudes of imaginary eigenvalues are zero for a_{x0}=1.7, a_{y0}=2.0, and hence the corresponding solutions are linearly stable. Figure 6.7(b) shows that solutions are stable with purely real eigenvalues for a_{x0}=4.1, a_{y0}=4.8. This implies that the single-peak and two peak gap nematicons are stable.

Figure (6.8) shows stability plots for three and four-peak gap nematicons having the same amplitude peaks in a periodic potential strength of $V_0 = 1.7$. Figure 6.8(a) shows that for three peak gap nematicons with a_{x0}=4.5 and a_{y0}=5.3, the magnitudes of imaginary eigenvalues are zero, indicating that the corresponding solutions are linearly stable. Solutions with purely real eigenvalues are stable for four peak gap nematicons with a_{x0}=8.8, a_{y0}=9.5, as shown in Figure 6.8(b). This implies that the three and four-peak gap nematicons having all peaks with the same amplitudes are stable.

Stability plots for multi-peak gap nematicons in a periodic potential strength of $V_0 = 1.7$ are shown in Figure (6.9). The first row shows the stability plot for three peak gap nematicons, while the second shows the stability plots for four peak gap nematicons. The stability plots for the three peak gap nematicon with a_{x0}=4.1 and a_{y0}=4.9 are shown in Figure 6.9(a), and those for the three peak gap nematicon with a_{x0}=4.8 and a_{y0}=5.6 are shown in Figure 6.9(b). In Figures 6.9(c) and (d), the stability plots for four peak gap nematicons with a_{x0}=8.3, a_{y0}=9.0 and a_{x0}=9.6, a_{y0}=10.3 are respectively plotted. The magnitudes of imaginary

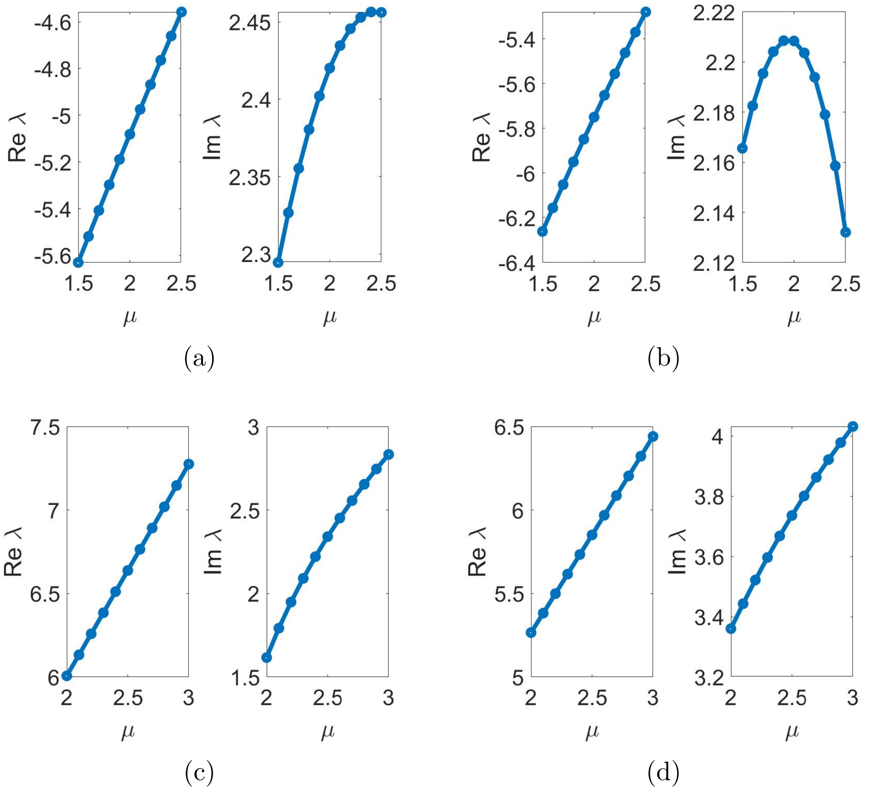

(a) (b)

(c) (d)

Figure 6.9: The results of linear stability analysis of the system in a periodic potential with the strength of $V_0 = 1.7$. Stability analysis of three peak gap nematicons for (a) a_{x0}=4.1, a_{y0}=4.9; (b) a_{x0}=4.8, a_{y0}=5.6. Stability analysis of four peak gap nematicons for (c) a_{x0}=8.3, a_{y0}=9.0; (d) a_{x0}=9.6, a_{y0}=10.3. The real and imaginary parts of the perturbation eigenvalues (λ) versus the propagation constant μ are shown.

eigenvalues are not zero in Figures 6.9(a)-(d), implying that the corresponding solutions are linearly unstable. This indicates that the multi-peak gap nematicons with unequal amplitudes among peaks are unstable.

According to linear stability analysis, single-peak gap nematicons are stable in the first band gap whereas multi-peak gap nematicons are only stable for a specific value of input wave amplitudes. Multi-peak gap nematicons with the same amplitudes among the peaks are stable, whereas those with unequal amplitudes among the peaks are unstable.

6.7 Conclusion

The formation and stability of single-peak and multi-peak gap nematicons have been numerically studied. Both the stationary and dynamic solutions of the system have been analyzed. Single-peak and multi-peak gap nematicons are observed in the first band gap. Single-peak gap nematicons are supported over a broad range of propagation constants, while multi-peak gap nematicons are only found above a specific threshold of the propagation constant. Once the propagation constant exceeds this threshold, varying the input wave amplitudes can yield different multi-peak gap nematicon profiles. A linear stability analysis has been employed to assess the stability of the stationary solutions under small perturbations. Single-peak gap nematicons are found to be stable. The multi-peak gap nematicons with equal peak amplitudes are stable, but those with unequal amplitudes are unstable.

The ability to generate and stabilize single-peak and multi-peak gap nematicons can be crucial for enhancing light propagation in optical fibers and waveguides. Single-peak nematicons, which are stable over a broad range of propagation constants, may be particularly useful for transmitting signals without distortion. Multi-peak gap nematicons with their dependence on input beam intensity, offer the potential for tunable signal transmission. Photonic crystals which rely on band gap engineering to control light, could benefit from the stable single-peak and multi-peak gap nematicons. These nematicons can enhance the performance of photonic devices by providing stable light confinement and guidance which is critical in developing highly efficient optical switches, filters, and sensors. The ability to control the intensity distribution in multi-peak gap nematicons suggests potential applications in laser systems where beam profile shaping is required. This could lead to improved laser beam control in applications such as precision machining, medical devices, or optical trapping. The stability and controllability of gap nematicons could also be relevant in the development of quantum communication and computing systems, where stable, controlled light propagation is crucial for maintaining coherence and reducing noise in quantum channels. In multi-peak gap nematicons, each peak represent a bit and so multi-peak structures helps to increase data carrying capacity. Multi-peak nematicons provide more the amount of data that can be sent in optical communications as compared to single-peak nematicons. That is, multi-peak nematicons have more data-carrying capacity, resulting in faster data transmission.

Building on the analysis of nematicons in a periodic potential, the next chapter investigates the combined effects of thermal response and diffractive radiation on beam propagation within this potential.

Bibliography

[1] Mills DL, Trullinger SE. Gap solitons in nonlinear periodic structures. Physical Review B. 1987 jul;36(2):947-52.

[2] Zeng L, Zeng J. Preventing critical collapse of higher-order solitons by tailoring unconventional optical diffraction and nonlinearities. Communications Physics. 2020 Jan;3(1):Article ID 26.

[3] Chen W, Mills DL. Gap solitons and the nonlinear optical response of superlattices. Physical Review Letters. 1987 jan;58(2):160-3.

[4] Zhang Y, Wang Z, Zheng H, Yuan C, Li C, Lu K, et al. Four-wave-mixing gap solitons. Physical Review A. 2010 nov;82(5):053837.

[5] Barashenkov IV, Pelinovsky DE, Zemlyanaya EV. Vibrations and Oscillatory Instabilities of Gap Solitons. Physical Review Letters. 1998 jun;80(23):5117-20.

[6] Ikeda T, Tsutsumi O, Sasaki T. Liquid crystal photonics: optical switching and image storage by means of nematic liquid crystals and ferroelectric liquid crystals. Synthetic Metals. 1996 aug;81(2-3):289-96.

[7] Garcìa CV, Garcilópez IP, Lallana PC, Vinouze B, Fracasso B. Liquid crystal optical switches. In: Optical Switches. Elsevier; 2010. p. 206-40.

[8] Hussein RA, Hameed MFO, Obayya SSA. Ultrahigh Soliton Pulse Compression Through Liquid Crystal Photonic Crystal Fiber. IEEE Journal of Selected Topics in Quantum Electronics. 2016 mar;22(2):302-9.

[9] Khoo IC. Extreme nonlinear optics of nematic liquid crystals [Invited]. Journal of the Optical Society of America B. 2011 Dec;28(12):A45.

[10] Sajitha NM, Suneera TP. Thermal response of nematicons in a parabolic potential. Physica Scripta. 2024 May;99(6):065567.

[11] Hällstig E, Lindgren M, Martin T, Sjöqvist L. Polarization properties of a nematic liquid-crystal spatial light modulator for phase modulation. Journal of the Optical Society of America A. 2005 Jan;22(1):177.

[12] Markos C, Travers JC, Abdolvand A, Eggleton BJ, Bang O. Hybrid photonic-crystal fiber. Reviews of Modern Physics. 2017 Nov;89(4):045003.

[13] Lu M. Nematic liquid-crystal technology for Si wafer-based reflective spatial light modulators. Journal of the Society for Information Display. 2002 Mar;10(1):37-47.

[14] Woltman SJ, Jay GD, Crawford GP. Liquid-crystal materials find a new order in biomedical applications. Nature Materials. 2007 Nov;6(12):929-38.

[15] Kwasny M, Laudyn UA, Sala FA, Alberucci A, Karpierz MA, Assanto G. Self-guided beams in low-birefringence nematic liquid crystals. Physical Review A. 2012 jul;86(1):013824.

[16] Sajitha NM, Suneera TP. Thermal response of single-peak and double-peak nematicons. The European Physical Journal Plus. 2023 Dec;138(12):Article ID 1073.

[17] Assanto G, Smyth NF. Spin-optical solitons in liquid crystals. Physical Review A. 2020 sep;102(3):033501.

[18] Aleksić NB, Petrović MS, Strinić AI, Belić MR. Solitons in highly nonlocal nematic liquid crystals: Variational approach. Physical Review A. 2012 mar;85(3):033826.

[19] Sajitha NM, Suneera TP. The effect of parabolic potential on the generation of higher harmonics of nematicons. Physica Scripta. 2023 Apr;98(5):055502.

[20] Kumar S, Perego A Staliunas K. Linear and Nonlinear Bullets of the Bogoliubov–de Gennes Excitations. Physical Review Letters. 2017 Jan;118(4):044103.

[21] Wang W, Kevrekidis PG, Carretero-González R, Frantzeskakis DJ. Dark spherical shell solitons in three-dimensional Bose-Einstein condensates: Existence, stability, and dynamics. Physical Review A. 2016 Feb;93(2):023630.

Chapter 7

Multi-Peak Gap Nematicons: Effects of Thermal Response and Diffractive Radiation

This chapter explores the influence of thermal response and diffractive radiation on multi-peak gap nematicons by employing numerical simulations. Both stationary and dynamic solutions are analyzed. The study shows that thermal response alone generates two-peak gap nematicons in the first band gap, with the peak separation increasing nonlinearly in a parabolic fashion as thermal response coefficients rise. When diffractive radiation is considered, three-peak and four-peak gap nematicons also emerge with energy dynamically redistributing among peaks based on the varying heights of the diffractive radiation shelf. The stability of these multi-peak structures under small perturbations is investigated. This research offers significant potential for applications in advanced photonic technologies, such as optical switching, beam shaping, and temperature sensing.

The results of this chapter are published as:

- N. M. Sajitha, T. P. Suneera, 'Unveiling the dynamics of multi-peak gap nematicons: Effects of thermal response and diffractive radiation'. Chaos. 2025 Mar; 35(3): 033149.

7.1 Introduction

Solitons in periodic media are a vibrant research topic in both science and engineering, recognized for their unique properties and diverse applications. A prominent example is gap solitons, which are localized structures formed in nonlinear media characterized by periodic variations in properties like refractive index, density, or potential. These solitons emerge from the interaction between nonlinearity and the band gap structure of the medium, residing spectrally within regions where linear wave propagation is prohibited [1]. Although they are extensively studied in optical systems, gap solitons are also found in other physical settings, such as Bose-Einstein condensates in optical lattices and acoustic waves in layered media [2, 3]. Their distinctive dynamics and adaptability offer exciting potential for advancements in photonic technologies and other fields. The previous chapter focused on the behavior and stability of multi-peak gap nematicons. In this chapter, we explore how multi-peak gap nematicons are affected by the combined influences of thermal response and diffractive radiation within a periodic potential. The interplay between thermal effects and diffractive radiation in shaping multi-peak gap nematicons is a relatively unexplored area with significant implications for optical solitons and photonics applications.

This chapter explores the impact of thermal response and diffractive radiation on multi-peak gap nematicons in the nonlocal regime. Numerical simulations are performed to analyze beam dynamics for varying thermal response coefficients and diffractive radiation shelf heights. The chapter is organized as follows: Section 7.2 introduces the modeling of beam dynamics in nematic liquid crystals with periodic potential and nonlocal nonlinearity. Section 7.3 delves into the band gap spectrum generated by the periodic potential for different thermal response coefficients and discusses stationary solutions. Section 7.4 addresses the propagation characteristics of multi-peak gap nematicons. Results and discussions are presented in section 7.5. This section analyzes beam behavior under two scenarios: one where the dynamics are influenced only by thermal response, and another where thermal response and diffractive radiation are considered together.

Section 7.6 provides a linear stability analysis to assess the stability of multi-peak gap nematicons under small perturbations. Finally, section 7.7 concludes the chapter.

7.2 Theoretical model

Consider a positive uniaxial NLC with its optic axis along the y-direction. When an optical beam propagates through the system along z - direction, the optic axis reorients in the $x - y$ plane. The angle ξ denotes the reorientation of the optic axis. The entire geometry is illustrated in Figure (7.1). The medium is modified such that the beam experiences periodic refractive index variations.

As the beam propagates through the medium absorption occurs, thereby localized heating. This causes thermo-optic changes in the optical properties of the NLC. The refractive indices $n_{\parallel}$ and $n_{\perp}$, which are parallel and perpendicular to the director alignment respectively, as well as the elastic constant K of the medium, become temperature-dependent when thermal effects on material properties are considered.

We have the heat flow equation as follows [4]

$$S\nabla^2 T = -\alpha\Gamma \mid E \mid^2, \qquad \text{where,} \quad \Gamma = \frac{1}{2}\epsilon_0 c n_e. \tag{7.1}$$

The letter S indicates thermal conductivity and α represents the absorption coefficient of the material. The temperature is denoted by T, ϵ_0 represents the permittivity of free space and c denotes the speed of light. n_e is the refractive index of the extraordinariy polarized waves and is given by

$$n_e^2 = \frac{n_{\parallel}^2 n_{\perp}^2}{n_{\parallel}^2 cos^2\xi + n_{\perp}^2 sin^2\xi}. \tag{7.2}$$

Assume that the temperature of the NLC is T_0 initially. When the optical beam passes through the medium, the temperature is increased by A_T due to the absorption of light. Now, the dimensionless temperature change is represented by

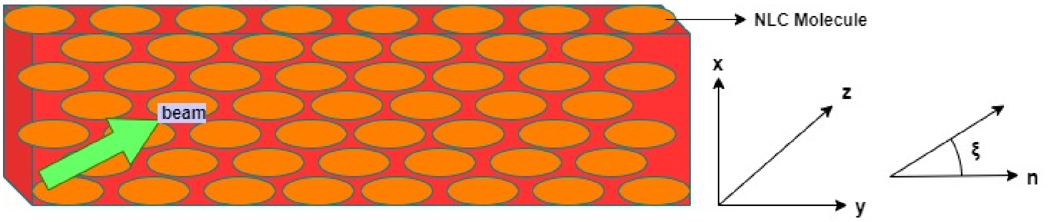

Figure 7.1: The considered geometry. The NLC molecules are depicted with ellipses and their long axes along y. The input beam is displayed in a green arrow, hitting normally on the molecular director. The angle ξ represents the director angle [5].

$T = T_0 + A_T\tau$. The non-dimensional form of the heat equation is given as

$$\mu_T \nabla^2 \tau = - \mid X \mid^2 - \mid Y \mid^2, \qquad \text{where,} \quad \mu_T = \frac{SA_T}{\alpha \Gamma W_b^2 A_b^2}, \tag{7.3}$$

where μ_T is the thermal diffusivity [6], A_b and W_b denote the amplitude and width of the input wave packet.

The system is modeled using a nonlinear Schrodinger equation with a periodic potential, with the behavior of the molecular director described by an elliptic Poisson equation. Incorporating thermal effects on the properties of the NLC, the governing equations for the system are given by

$$2i\frac{\partial X}{\partial z} + \frac{\partial^2 X}{\partial x^2} + \frac{\partial^2 X}{\partial y^2} + X sin^2\xi + \frac{1}{2} Y e^{\frac{iz}{1+\gamma(\tau)}} sin2\xi + V(x,y)X = 0, \tag{7.4}$$

$$\begin{aligned} 2i\gamma(\tau)\frac{\partial Y}{\partial z} + \frac{\partial^2 Y}{\partial x^2} + \frac{\partial^2 Y}{\partial y^2} - Y sin^2\xi + \frac{1}{2} X e^{\frac{-iz}{1+\gamma(\tau)}} sin2\xi \\ -V(x,y)Y = 0, \end{aligned} \tag{7.5}$$

$$\nu(\tau)\nabla^2\xi + (\mid X \mid^2 - \mid Y \mid^2) sin2\xi + 2Re(XY^* e^{\frac{-iz}{1+\gamma(\tau)}}) cos2\xi = 0. \tag{7.6}$$

Here, $V(x,y) = V_0 \; cos^2\left(\sqrt{x^2+y^2}\right)$, denotes the periodic potential of period π and a strength V_0. Electric field amplitudes in two transverse directions are represented by X and Y. z denotes the propagation distance.

Both the nonlocality (ν) and anisotropy (γ) depend on temperature. The following equations relate nonlocality ν to the elastic constant K and anisotropy γ to the extra-ordinary refractive index n_e [4],

$$\nu = \frac{8K}{\epsilon_0 \epsilon_a A_b^2 W_b^2 sin 2\xi}, \quad \gamma = \frac{2n_e}{\sqrt{\epsilon_a sin 2\xi}}, \tag{7.7}$$

where, K represents the elastic constant of the medium, which is considered to be the same for bend, splay, and twist deformations of the NLC molecules [7].

Continuous-wave lasers in the visible to near-infrared region with power levels typically in the milliwatt range would be suitable for the experimental realization of this study. Our findings indicate that the beam power required to generate two-peak, three-peak, and four-peak gap nematicons is approximately 40 mW, 55 mW, and 180 mW, respectively. A coherent and polarized Gaussian beam is launched with a plane wavefront, having a waist of 12 μm at the origin of a planar cell of size L= 200 μm along the x-axis. The various constants used in the model are chosen based on the material properties of the standard E7 mixture at room temperature. This mixture is a positive uniaxial NLC with refractive indices $n_{\|}$=1.73 and $n_{\perp}$=1.53, and an elastic constant of K=12 pN [7]. These parameters are employed in the computational analysis to simulate the beam dynamics and nonlinear effects in the system.

Experimental results show that the refractive index eigenvalues of the NLC mixture E7 change almost linearly with temperature up to 40^0C [4]. Between 20 and 40 degrees Celsius, the refractive index $n_{\|}$ decreases by approximately 0.6%, whereas the refractive index $n_{\perp}$ increases by approximately 1.3% [4, 8]. Thus, $\gamma(\tau) = 1 - \gamma_1 \tau$, where γ_1 is correlated with $\frac{d\gamma}{d\tau}$ at $T = T_0$. The dependence of temperature on nonlocality, ν is minimal [6].

The heat Equation (7.3) has two homogeneous solutions, $\ln r$ and a constant. Because of the high thermal diffusivity μ_T, we suppose that the temperature inside the circular peak of nematicon is constant. Temperature decreases as the homogeneous solution goes away from the axis.

$$\tau = \tau_0, \quad 0 \le r \le m; \qquad \tau = \tau_1 \ln \frac{R}{r}, \quad m < r < R. \tag{7.8}$$

Also, it follows the boundary condition $\tau= 0$ at $r = R$.

In E7 NLCs, thermal response coefficient values can vary from 0 to 1.8, a range that allows for detailed investigation of thermal effects on nematicon dynamics and stability [4].

To study beam dynamics with thermal response and diffractive radiation in a periodic potential, the trial functions for Equations (7.4) and (7.5) are expressed as

$$X = \left[a_x \left(e^{\frac{-(r-m)^2}{w_x^2}} + e^{\frac{-(r+m)^2}{w_x^2}}\right) + ig_x\right] e^{i\sigma_x}, \tag{7.9}$$

$$Y = \left[a_y \left(e^{\frac{-(r-m)^2}{w_y^2}} + e^{\frac{-(r+m)^2}{w_y^2}}\right) + ig_y\right] e^{i\sigma_y}. \tag{7.10}$$

The beam amplitudes are a_x and a_y, the widths are w_x and w_y, and the phases in the two transverse directions are σ_x and σ_y respectively. Here, g_x and g_y denote the heights of the diffractive radiation shelf along the x and y axes, respectively.

As the beam components propagate, they experience oscillations that lead to the generation of diffractive radiation, which manifests as a radiation "shelf" beneath the beam. These shelf terms, denoted as ig_x and ig_y, represent the long-wavelength radiation produced near the beam. When g_x=0 and g_y=0, the solution gives the thermal response of the system.

The solution of Equation (7.6) is chosen as [5, 9, 10],

$$\xi = \alpha e^{\frac{-r^2}{\beta^2}} + A\left[Ei\left(\frac{-r^2}{\beta^2}\right) - ln\left(\frac{r^2}{d^2}\right)\right]. \tag{7.11}$$

In Equation (7.11), the first term corresponds to the local contribution with the amplitude α, while the second and third terms indicate the nonlocal contributions having amplitude A and width β. The following relation shows how α depends on the propagation distance z,

$$\alpha = \frac{2}{D} \frac{a_x a_y w_x^2 w_y^2 \beta^2 cos\theta}{\nu - \beta^2 \Delta}, \tag{7.12}$$

where,

$$D = \beta^2 w_x^2 + \beta^2 w_y^2 + w_x^2 w_y^2, \quad \theta = \frac{z}{1+\gamma} - \sigma_x + \sigma_y, \qquad \text{and}$$
$$\Delta = \frac{a_x^2 w_x^2}{\beta^2 + w_x^2} - \frac{a_y^2 w_y^2}{\beta^2 + w_y^2}. \tag{7.13}$$

β is provided by the equation, β=$L/(2\ln 100)$. Assuming L is the thickness of the NLC, $d = L/2$. Ei represents the exponential integral function.

$$E_i = -\int_{-z}^{+\infty} e^{-t} t^{-1} dt. \tag{7.14}$$

7.3 Band gap spectrum and stationary solutions

7.3.1 Band gap spectrum

Assuming solutions of Equations (7.4) - (7.6) can be expressed in terms of the propagation constant μ,

$$X(x,y,z) \;= P(x,y)e^{-i\mu z}, \qquad Y(x,y,z) \;= Q(x,y)e^{-i\mu z}, \tag{7.15}$$

yield steady-state equations,

$$\frac{\partial^2 P}{\partial x^2} + \frac{\partial^2 P}{\partial y^2} + Psin^2\xi + \frac{1}{2}Qe^{\frac{iz}{1+\gamma(\tau)}}sin2\xi + V(x,y)P = -2\mu P, \tag{7.16}$$

$$\frac{\partial^2 Q}{\partial x^2} + \frac{\partial^2 Q}{\partial y^2} - Qsin^2\xi + \frac{1}{2}Pe^{\frac{-iz}{1+\gamma(\tau)}}sin2\xi - V(x,y)Q = -2\mu\gamma(\tau)Q, \tag{7.17}$$

$$\nu(\tau)\nabla^2\xi + (|P|^2 - |Q|^2)sin2\xi + 2Re(PQ^* e^{\frac{-iz}{1+\gamma(\tau)}})cos2\xi = 0. \tag{7.18}$$

Because the potential is periodic, the system can support Bloch waves, which take the form:

$$P(x,y) \;= P_k(x,y)e^{i(kx+ky)}, \qquad Q(x,y) \;= Q_k(x,y)e^{i(kx+ky)}. \tag{7.19}$$

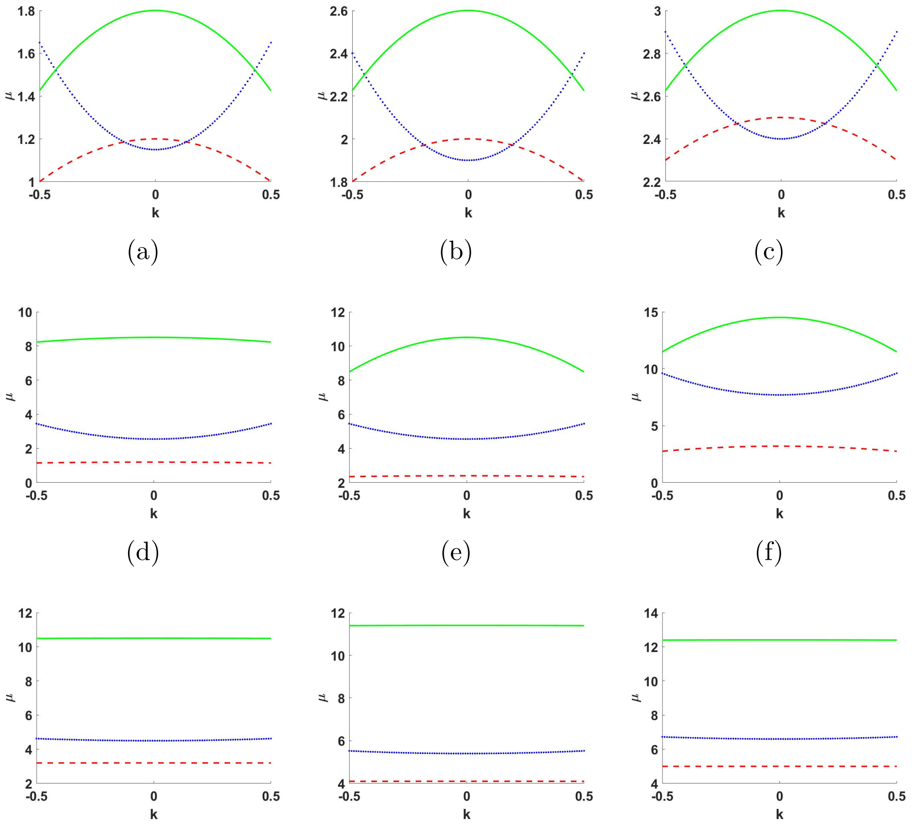

(a) (b) (c)

(d) (e) (f)

(g) (h) (i)

Figure 7.2: Band gap spectrum - The eigenvalue μ versus Bloch momentum k, with the first band in red dashed line, the second band in blue dotted line, and the third band in green solid line. First row for $V_0 = 1.0$: (a) $\tau_0 = \tau_1 = 0$; (b) $\tau_0 = \tau_1 = 0.8$; (c) $\tau_0 = \tau_1 = 1.6$. Second row for $V_0 = 1.7$: (d) $\tau_0 = \tau_1 = 0$; (e) $\tau_0 = \tau_1 = 0.8$; (f) $\tau_0 = \tau_1 = 1.6$. Third row for $V_0 = 2.4$: (g) $\tau_0 = \tau_1 = 0$; (h) $\tau_0 = \tau_1 = 0.8$; (i) $\tau_0 = \tau_1 = 1.6$.

Let k denotes the Bloch momentum, which satisfies the periodic boundary condition:

$$P_k(x+\pi, y) \; = P_k(x, y), \qquad Q_k(x, y+\pi) \; = Q_k(x, y). \tag{7.20}$$

The Bloch solutions fulfill the equation:

$$\begin{aligned} \frac{\partial^2 P_k}{\partial x^2} + \frac{\partial^2 P_k}{\partial y^2} - 2k^2 P_k + P_k sin^2\xi + \frac{1}{2} Q_k e^{\frac{iz}{1+\gamma(\tau)}} sin2\xi & \\ + V(x, y) P_k = -2\mu P_k, & \end{aligned} \tag{7.21}$$

$$\frac{\partial^2 Q_k}{\partial x^2}+\frac{\partial^2 Q_k}{\partial y^2}-(1+\gamma(\tau)^2)k^2Q_k-Q_k sin^2\xi+\frac{1}{2}P_k e^{\frac{-iz}{1+\gamma(\tau)}} sin2\xi$$
$$-V(x,y)Q_k=-2\mu\gamma(\tau)Q_k, \qquad (7.22)$$

$$\nu(\tau)\nabla^2\xi+(|P_k|^2-|Q_k|^2)sin2\xi+2Re(P_kQ_k^*e^{\frac{-iz}{1+\gamma(\tau)}})cos2\xi=0. \qquad (7.23)$$

This study concentrates on solutions with radial symmetry, and therefore, Equations (7.21) – (7.23) are reformulated using radial coordinates as follows:

$$\frac{\mathrm{d}^2 P_k}{\mathrm{d}r^2}+\frac{1}{r}\frac{\mathrm{d}P_k}{\mathrm{d}r}-2k^2P_k+P_k sin^2\xi+\frac{1}{2}Q_k e^{\frac{iz}{1+\gamma(\tau)}} sin2\xi$$
$$+V(r)P_k=-2\mu P_k, \qquad (7.24)$$

$$\frac{\mathrm{d}^2 Q_k}{\mathrm{d}r^2}+\frac{1}{r}\frac{\mathrm{d}Q_k}{\mathrm{d}r}-(1+\gamma(\tau)^2)k^2Q_k-Q_k sin^2\xi+\frac{1}{2}P_k e^{\frac{-iz}{1+\gamma(\tau)}} sin2\xi$$
$$-V(r)Q_k=-2\mu\gamma(\tau)Q_k, \qquad (7.25)$$

$$\nu(\tau)\frac{\mathrm{d}^2\xi}{\mathrm{d}r^2}+\frac{\nu(\tau)}{r}\frac{\mathrm{d}\xi}{\mathrm{d}r}+(|P_k|^2-|Q_k|^2)sin2\xi$$
$$+2Re(P_kQ_k^*e^{\frac{-iz}{1+\gamma(\tau)}})cos2\xi=0. \qquad (7.26)$$

The periodic potential in radial coordinates is expressed as $V(r) = V_0\ cos^2 r$, where V_0 denotes the strength of the periodic potential. The eigenvalues are calculated for Bloch momentum k with varying strength of the periodic potential and different thermal response coefficients. To analyze the stability region of nematicons, we investigated their behavior across varying periodic potential strengths, V_0, from 0.1 to 3.0. Our analysis reveals distinct transitions in the band structure as V_0 varies.

Figure (7.2) depicts a band gap spectrum containing three bands, with the first band shown in a red dashed line, the second in a blue dotted line, and the third in a green solid line. The first row gives the band gap spectrum for a potential strength of $V_0 = 1.0$ with varying thermal response coefficients. Figures 7.2(a)-(c) shows the band gap spectrum for $\tau_0 = \tau_1 = 0$, $\tau_0 = \tau_1 = 0.8$, and

$\tau_0 = \tau_1 = 1.6$ respectively. The results indicate that the bands overlap and shift upward as the thermal response coefficients increase. When V_0 varies from 0.1 to 1.3, overlapping bands dominate, indicating weak localization and potential instability due to significant diffraction effects. This means that at lower V_0, band overlap makes it difficult to distinguish between modes.

The second row of Figure (7.2) depicts the band gap spectrum for a potential strength of $V_0 = 1.7$ with different thermal response coefficients. As shown in Figures 7.2(d)-(f), well-separated bands begin to emerge. In Figure 7.2(d), the first finite band gap covers an interval of $1.199 \leq \mu \leq 2.55$, and the second band gap spans an interval of $3.45 \leq \mu \leq 8.2$ with $\tau_0 = \tau_1 = 0$. In Figure 7.2(e), the first finite band gap encompasses an interval of $2.39 \leq \mu \leq 4.55$, and the second band gap extends over an interval of $5.41 \leq \mu \leq 10.49$ with $\tau_0 = \tau_1 = 0.8$. In Figure 7.2(f), the first finite band gap occupies an interval of $3.19 \leq \mu \leq 7.7$, and the second band gap ranges from $9.6 \leq \mu \leq 14.49$ with $\tau_0 = \tau_1 = 1.6$. For $V_0 = 1.4$ to $V_0 = 2.3$, well-separated bands emerge, revealing a stable regime with better confinement. Stable gap nematicon solutions were confirmed in this range.

The third row of Figure (7.2) shows the band gap spectrum for a potential strength of $V_0 = 2.4$ with different thermal response coefficients. As shown in Figures 7.2(g)-(i), more bands flatten at this potential strength and shift to higher μ values as the thermal response coefficients increase. Similarly, for V_0 ranging from 2.4 to 3.0, the bands continue to flatten and shift upward with increasing thermal response coefficients.

As V_0 varies the characteristics of nematicons may change due to modifications in the effective potential landscape. This study focuses on $V_0 = 1.7$ due to the well-separated band structure observed at this value, which facilitates the clear identification of stable numerical solutions. Our study primarily investigates how the band gap at this potential strength varies with thermal effects. A detailed investigation, including a complete stability boundary analysis for different potential strengths considering thermal response and diffractive radiation, may yield interesting results and will be pursued in our future work.

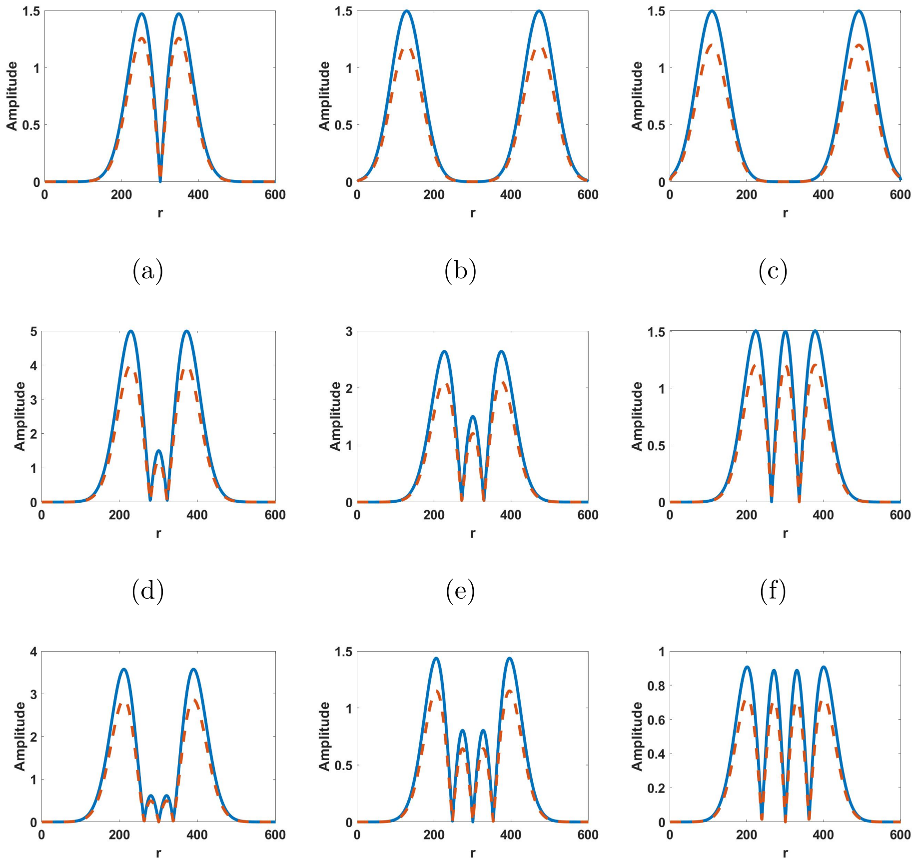

(a) (b) (c)

(d) (e) (f)

(g) (h) (i)

Figure 7.3: Stationary states in a periodic potential with strength $V_0 = 1.7$. P blue (solid) line and Q red (dashed) line. First row: Two-peak gap nematicon for a_{x0}=4.8, a_{y0}=4.1 with g_x=g_y=0. (a) $\tau_0 = \tau_1 = 0$; (b) $\tau_0 = \tau_1 = 0.8$; (c) $\tau_0 = \tau_1 = 1.6$. Second row: Three-peak gap nematicon for a_{x0}=5.6, a_{y0}=4.8 with $\tau_0 = \tau_1 = 0.8$. (d) g_x=g_y=0.5; (e) g_x=g_y=1.5; (f) g_x=g_y=3.8. Third row: Four-peak gap nematicon for a_{x0}=9.8, a_{y0}=9.1 with $\tau_0 = \tau_1 = 1.6$. (g) g_x=g_y=2.0; (h) g_x=g_y=5; (i) g_x=g_y=8.6.

7.3.2 Stationary solutions

Take into account the cylindrical symmetry of the uniaxial NLC. Furthermore, the system is considered to have a rotational symmetry about the propagation direction z. Then, $x^2 + y^2 = r^2$ and $\nabla^2 = \frac{1}{r}\frac{\partial}{\partial r} + \frac{\partial^2}{\partial r^2}$. The stationary differential Equations (7.16) - (7.18) becomes,

$$\frac{\mathrm{d}^2P}{\mathrm{d}r^2}+\frac{1}{r}\frac{\mathrm{d}P}{\mathrm{d}r}+Psin^2\xi+\frac{1}{2}Qe^{\frac{iz}{1+\gamma(\tau)}}sin2\xi+V(r)P=-2\mu P, \tag{7.27}$$

$$\frac{\mathrm{d}^2Q}{\mathrm{d}r^2}+\frac{1}{r}\frac{\mathrm{d}Q}{\mathrm{d}r}-Qsin^2\xi+\frac{1}{2}Pe^{\frac{-iz}{1+\gamma(\tau)}}sin2\xi-V(r)Q=-2\mu\gamma(\tau)Q, \tag{7.28}$$

$$\begin{aligned}\nu(\tau)\frac{\mathrm{d}^2\xi}{\mathrm{d}r^2}+\frac{\nu(\tau)}{r}\frac{\mathrm{d}\xi}{\mathrm{d}r}+(|P|^2-|Q|^2)sin2\xi&\\ +2Re(PQ^*e^{\frac{-iz}{1+\gamma(\tau)}})cos2\xi=0.&\end{aligned} \tag{7.29}$$

The numerical analysis of Equations (7.27) - (7.29) has been conducted using the finite difference method, and Figure (7.3) shows the amplitudes of the stationary solutions P and Q for various thermal response coefficient values within the first band gap in a periodic potential with strength V_0=1.7. In the first band gap, the thermal response alone produces two-peak gap nematicons for an initial excitation with a_{x0}=4.8, a_{y0}=4.1, w_{x0}=12, w_{y0}=12, σ_{x0}=0, σ_{y0}=0, g_x=0, and g_y=0. The impact of thermal response on the propagation of these two-peak gap nematicons has been analyzed in detail. When thermal response coefficients are zero and the propagation constant $\mu = 1.9$, the peak separation is 102, as shown in Figure 7.3(a). As the thermal response coefficients increase to $\tau_0 = \tau_1 = 0.8$, with the propagation constant $\mu = 2.4$, the peak separation widens to 270, as depicted in Figure 7.3(b). With a further increase to $\tau_0 = \tau_1 = 1.6$ and the propagation constant $\mu = 3.3$, the peak separation reaches 382, as seen in Figure 7.3(c).

The nonlinear parabolic increase in peak separation of two-peak gap nematicons with increase in thermal response coefficients is due to heat-induced refractive index changes in nematic liquid crystals. As the thermal response coefficient grows, temperature variations more strongly affect molecular alignment, amplifying refractive index modulation. This modulation broadens the optical waveguide around the nematicon, reducing confinement and leading to greater separation between the peaks.

When diffractive radiation is considered along with thermal effects, three-peak and four-peak gap nematicons can be found in the first band gap in a periodic potential with strength $V_0 = 1.7$. The second and third rows of Figure (7.3) show the three-peak and four-peak gap nematicons for $\tau_0 = \tau_1 = 0.8$ and $\tau_0 = \tau_1 = 1.6$, respectively. The second row gives the three-peak gap nematicon for an initial excitation with a_{x0}=5.6, a_{y0}=4.8, w_{x0}=12, w_{y0}=12, σ_{x0}=0, and σ_{y0}=0. Figures 7.3(d)-(f) depict the three-peak gap nematicons with a propagation constant of $\mu = 3.6$ and diffractive radiation shelf heights g_x=g_y=0.5, g_x=g_y=1.5, and g_x=g_y=3.8, respectively. The third row gives the four-peak gap nematicon for an initial excitation with a_{x0}=9.8, a_{y0}=9.1, w_{x0}=12, w_{y0}=12, σ_{x0}=0, and σ_{y0}=0. Figures 7.3(g)-(i) depict the four-peak gap nematicons with a propagation constant of $\mu = 6.4$ and diffractive radiation shelf heights g_x=g_y=2.0, g_x=g_y=5.0, and g_x=g_y=8.6, respectively. The second and third rows of Figure (7.3) show energy redistribution among the peaks with varying levels of diffractive radiation shelf heights.

7.4 Propagation dynamics of gap nematicons

The dynamic solution of the Equations (7.4) – (7.6) are analyzed in terms of the propagation constant μ as

$$X(x,y,z) \;= R(x,y,z)e^{-i\mu z}, \qquad Y(x,y,z) \;= S(x,y,z)e^{-i\mu z}. \tag{7.30}$$

Substituting X and Y in Equations (7.4) - (7.6) yields the nonlinear eigenvalue problem as

$$2i\frac{\partial R}{\partial z} + \frac{\partial^2 R}{\partial x^2} + \frac{\partial^2 R}{\partial y^2} + Rsin^2\xi + \frac{1}{2}Se^{\frac{iz}{1+\gamma(\tau)}}sin2\xi \\ +V(x,y)R = -2\mu R, \tag{7.31}$$

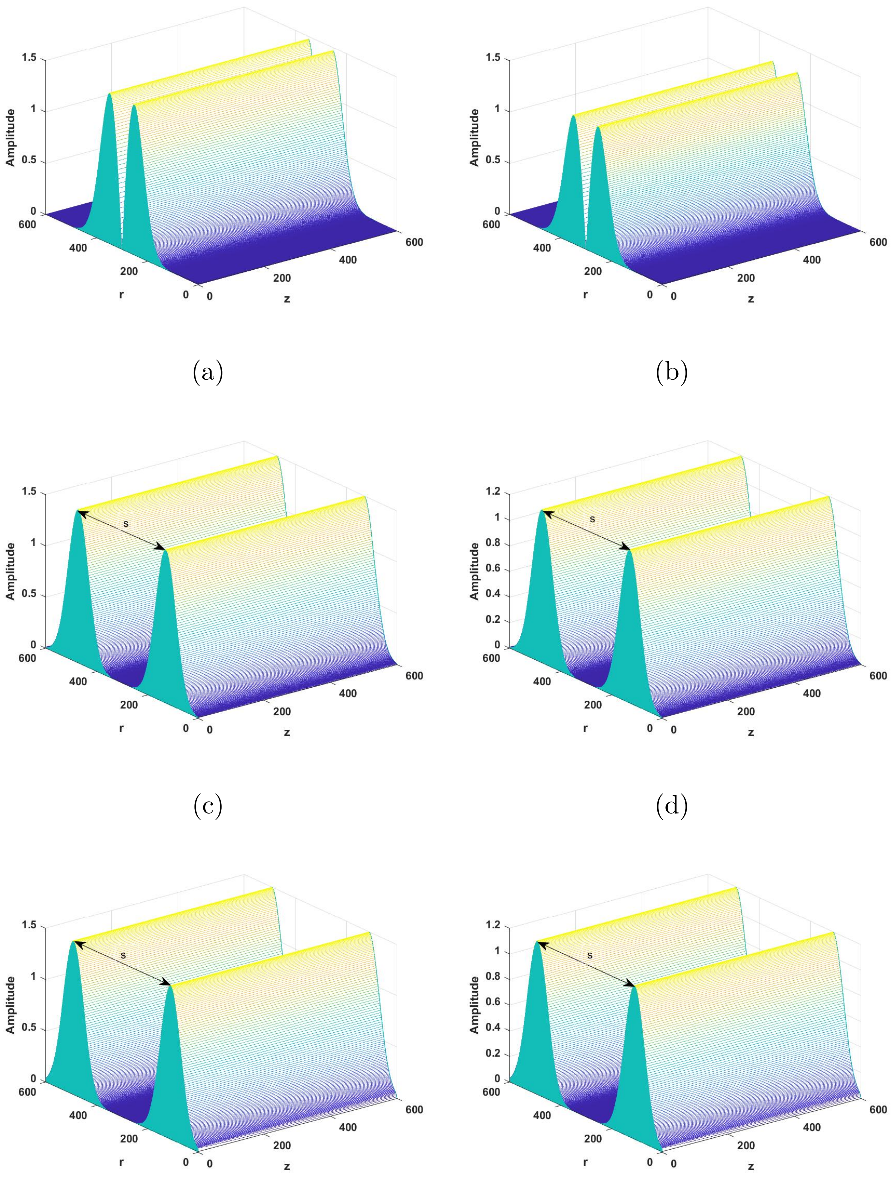

(a) (b)

(c) (d)

(e) (f)

Figure 7.4: Evolution of a two-peak gap nematicon for an initial excitation with a_{x0}=4.8, a_{y0}=4.1, w_{x0}=12, w_{y0}=12, σ_{x0}=0, σ_{y0}=0, g_x=0, and g_y=0 in a periodic potential with strength $V_0 = 1.7$. First column [(a), (c), (e)]: Evolution of R. Second column [(b), (d), (f)]: Evolution of S. First raw: $\tau_0 = \tau_1 = 0$ and $\mu = 1.9$. Second raw: $\tau_0 = \tau_1 = 0.8$ and $\mu = 2.4$. Third raw: $\tau_0 = \tau_1 = 1.6$ and $\mu = 3.3$.

Thermal response coefficients	Separation
0.0	102
0.2	149
0.4	193
0.6	233
0.8	270
1.0	303
1.2	332
1.4	358
1.6	382
1.8	398

Table 7.1: Thermal response coefficients and the corresponding seperation between peaks of two-peak gap nematicon.

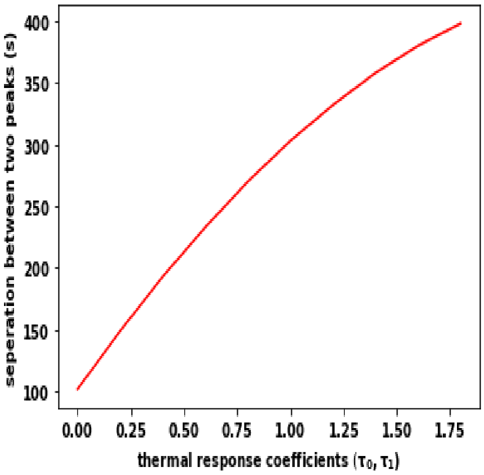

Figure 7.5: The thermal response coefficients versus separation between peaks of two-peak gap nematicon.

$$2i\gamma(\tau)\frac{\partial S}{\partial z}+\frac{\partial^2 S}{\partial x^2}+\frac{\partial^2 S}{\partial y^2}-Ssin^2\xi+\frac{1}{2}Re^{\frac{-iz}{1+\gamma(\tau)}}sin2\xi$$
$$-V(x,y)S=-2\mu\gamma(\tau)S, \quad (7.32)$$

$$\nu(\tau)\nabla^2\xi+(|R|^2-|S|^2)sin2\xi+2Re(RS^*e^{\frac{-iz}{1+\gamma(\tau)}})cos2\xi=0. \quad (7.33)$$

For radial symmetry, the Equations (7.31) - (7.33) becomes

$$2i\frac{\partial R}{\partial z}+\frac{\partial^2 R}{\partial r^2}+\frac{1}{r}\frac{\partial R}{\partial r}+Rsin^2\xi+\frac{1}{2}Se^{\frac{iz}{1+\gamma(\tau)}}sin2\xi$$
$$+V(r)R=-2\mu R, \quad (7.34)$$

$$2i\gamma(\tau)\frac{\partial S}{\partial z}+\frac{\partial^2 S}{\partial r^2}+\frac{1}{r}\frac{\partial S}{\partial r}-Ssin^2\xi+\frac{1}{2}Re^{\frac{-iz}{1+\gamma(\tau)}}sin2\xi$$
$$-V(r)S=-2\mu\gamma(\tau)S, \quad (7.35)$$

$$\nu(\tau)\frac{\partial^2\xi}{\partial r^2}+\frac{\nu(\tau)}{r}\frac{\partial\xi}{\partial r}+(|R|^2-|S|^2)sin2\xi$$
$$+2Re(RS^*e^{\frac{-iz}{1+\gamma(\tau)}})cos2\xi=0. \quad (7.36)$$

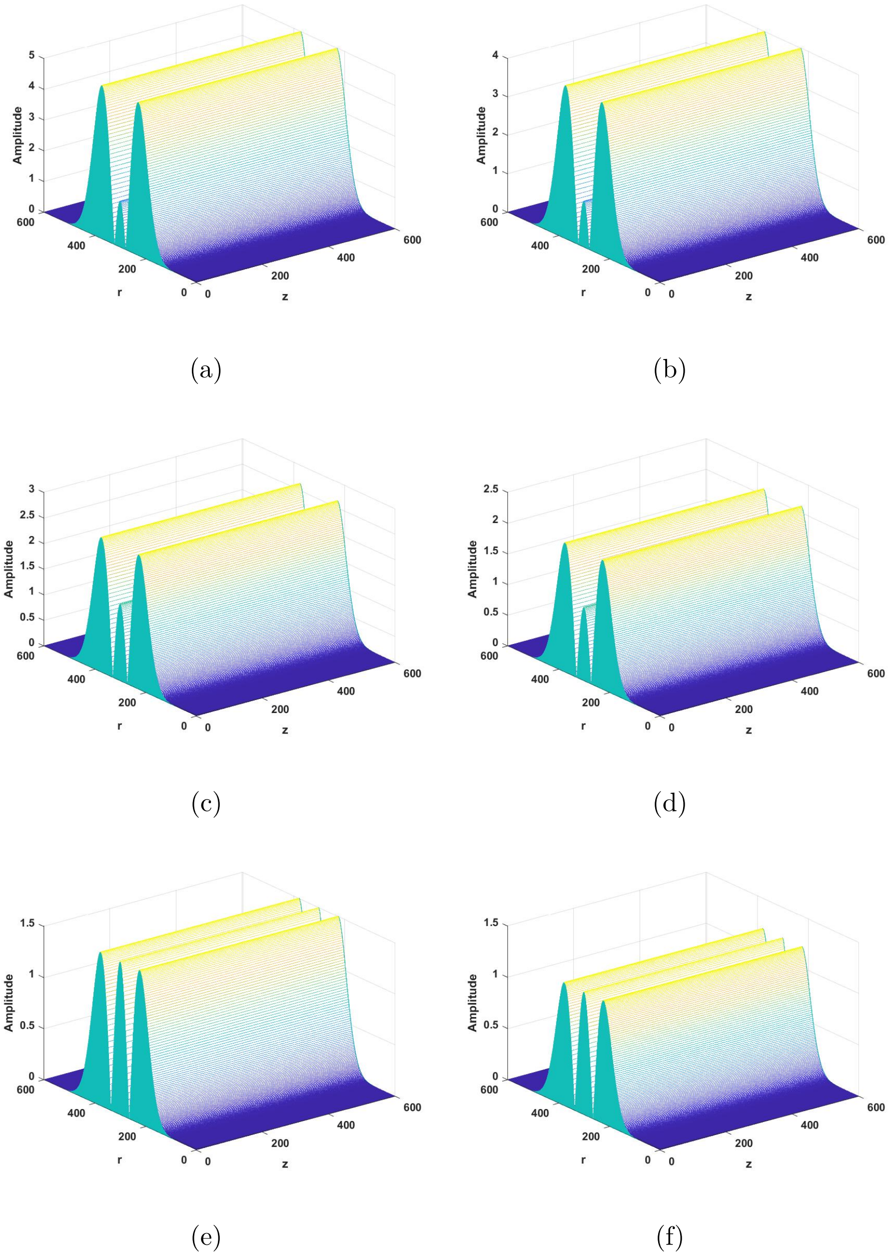

(a) (b)

(c) (d)

(e) (f)

Figure 7.6: Evolution of a three-peak gap nematicon for an initial excitation with a_{x0}=5.6, a_{y0}=4.8, w_{x0}=12, w_{y0}=12, σ_{x0}=0, and σ_{y0}=0 in a periodic potential with strength $V_0 = 1.7$. First column [(a), (c), (e)]: Evolution of R. Second column [(b), (d), (f)]: Evolution of S. First row: g_x=g_y=0.5. Second row: g_x=g_y=1.5. Third row: g_x=g_y=3.8. In all three rows, $\tau_0 = \tau_1 = 0.8$ and $\mu = 3.6$.

The Equations (7.34) - (7.36) are solved numerically by employing the finite difference method. In this method, a rectangular grid is applied with a separation of grid planes by Δz and Δr such that $z_k = k\Delta z$ and $r_n = n\Delta r$. The stability of the method requires $\frac{\Delta z}{\Delta r^2} \leq 0.5$. Section 7.5 graphically presents the numerical results of Equations (7.34) - (7.36).

7.5 Results and discussions

This work utilizes the finite difference method to analyze the effects of thermal response and diffractive radiation on the dynamics of multi-peak gap nematicons. The numerical solutions of Equations (7.34) - (7.36) are investigated under two conditions: with thermal response only, and with both thermal response and diffractive radiation. The strength of the potential is assumed to be $V_0 = 1.7$ throughout the analysis. The initial conditions are w_{x0}=12, w_{y0}=12, σ_{x0}=0, and σ_{y0}=0. The different variables are selected as $\mu_T = 300$, $\nu = 600$, $\gamma_1 = 0.1$, $\alpha = 2$, $A = 0.5$, and $m = 2.2$.

7.5.1 Thermal response only

Figure (7.4) depicts the evolution of the two-peak gap nematicons with a_{x0}=4.8, a_{y0}=4.1, g_x=0, and g_y=0 for varying thermal response coefficients. Figure 7.4(a,b) represents the evolution of the dynamic solutions R and S of Equations (7.34) - (7.36) with the propagation constant $\mu = 1.9$ and shows that the separation between peaks is about 102 for $\tau_0 = \tau_1 = 0$. When the thermal response coefficients are $\tau_0 = \tau_1 = 0.8$ and the propagation constant $\mu = 2.4$, the evolutions of the beam are depicted in second row of Figure (7.4). Figure 7.4(c,d) shows that the separation between peaks is around 270.

The advancement of amplitudes R and S for $\tau_0 = \tau_1 = 1.6$ and the propagation constant $\mu = 3.3$ is depicted in the third row of Figure (7.4). Figure 7.4(e,f) illustrates that two-peak gap nematicons have a peak separation of about 382. As the thermal response coefficients rise from 0 to 0.8 to 1.6, the separation between the peaks increases from 102 to 270 to 382. This change happens because the increased thermal response coefficients raise the temperature near the nematicon, enhancing the refractive index variation and widening the optical waveguide. Consequently, the two peaks become less confined, leading to a greater separation as the thermal response coefficients increase. The analysis has been carried out for thermal response coefficients ranging from 0 to 1.8 in a periodic potential strength of $V_0 = 1.7$. Numerical methods reveal two-peak gap nematicons, and we found that the separation between peaks increases nonlinear parabolic manner with increasing thermal response coefficients.

Table (7.1) shows the thermal response coefficients and the corresponding separation between peaks of two-peak gap nematicon in a periodic potential with a strength of $V_0 = 1.7$. The relationship between thermal response coefficients and the separation between peaks is depicted in Figure (7.5). The separation between peaks increases in a nonlinear parabolic manner with increasing thermal response coefficients.

From the above results, the two-peak gap nematicons can be found for a wide range of thermal response coefficients ranging from 0 to 1.8 in a periodic potential with a strength of V_0=1.7. As thermal response coefficients increase, the separation between peaks increases in a nonlinear parabolic manner. The increase in the separation between the peaks of a two-peak gap nematicon with higher thermal response coefficients can be understood through the interplay between thermal effects and refractive index changes in the nematic liquid crystal medium. Physically, the thermal response coefficient reflects the degree to which the refractive index of the medium changes in response to localized heating. When light propagates through the medium, it induces localized heating due to absorption. As the thermal response coefficient increases, the heating effect becomes more pronounced, leading to a stronger alteration of the refractive index around the nematicon. This localized change in refractive index acts like a thermal lens, broadening the spatial extent of the light field. In the case of a two-peak gap nematicon, the increased thermal response causes a greater divergence of the intensity distribution of light, pushing the two peaks farther apart. Essentially, the increased thermal effect weakens the nonlinear self-focusing between the peaks, allowing them to separate more as the refractive index gradient becomes more significant. The separation continues to grow in a parabolic manner up to a thermal response coefficient of $\tau_0 = \tau_1 = 1.8$, beyond which the two-peak gap nematicon becomes unstable and can no longer exist.

7.5.2 Thermal response and diffractive radiation

When diffractive radiation is also taken into account along with thermal effects, three-peak and four-peak gap nematicons can be found in the first band gap as shown in Figures (7.6) and (7.7). Figure (7.6) represents the evolution of the dynamic solutions R and S of Equations (7.34) - (7.36) in a periodic potential strength V_0=1.7 and thermal response coefficients $\tau_0 = \tau_1 = 0.8$, for different diffractive radiation shelf heights. In all three rows of Figure (7.6), the initial beam amplitudes are a_{x0}=5.6, a_{y0}=4.8, and the propagation constant is $\mu = 3.6$. The first, second, and third rows of Figure (7.6) show the evolution of three-peak gap nematicons for $g_x = g_y = 0.5$, $g_x = g_y = 1.5$ and $g_x = g_y = 3.8$, respectively, showing energy redistribution among peaks as diffractive radiation varies.

Figure (7.7) depicts the evolution of R and S in the same periodic potential with thermal response coefficients $\tau_0 = \tau_1 = 1.6$, across increasing diffractive radiation shelf heights. In all three rows of Figure (7.7), the initial beam amplitudes are a_{x0}=9.8, a_{y0}=9.1, and the propagation constant is $\mu = 6.4$. The first, second, and third rows of Figure (7.7) show the four-peak gap nematicons for $g_x = g_y = 2.0$, $g_x = g_y = 5.0$ and $g_x = g_y = 8.6$, respectively, with energy redistribution adjusting dynamically among peaks at different diffractive radiation shelf heights.

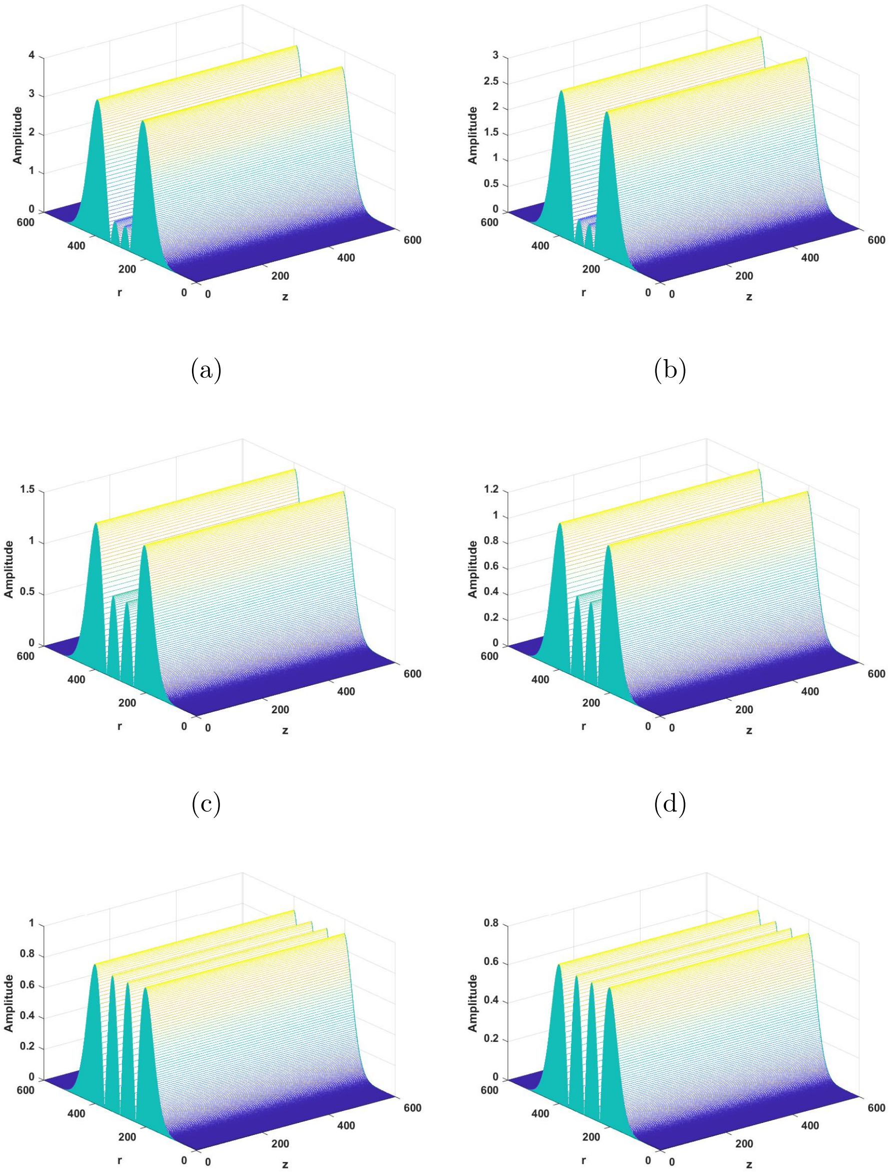

(a) (b)

(c) (d)

(e) (f)

Figure 7.7: Evolution of a four-peak gap nematicon for an initial excitation with a_{x0}=9.8, a_{y0}=9.1, w_{x0}=12, w_{y0}=12, σ_{x0}=0, and σ_{y0}=0, in a periodic potential with strength $V_0 = 1.7$. First column [(a), (c), (e)]: Evolution of R. Second column [(b), (d), (f)]: Evolution of S. First row: g_x=g_y=2. Second row: g_x=g_y=5. Third row: g_x=g_y=8.6. In all three rows, $\tau_0 = \tau_1 = 1.6$ and $\mu = 6.4$.

Experimental validation for our study is supported by previous works that demonstrate the realization of periodic potentials in liquid crystal systems. Specifically, prior research has shown that periodic electrode structures and controlled electric fields can effectively induce spatially varying refractive index profiles in LC waveguides. For instance, in [11], electrically switchable LC waveguide structures were developed for spatial-polarization control of light. These structures utilized spatially modulated electric fields applied to planar-aligned LC cells, with patterned electrodes on conducting glass substrates enabling precise control. The experimental findings confirmed the feasibility of electrically controlled periodic potentials for tuning optical waveguiding properties. Similarly, [12] explores electro-optical cells based on cholesteric liquid crystals, where periodic structures emerge and transform under applied electric fields. Polarizing optical microscopy was used to investigate the formation and behavior of alternating over- and under-twisted defect lines. The periodicity of these structures was voltage-dependent, demonstrating a practical approach for achieving tunable periodic potentials in LC materials. Additionally, [13] presents various techniques for fabricating optical waveguides with LC cores, where molecules form periodic patterns with well-defined periods. Methods such as microstructured electrodes and photoalignment techniques enabled experimental realization of controlled molecular orientations, with waveguiding properties examined through optical fiber grating effects. These studies collectively validate our approach, demonstrating that periodic potentials in LC systems can be achieved through electrically controlled patterned electrodes or structured anchoring methods.

7.6 Linear stability analysis

Bogoliubov-de Gennes (BDG) equations are the most popular method in the analysis of linear stability. Here, the stationary states of the system are perturbed slightly in the form

$$X = R + a(r,z)e^{-i\mu z}, \qquad Y = S + b(r,z)e^{-i\mu z}, \tag{7.37}$$

where the perturbations are given by

$$a(r,z) = a_1(r)e^{i\lambda z} + a_2(r)e^{-i\lambda^* z}, \tag{7.38}$$

$$b(r,z) = b_1(r)e^{i\lambda z} + b_2(r)e^{-i\lambda^* z}. \tag{7.39}$$

The pair of coupled Equations (7.34) and (7.35) are linearized, assuming a_1, a_2, b_1, and b_2 are very small. The resultant equations are given in matrix form:

$$\lambda \begin{pmatrix} a_1 \\ a_2^* \\ b_1 \\ b_2^* \end{pmatrix} = C \begin{pmatrix} a_1 \\ a_2^* \\ b_1 \\ b_2^* \end{pmatrix}, \tag{7.40}$$

where,

$$C = \begin{pmatrix} L_1 + V(r) & 0 & \frac{1}{4}e^{\frac{iz}{1+\gamma(\tau)}} sin2\xi & \frac{R^2}{2} \\ \frac{R^2}{2} & -L_1 - V(r) & 0 & -\frac{1}{4}e^{\frac{-iz}{1+\gamma(\tau)}} sin2\xi \\ \frac{1}{4\gamma(\tau)}e^{\frac{-iz}{1+\gamma(\tau)}} sin2\xi & \frac{S^2}{2} & L_2 + V(r) & 0 \\ 0 & -\frac{1}{4\gamma(\tau)}e^{\frac{iz}{1+\gamma(\tau)}} sin2\xi & \frac{S^2}{2} & -L_2 - V(r) \end{pmatrix}, \tag{7.41}$$

$$L_1 = \frac{1}{2}\left(\frac{d^2}{dr^2} + \frac{1}{r}\frac{d}{dr} + sin^2\xi + |R|^2 + 2\mu\right), \tag{7.42}$$

$$L_2 = \frac{1}{2\gamma(\tau)}\left(\frac{d^2}{dr^2} + \frac{1}{r}\frac{d}{dr} - sin^2\xi + |S|^2 + 2\gamma(\tau)\mu\right). \tag{7.43}$$

Chebyshev polynomial-based spectral methods are used to solve the matrix equation. Perturbation eigenvalues are analyzed with respect to the propagation constant, where imaginary parts indicate linear instability and real parts signify stability.

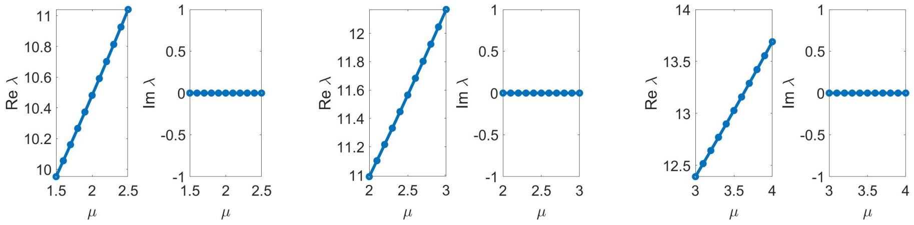

(a) (b) (c)

Figure 7.8: The results of linear stability analysis of the system in a periodic potential with the strength of $V_0 = 1.7$. Stability analysis of two-peak gap nematicons for (a) $\tau_0 = \tau_1 = 0$; (b) $\tau_0 = \tau_1 = 0.8$; (c) $\tau_0 = \tau_1 = 1.6$. The real and imaginary parts of the perturbation eigenvalues (λ) versus the propagation constant μ are displayed.

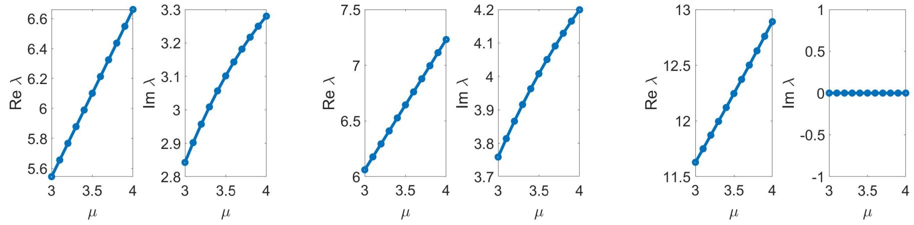

(a) (b) (c)

Figure 7.9: The results of linear stability analysis of the system in a periodic potential with the strength of $V_0 = 1.7$. Stability analysis of three-peak gap nematicons for $\tau_0 = \tau_1 = 0.8$: (a) g_x=g_y=0.5; (b) g_x=g_y=1.5; (c) g_x=g_y=3.8. The real and imaginary parts of the perturbation eigenvalues (λ) versus the propagation constant μ are displayed.

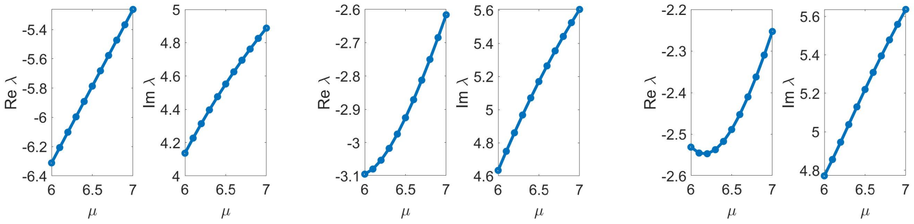

(a) (b) (c)

Figure 7.10: The results of linear stability analysis of the system in a periodic potential with the strength of $V_0 = 1.7$. Stability analysis of four-peak gap nematicons for $\tau_0 = \tau_1 = 1.6$: (a) g_x=g_y=2; (b) g_x=g_y=5; (c) g_x=g_y=8.6. The real and imaginary parts of the perturbation eigenvalues (λ) versus the propagation constant μ are displayed.

Figure (7.8) consists of stability plots for two-peak gap nematicons in a periodic potential strength of $V_0 = 1.7$ for different thermal response coefficients. Figure 7.8(a)-(c) depicts the stability analysis of two-peak gap nematicon for $\tau_0 = \tau_1 = 0$, $\tau_0 = \tau_1 = 0.8$, and $\tau_0 = \tau_1 = 1.6$ respectively. Figure 8(a)-(c) shows that solutions are stable with purely real eigenvalues. This implies that the two-peak gap nematicons with thermal response are stable.

Figure (7.9) presents stability plots for three-peak gap nematicon within a periodic potential of strength $V_0 = 1.7$, for different diffractive radiation shelf heights. Here, both τ_0 and τ_1 are set to 0.8. Figures 7.9(a)-(c) depict the stability analysis of three-peak gap nematicon for g_x=g_y=0.5, g_x=g_y=1.5, and g_x=g_y=3.8 respectively. In Figures 7.9(a) and (b), the presence of non-zero imaginary eigenvalues indicates linear instability in the solutions. Figure 7.9(c) shows that solutions are stable with purely real eigenvalues. This implies that the three-peak gap nematicon with thermal response is stable for diffractive radiation shelf heights g_x=g_y=3.8, with energy nearly evenly distributed across the peaks.

Figure (7.10) shows the stability plots for four-peak gap nematicon in a periodic potential strength of $V_0 = 1.7$ for different diffractive radiation shelf heights. Here, both τ_0 and τ_1 are set to 1.6. Figures 7.10(a)-(c) depict the stability analysis of four-peak gap nematicon for g_x=g_y=2, g_x=g_y=5, and g_x=g_y=8.6 respectively. In Figures 7.10(a)-(c), the presence of imaginary eigenvalues indicates instability in the solutions. This implies that the four-peak gap nematicon with thermal response is unstable. At high thermal response (τ_0=τ_1=1.6), even evenly distributed peaks in four-peak gap nematicon become unstable due to intensified thermal gradients, which create stronger refractive index modulations that disrupt peak confinement. This intensified modulation causes peaks to shift out of phase, leading to instability regardless of peak symmetry.

7.7 Conclusion

This chapter explores the effects of thermal response and diffractive radiation on multi-peak gap nematicons by employing numerical simulations. The analysis covers both stationary and dynamic solutions. It reveals that thermal response alone generates two-peak gap nematicons in the first band gap. As the thermal response coefficient increases, the separation between peaks grows in a nonlinear, parabolic manner, driven by the interaction between thermal effects and refractive index modulation in the nematic liquid crystal medium. Incorporating diffractive radiation allows the formation of three-peak and four-peak gap nematicons, with dynamic energy redistribution among the peaks depending on the diffractive radiation shelf height. Stability analysis of these multi-peak structures is conducted by studying small perturbations using the Bogoliubov–de Gennes equations.

This research has numerous potential applications in advanced photonic technologies, including optical switching, beam shaping, and temperature sensing. The thermal tunability of two-peak gap nematicons is particularly valuable for photonic devices. In optical switching, the ability to adjust the separation between peaks enables transitions between distinct light states, making these structures well-suited for high-speed data processing. In optical fibers or waveguides, thermal effects allow dynamic control of light beams, enhancing signal clarity by managing interference. Additionally, their sensitivity to temperature makes nematicons ideal for thermal sensing, with peak separation providing accurate real-time temperature monitoring. Incorporating diffractive radiation enables energy redistribution, making gap nematicons useful for applications such as optical modulation and laser beam shaping, which are critical in fields like materials processing and medical treatments. By controlling the thermal response and diffractive radiation shelf heights, these systems offer versatile solutions for designing advanced photonic devices.

A promising avenue for future research involves investigating the breather-like excitations within this system. Beyond gap nematicons, nonlinear

Schrodinger-type equations are known to support oscillatory solutions, including breathers. The combined effects of nonlinearity, periodic potential, and diffractive radiation in nematic liquid crystals may create favorable conditions for such excitations. Exploring whether gap nematicons display internal oscillations or periodic energy transfer could offer a deeper understanding of the nonlinear behavior, warranting further investigation.

Bibliography

[1] Lin Y, Jisha CP, Jeng CJ, Lee RK, Malomed BA. Gap solitons in optical lattices embedded into nonlocal media. Physical Review A. 2010 jun;81(6):063803.

[2] Meng H, Zhou Y, Li X, Ren X, Wan X, Zhou Z, et al. Gap solitons in Bose–Einstein condensate loaded in a honeycomb optical lattice: Nonlinear dynamical stability, tunneling, and self-trapping. Physica A: Statistical Mechanics and its Applications. 2021 Sep;577:126087.

[3] Kartashov YV, Vysloukh VA, Torner L. Surface Gap Solitons. Physical Review Letters. 2006 feb;96(7):073901.

[4] Assanto G, Khan C, Piccardi A, Smyth NF. Temperature control of nematicon trajectories. Physical Review E. 2019 dec;100(6):062702.

[5] Sajitha NM, Suneera TP. Thermal response of nematicons in a parabolic potential. Physica Scripta. 2024 May;99(6):065567.

[6] Assanto G, Khan C, Smyth NF. Multihump thermo-reorientational solitary waves in nematic liquid crystals: Modulation theory solutions. Physical Review A. 2021 jul;104(1):013526.

[7] Assanto G, Smyth NF. Spin-optical solitons in liquid crystals. Physical Review A. 2020 sep;102(3):033501.

[8] Laudyn UA, Piccardi A, Kwasny M, Karpierz MA, Assanto G. Thermo-optic

soliton routing in nematic liquid crystals. Optics Letters. 2018 may;43(10):2296.

[9] Aleksić NB, Petrović MS, Strinić AI, Belić MR. Solitons in highly nonlocal nematic liquid crystals: Variational approach. Physical Review A. 2012 mar;85(3):033826.

[10] Sajitha NM, Suneera TP. The effect of parabolic potential on the generation of higher harmonics of nematicons. Physica Scripta. 2023 Apr;98(5):055502.

[11] Kabanava VS, Rushnova II, Melnikova EA, Tolstik AL. Nematic Liquid Crystal Waveguides for Spatial Control of Linearly Polarized Light Waves. In: 2019 PhotonIcs amp; Electromagnetics Research Symposium - Spring (PIERS-Spring). IEEE; 2019. p. 3832-5.

[12] Prishchepa O, Krakhalev M, Rudyak V, Sutormin V, Zyryanov V. Electrically turning periodic structures in cholesteric layer with conical–planar boundary conditions. Scientific Reports. 2021 Apr;11(1).

[13] Ertman S, Orzechowski K, Rutkowska K, Kołodyńska O, Różycka J, Ignaciuk A, et al. Periodic liquid crystalline waveguiding microstructures. Scientific Reports. 2023 Aug;13(1).

Chapter 8

Results and Recommendations

This chapter presents a summary of the key findings of the thesis and offers suggestions for future research inspired by the results. The study of optical beam propagation in uniaxial nematic liquid crystal in the nonlocal regime is the basis of the research carried out in this thesis. Nonlinear waves and liquid crystals are both thriving topics with numerous scientific and technological applications. The thesis, "Studies on Nonlinear Beam Dynamics in Uniaxial Nematic Liquid Crystals Under the Influence of Temperature, Diffractive Radiation, and Potentials" is highly relevant to advancing the understanding of nonlinear beam dynamics in nematic liquid crystals, a material with significant potential for reconfigurable optical applications. It provides insights into the interplay of the potentials, thermal effects, and diffractive radiation, enabling the design of robust waveguides, optical switches, and beam-steering technologies. Section 8.1 outlines the key results, while section 8.2 provides the recommendations for future research.

8.1 Results

- The interplay between diffractive radiation shed and the damping coefficient in a nematic liquid crystal with nonlocal nonlinearity has been studied. The system is analyzed using semi-analytical and numerical methods. When the damping profile is a constant or a periodic function of the propagation distance, nematicon propagation is only possible for high diffractive radiation shelf height. However, a very small value of diffractive radiation shelf height can counterbalance the effect of hyperbolic damping of the beam, resulting in nematicon propagation through the medium.

- The studies have been extended to the thermal response of single-peak and double-peak solitons in a nematic liquid crystal. Single-peak nematicons have been found for low values of thermal response coefficients. This regime is characterized by focusing reorientational nonlinearity. For fairly large values of thermal response coefficients, the defocusing thermal nonlinearity is greater than the focusing reorientational nonlinearity. As a result, the beam broadens, flattens, and eventually separates into double-peak nematicons. Linear stability analysis reveals that single-peak nematicons are stable regardless of thermal response coefficient values, whereas double-peak nematicons are stable only for large values of thermal response coefficients.

- The behavior of nonlocal spatial optical solitons in a uniaxial nematic liquid crystal subjected to a parabolic potential has been further explored. The governing equations of the system were solved using both semi-analytic and numerical approaches. Our results show that nematicons can form within the parabolic potential, where they exhibit periodic oscillations. It was observed that the wavelength of these oscillations decreases linearly as the strength of the potential increases. By adjusting the potential strength, it is possible to generate higher harmonics of the nematicons. Additionally, linear stability analysis indicates that nematicons remain stable within the parabolic potential.

- The study then focuses on the thermal response of nematicons in a parabolic potential. In the absence of thermal response, single-peak nematicons exist due to the dominance of focusing reorientational nonlinearity. However, when thermal response is introduced, the interaction between the focusing reorientational and defocusing thermal nonlinearities leads to the transformation of single-peak nematicons into double-peak ones. In this scenario, the beam profile splits into two peaks as the defocusing thermal nonlinearity outweighs the focusing reorientational nonlinearity. This competition between the nonlinearities alters the energy landscape experienced by the light beam within the medium. The combined effect of focusing reorientational and defocusing thermal nonlinearities creates multiple maxima in the energy landscape, stabilizing double-peak nematicons as equilibrium states. When parabolic potential is present, periodic oscillations emerge in the nematicon. For small thermal response coefficients, double-peak nematicons with periodic oscillations are observed. The thermal response coefficients significantly influence the wavelength of these oscillations, with the wavelength increasing as the thermal response coefficients rise. For larger thermal response coefficients, the double-peak nematicon becomes non-oscillatory. Linear stability analysis shows that single-peak nematicons and double-peak nematicons with periodic oscillations are stable, whereas double-peak nematicons without oscillations are unstable.

- The study has further investigated the formation and stability of single-peak and multi-peak gap nematicons using numerical methods. Single-peak and multi-peak gap nematicons can be found in the first band gap. Single-peak gap nematicons can be formed for a broad range of propagation constants. Multi-peak gap nematicons, however, can only exist above a certain minimum propagation constant. The intensity distribution among the peaks in a multi-peak gap nematicon is highly sensitive to the intensity of the input beam. To analyze stability, we utilized the Bogoliubov-De-Gennes equations to assess the response of the stationary solution to small perturbations. Our findings show that single-peak gap nematicons are stable. Multi-peak gap nematicons with equal peak amplitudes are stable, while those with unequal peak amplitudes are unstable.

- The impact of thermal response and diffractive radiation on multi-peak gap nematicons is then studied using numerical simulations. Both stationary and dynamic solutions are explored, revealing that thermal response alone induces the formation of two-peak gap nematicons in the first band gap. As the thermal response coefficients increase, the separation between the peaks grows in a nonlinear, parabolic manner. This peak separation results from the interaction of thermal effects and changes in the refractive index of the nematic liquid crystal medium. Upon incorporating diffractive radiation, three-peak and four-peak gap nematicons can also observed, with energy redistribution occurring dynamically among the peaks as the shelf height of the diffractive radiation varies. Linear stability analysis indicates that two-peak gap nematicons with thermal response are stable. The three-peak gap nematicons remain stable for comparatively large diffractive radiation shelf heights with energy almost evenly distributed across the peaks. However, at high thermal response even evenly distributed peaks in a four-peak gap nematicon become unstable. This instability arises due to intensified thermal gradients, which enhance refractive index modulations and disrupt peak confinement. These stronger modulations cause the peaks to shift out of phase, leading to instability, regardless of the symmetry of the peaks.

This research has broad potential applications in advanced photonic systems, particularly in optical switching, beam shaping, and temperature sensing. The thermal tunability of two-peak gap nematicons holds promise for photonic devices, as it enables control over the peak separation, facilitating transitions between different light states for high-speed data processing. In optical fibers or waveguides, thermal effects offer dynamic manipulation of light beams, enhancing signal clarity by adjusting interference effects. Additionally, the temperature sensitivity of nematicons makes them ideal for precise real-time thermal monitoring in temperature sensing applications. When combined with diffractive radiation, nematicons enable energy redistribution, which can be applied to optical modulation and laser beam shaping, particularly in fields like material processing and medical treatments. By controlling the thermal response and diffractive radiation shelf heights, a versatile functionality is achieved for the design of advanced photonic systems.

8.2 Recommendations

The study of nematicon propagation under various conditions, including diffractive radiation, damping effects, parabolic and periodic potentials, and thermal responses, is explored in this thesis. It provides significant insights into nonlinear light-matter interactions in nematic liquid crystals. However, there are several avenues for further exploration that can deepen our understanding of these phenomena and broaden their potential applications. Future research in diffractive radiation could focus on exploring its effects on nematicons in various complex media, including anisotropic and gradient-index materials. Investigating the interaction between diffractive radiation and different beam profiles, such as Laguerre and Hermite-Gaussian beams, could lead to enhanced control over beam propagation and manipulation. Additionally, the role of diffractive radiation in multi-peak and multi-dimensional soliton formation could be studied to enable more versatile applications in optical communication and beam steering. Future studies might also delve into optimizing diffractive radiation in systems with higher-order nonlinearities, enabling more efficient energy transfer and dynamic control for advanced photonic technologies. There are several potential future research directions that involve the investigation of two or more interacting beams traveling through NLC. Investigating the interaction of nematicons with other types of solitons or multiple nematicon beams could unveil new forms of soliton behavior. Studying such multicomponent systems might enable the development of novel optical devices that utilize the interaction between different types of light beams for more advanced functionalities. The effect of parabolic potentials on the generation of higher harmonics of nematicons has opened up possibilities for extending this work to other types of nonlinear interactions. Investigating different potentials such as anharmonic, periodic, or even stochastic potentials could lead to the discovery of novel harmonic generation processes. Moreover, extending the research to higher-dimensional potentials could provide new ways to manipulate nematicon behavior for advanced photonic applications. A potential continuation of this work would be to investigate responses of nematicons with other optical beam types, such as elliptical, Hermite polynomial type, Laguree polynomial type, and so on. There are numerous opportunities to broaden the study of nonlocal nonlinear media to encompass diverse forms of nonlinearities, higher-order diffraction terms, etc. Investigating the effects of more intricate potentials beyond the parabolic and periodic forms, such as anharmonic or time-varying potentials, could lead to new insights into the controllability of nematicons. Tailoring the potential could provide a means of finely tuning the propagation characteristics, opening the door to more sophisticated applications in optical communication or material processing.

The theoretical insights gained from this thesis provide a strong foundation for experimental investigations. Future research could focus on experimental validation of the predicted phenomena, especially in novel liquid crystal materials with enhanced nonlinear and thermal properties. Additionally, the integration of nematicons into photonic devices, such as optical switches, modulators, or filters, remains a promising area for further development. By fine tuning the properties of the material and potentials, nematicons could be harnessed for a wide range of applications in optical communications and photonic circuitry. Similar research can be conducted on the optical vortex, dark nematicons, soliplasmons (solitons+surface plasmons), and so on. By addressing these areas in future research, the understanding of nematicon dynamics can be significantly advanced, leading to new theoretical insights and practical applications in photonics and beyond.